Summer 2016

Local optical phase detection probes with an application to a high speed boundary layer

Matias Nicholas Perret
University of Iowa

Recommended Citation

Perret, Matias Nicholas. "Local optical phase detection probes with an application to a high speed boundary layer." PhD (Doctor of Philosophy) thesis, University of Iowa, 2016.
https://doi.org/10.17077/etd.17q4iqdl

LOCAL OPTICAL PHASE DETECTION PROBES WITH AN APPLICATION TO A HIGH SPEED BOUNDARY LAYER

by

Matias Nicholas Perret

A thesis submitted in partial fulfillment
of the requirements for the Doctor of
Philosophy degree in Mechanical Engineering
in the Graduate College of
The University of Iowa

August 2016

Thesis Supervisor: Professor Pablo M. Carrica

Graduate College
The University of Iowa
Iowa City, Iowa

CERTIFICATE OF APPROVAL

PH.D. THESIS

This is to certify that the Ph.D. thesis of

Matias Nicholas Perret

has been approved by the Examining Committee
for the thesis requirement for the Doctor of Philosophy
degree in Mechanical Engineering at the August 2016 graduation.

Thesis Committee: ___________________________________
Pablo M. Carrica, Thesis Supervisor

____
Hongtao Ding

____
William E Eichinger

____
Mark Hyman

____
Anton Kruger

ACKNOWLEDGMENTS

I would like to thank my advisor Pablo for his continuous support, patience, enthusiasm and friendship that it took to see me through to the end of my graduate studies.

I would like to thank the members of my committee, Anton, Bill, Hongtao and Mark who made themselves available to provide their wisdom and expertise, whether it was to a casual knock on their door or providing logistical help during experiments, your guidance has been greatly appreciated.

I would also like to acknowledge all of the students and fellow colleges I've had the opportunity to work with, you have truly made pursing graduate studies a treat.

Mostly I would like to thank Lauren and my family for their support and companionship that they have given me along this path I have taken.

This research was in part funded by the US Office of Naval Research under Grant N000141110026 with Drs. Ki-Han Kim and Patrick Purtell as program managers. The text of Chapter 2 is, in part, a reprint of the material as it appears in the International Journal of Multiphase Flow (Perret & Carrica, 2015).

ABSTRACT

This thesis presents the continued development of micro optical phase detection instrumentation capable of measuring void fraction, interfacial area density, interfacial velocity and bubble sizes and their application to measurements in a high speed boundary layer. The instrumentation consists of micro sized sapphire tipped probes tailored to measure in the two-phase flow of air bubbles in water. Probe tips with geometries intended to maximize field life while minimizing intrusiveness were designed, fabricated and characterized. The characterization revealed that the active *region* of a probe tip can go beyond the highly sensitive 45 degree tip. Controlling the active length of the tips can be achieved through a combination of taper angles and 45 degree tip size, with larger tips having shorter active lengths.

The full scale bubbly flow measurements were performed on a 6 m flat bottom survey boat. The aforementioned quantities were measured on bubbles naturally entrained at the bow of the boat. Probes were positioned at the bow of the boat, near the entrainment region and at the stern where the bubbles exit after having interacted with the high shear turbulent boundary layer. Experiments were conducted in fresh water, at the Coralville Lake, IA, and salt water, at the St. Andrews Bay and Gulf Coast near Panama City, FL. The results indicate that the bubbles interact significantly with the boundary layer. At low speeds, in fresh water, bubble accumulation and coalescence is evident by the presence of large bubbles at the stern. At high speeds, in both fresh and salt water, bubble breakup dominates and very small bubbles are produced near the hull of the boat. It was observed that salt water inhibits coalescence, even at low boat speeds. Void fraction was seen to increase with boat speeds above 10 knots and peaks near the wall. Bubble velocities show slip with the wall at all speeds and exhibit large RMS fluctuations, increasing near the wall.

PUBLIC ABSTRACT

This thesis presents the continued development of micro optical phase detection instrumentation capable of measuring void fraction, interfacial area density, interfacial velocity and bubble sizes and their application to measurements in a high speed boundary layer. The instrumentation consists of micro sized sapphire tipped probes tailored to measure in the two-phase flow of air bubbles in water. Probe tips with geometries intended to maximize field life while minimizing intrusiveness were designed, fabricated and characterized. The characterization revealed that the active *region* of a probe tip can go beyond the highly sensitive 45 degree tip. Controlling the active length of the tips can be achieved through a combination of taper angles and 45 degree tip size, with larger tips having shorter active lengths.

The full scale bubbly flow measurements were performed on a 6 m flat bottom survey boat. The aforementioned quantities were measured on bubbles naturally entrained at the bow of the boat. Probes were positioned at the bow of the boat, near the entrainment region and at the stern where the bubbles exit after having interacted with the high shear turbulent boundary layer. Experiments were conducted in fresh water, at the Coralville Lake, IA, and salt water, at the St. Andrews Bay and Gulf Coast near Panama City, FL. The results indicate that the bubbles interact significantly with the boundary layer. At low speeds, in fresh water, bubble accumulation and coalescence is evident by the presence of large bubbles at the stern. At high speeds, in both fresh and salt water, bubble breakup dominates and very small bubbles are produced near the hull of the boat. It was observed that salt water inhibits coalescence, even at low boat speeds. Void fraction was seen to increase with boat speeds above 10 knots and peaks near the wall. Bubble velocities show slip with the wall at all speeds and exhibit large RMS fluctuations, increasing near the wall.

TABLE OF CONTENTS

LIST OF TABLES

LIST OF FIGURES

CHAPTER 1:INTRODUCTION

This thesis documents the development, testing and application of a tool used to measure bubble concentration, velocity and size. The tool, a sapphire tipped optical phase detection probe, was used to measure the two phase quantities in the full scale boundary layer of a flat bottom boat in fresh and salt water.

1.1 Introduction

Two-phase flows are a particular subset of multi-phase flows in the broad context of fluid mechanics and are defined as fluid composites whose constituents remain separated and whose continuous phase is able to continuously deform (flow). Common examples of two-phase flows include bubbles in water (gas in liquid), rain (liquid in gas), mud (solid in liquid) and ash plumes (solid in gas). Note that these examples are multi-component flows, in which the constituent are of different materials. Single component two-phase flows exist as well, in which the constituents are made of the same material but in different phases, as in the case of steam/water flows often found in large scale power plants or ice/water flows such as ice flow in a thawing river. The previous examples are dispersed two-phase flows, meaning that one of the phases (the dispersed phase) is dispersed within the continuous phase (the carrier phase). These flows are different from separated two-phase flows, where the two phases are continuous throughout their domain, such as an oil slick on a body of water.

The topic of this thesis focuses on the measurement of dispersed, multi-component two-phase flow made up of air bubbles in water and how it pertains to ship hydrodynamics. However, the measurement techniques discussed here can be applied to any fluid/gas flow as long as both phases have the appropriate optical properties.

1.2 Background

The topic of two-phase flows pertaining to ship hydrodynamics has been the subject of numerous computational and experimental investigations. The bubble entrainment mechanisms and the resulting two-phase mixture play a key role in the behavior of the bubbly wake, the acoustic signature and the hydrodynamic performance of a ship. Bubbles are naturally entrained into the water by the ship's breaking bow wave, hull to water contact line and from cavitation along low pressure appendages and propellers. Additionally, bubbles may be intentionally entrained by direct forms of bubble injection or features specifically designed to entrain air. Prairie and Masker systems, which use the bubbles' acoustic dampening characteristics to form a sound barrier from the ship's machinery and propeller noise, have long been used in naval applications to avoid passive sonar detection (Fig. 1). In Naval interests, the bubble entrainment mechanisms and the resulting two-phase mixture play a key role in the behavior of the bubbly wake of a ship and can be beneficial, as mentioned above, or detrimental as the bubbles serve as an easily detectable (both visually and acoustically) method to find and track a ship.

Direct bubble injection has also found uses in commercial and recreational applications.

Figure 1: A DD-963 class destroyer displaying the use of a Prairie system (on left). Note the increased visibility of the wake

Bubble induced drag reductions from 4% to 22% have been achieved in ships and flat plates (Latorre *et al.*, 2003; Takahashi *et al.*, 2003; Ceccio, 2010) and are a viable option for decreasing the consumption of bunker fuels in tanker and container ships. In planing power boats, stepped hulls have long been used to introduce pockets of air under the hull; pockets of air allow the hull to break up the lifting surface, enabling the hull to ride on pockets of air, resulting in higher speeds. The pockets of air also provide a cushioning effect that decrease the intensity of impacts with water (slamming).

Early studies of the National Defense Research Committee (NDRC, 1946) revealed the importance of ship bubbly wakes and led to numerous studies (Trevorrow *et al.*, 1994; Trevorrow *et al.* 2006; Vagle and Burch, 2004; Stanic *et al.*, 2009, Terrill and Fu, 2008) focusing on the characterization of a ship's bubbly wake by acoustic attenuation and backscattering at full and model scale. These studies have concentrated in the far field, away from the hull of the ship, where acoustic methods are not adversely affected by the noise created from the ship and the acoustic characteristics of the hull itself. Limited studies have been performed in the near field of a ship, where the bubble sources are, and none within the boundary layer at full scale.

Johansen *et al.* (2010) performed experimental measurements of the bubbly flow on the full scale research vessel *Athena II*. The authors focused on two-phase quantities aft of the breaking bow wave, the starboard masker and at the stern. Using optical phase detection probes, they found that gas volume fraction increases with speed and with direction relative to the sea state (heading into the waves), and decreases with depth. The bubble size distributions were found to be dominated by bubbles smaller than 500 μm in radius at greater depths, with bubbles approximately $2\,mm$ in radius occurring towards the free surface. Their stern measurements revealed that the ratio of bubbles smaller than 200 μm to bubbles bigger than 200 μm increases over 10 fold at the deepest locations relative to the same horizontal location but higher in the water column. While they are inconclusive to the exact cause, one of their possible explanations is that bubbles entrained at the bow and masker are transported downstream along the hull, where they are subjected to the large shear stresses and turbulence below the hull causing the larger bubbles to breakup. The smaller bubbles then exit from below the hull at the transom (where they are measured). Similar results were found by Terrill *et al.* (2005), also on the Athena II, using an array of 12 conductivity probes and a submersible bubble sizing camera to measure void fraction and bubble size distributions.

As mentioned above, acoustic measurements characterizing the bubbly wake of a ship have shown large numbers of small bubbles existing in the far wake of a ship. While it is clear that the bubbles originate from the ship, the processes that occur to create the small bubbles are not yet fully understood. Under the hull of a ship, a number of processes occur in the turbulent and shearing boundary layer that results in the bubbly wake. Fig. 2 shows a schematic of the experimental platform, herein called Kann boat or simply boat, which was used to study the interaction of naturally entrained bubbles with a full-scale boundary layer in fresh and salt water. This application motivated the development of the probes discussed in this thesis. In Fig. 2, bubbles are naturally entrained at the bow of the boat from bow's breaking wave and along the hull-to-water contact line. The bubbles are transported below the hull and travel the length of the hull before exiting at the stern. While under the hull, buoyancy acts on the bubbles and pushes them up against the hull where the turbulent intensity and velocity gradients are high. Under these circumstances, it is likely for bubble breakup to occur. Similarly, due to the buoyant accumulation of bubbles below the hull and the resulting high void fraction, it is also likely for bubble coalescence to occur. Depending on the conditions on of these two mechanisms will dominate over the other. In the case of low boat speeds, where turbulent intensities and shear rates are low, coalescence is expected to dominate over breakup. Conversely, at higher boat speeds, where turbulent intensities and shear rates are high, bubble breakup is expected to dominate. The competition between breakup and coalescence highlights the importance of these processes and their influence on the resulting bubbly wake.

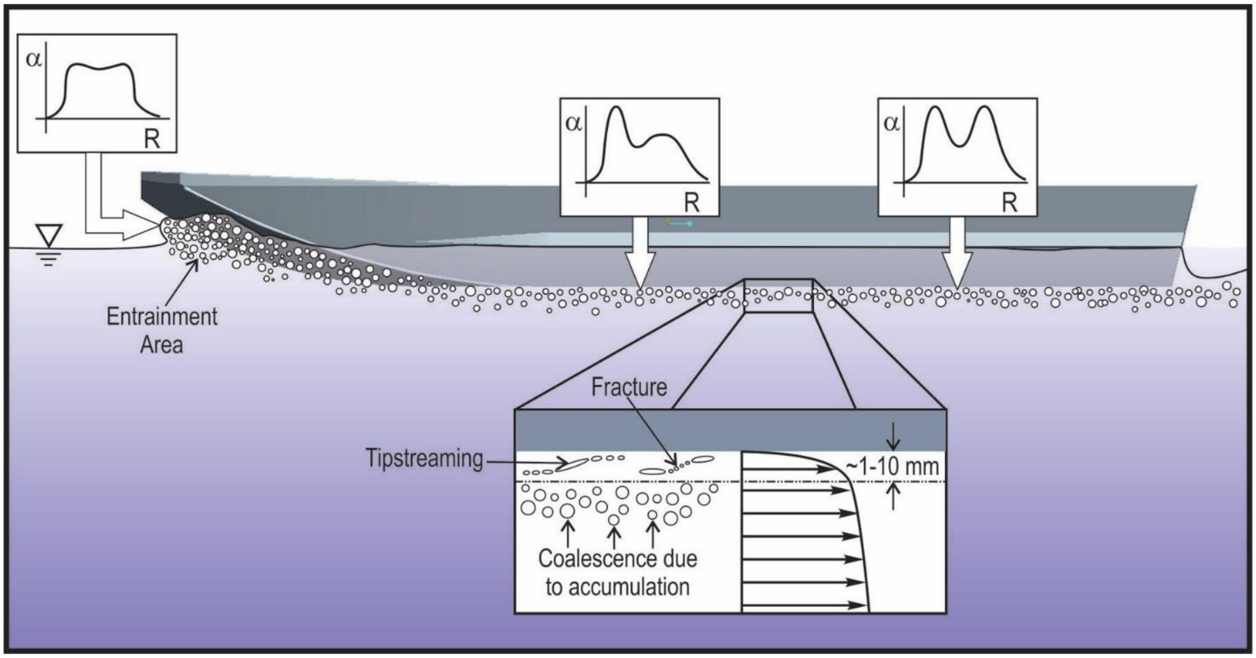

Figure 2: Diagram of bubble entrainment and transport processes in the Kann boat

1.3 Theoretical and modeling background

The bubbly flow around a ship can be described statistically with the bubble size distribution function $f(\boldsymbol{r}, m, t)$, such that $f(m, \boldsymbol{r}, t)dm$ is the expected number of bubbles per unit volume at location $\boldsymbol{r}$ and time t with mass within dm of m. Since pressure changes are significant due to hydrostatics and flow dynamics in ship flows, the bubble mass, which doesn't change with pressure, is usually adopted as the internal variable (Castro and Carrica, 2013). Bubble deformation leads to ambiguities since bubbles with different shapes can have the same mass. Though a shape parameter can be added as an internal variable to better generalize the bubble size distribution function, spherical shape is assumed in this work when analyzing and discussing all data. This assumption considerably simplifies the interpretation of the results, and general conclusions will still be valid despite bubbles deforming considerably inside the boundary layer. For spherical bubbles, mass and radius are related by $r = (3\nu(m,p)/4\pi)^{1/3}$, with $\nu(m,p)$ the volume of a bubble of mass m for a local pressure p.

From the bubble size distribution the number density and void fraction are computed as:

$$N(\boldsymbol{r},\boldsymbol{t}) = \int_0^\infty dm f(m,\boldsymbol{r},t) \qquad (1)$$

$$\alpha(\boldsymbol{r},t) = \int_0^\infty dm \frac{m}{\rho(m,\boldsymbol{r},t)} f(m,\boldsymbol{r},t) \qquad (2)$$

where $\rho(m,\boldsymbol{r},t)$ is the local internal density of a bubble of mass m, affected by the surface tension.

The bubble size distribution changes as bubbles change size due to coalescence, breakup and dissolution. Dropping all internal variables, the equation governing these changes in the context of bubbly flows can be written as (Guido-Lavalle *et al*., 1994)

$$\frac{\partial f}{\partial t} + \nabla \cdot (\boldsymbol{u} f) + \frac{\partial}{\partial m}(\dot{m} f) \doteq \beta + \chi \qquad (3)$$

where $\boldsymbol{u}$ is the bubble velocity corresponding to bubbles of mass m and β and χ are the breakup and coalescence sources for bubbles of mass m. The third term in the right hand side is the bubble dissolution, which in the case of the experiments presented herein can be neglected due to the short time elapsed between bubble entrainment and measurement. In a full-scale ship, were bubbles reside within the boundary layer for long times, this term may be important.

1.3.1 Bubble-boundary layer interactions

Several mechanisms exist for the breakup of bubbles and have been studied extensively in literature. The conditions which lead to bubble breakup are such that the external forces acting on a bubble to break it exceed the surface tension and viscous stresses within the bubble that act to keep it together (Liao and Lucas, 2009). In this context, bubble breakup is described by the type of external forces acting on the bubble, the most common types are: turbulence induced breakup, shear induced breakup and tip streaming (a shearing off process). All of these forces are expected in the boundary layer of a ship, though not necessarily with the strength to break up a bubble.

Breakup is incorporated into Eq. 3 adding a positive source due to breakup of larger bubbles creating bubbles with mass m and a negative source due to bubbles of mass m that breakup and are transferred to smaller bubble sizes (Castro and Carrica, 2013)

$$\beta(m,\boldsymbol{r},t) = \int_{m}^{\infty} h(m,m')(b(m')f(m',\boldsymbol{r},t)dm' - b(m)f(m,\boldsymbol{r},t) \qquad (4)$$

In Eq. 4 h is the size distribution of the bubbles created at breakup and b is the breakup frequency. These two parameters are critical to understand size distributions that contain large numbers of small bubbles. To help in the interpretation of models and experiments, bubble radii and diameters instead of masses will be used whenever possible in subsequent discussions.

1.3.1.1 Turbulent breakup

Turbulence induced breakup is the most studied mechanism in literature (Prince and Blanch 1990; Luo and Svendsen 1996; Martínez-Bazán *et al.* 1999, Lehr *et al.* 2002). In this mechanism, the bubble will deform due to fluctuations of the surrounding fluid and collisions with turbulent eddies. If the force acting on the bubble is strong enough, the bubbles' surface will become unstable and result in the bubble breaking up into two or more smaller bubbles typically of uneven sizes. With respect to the magnitude of restoring forces on a bubble, larger bubbles are easier to break than smaller ones, and smaller bubbles are more stable in a turbulent environment. Luo and Svendsen (1996) and Lehr *et al.* (2002) proposed turbulent breakup models that predict both h and b, based on balances of stabilizing forces (surface tension and inertia) and destabilizing forces (turbulence). Hinze (1955) suggested that the maximum stable size for a bubble in a turbulent flow is given by:

$$d_{max} = 0.725 \frac{\sigma^{3/5}}{\varepsilon^{2/5} \rho_i^{3/5}} \tag{5}$$

In Castro and Carrica (2013, Fig. 1) the models of Luo and Svendsen (1996) and Lehr *et al*. (2002) were compared against the predictions of Eq. 5. In these models, as well as in Eq. 5, the turbulent dissipation rate is used as the measure of breakage driving force. An analysis of both models shows that Lehr *et al*. (2002) model matches the well accepted Hinze (1955) correlation (Eq. 5) for the maximum stable size and properly accounts for the energy needed to breakup bubbles, preventing bubbles too small from being unphysically produced. On the other hand, the model of Luo and Svendsen (1996) maximizes the daughter bubble size distribution for extremely small bubbles.

In Athena R/V, measurements by Terrill *et al*. (2005) and Johansen *et al*. (2010) show large numbers of bubbles well below $100\ \mu m$ in diameter coming from below the hull at the stern. For the Kann boat used in this work, advancing at 18 knots, the dissipation rate obtained from numerical simulations is shown in Fig. 3. Most interesting is the fact that $\varepsilon = 1800\ m^2/s^3$ for distances to the wall below $200\ \mu m$ both at the stern and $2.4\ m$ upstream of the stern. In this small region the dissipation rates are very large and bubbles as small as $100\ \mu m$ in diameter can still break, according to Eq. 5. $1\ mm$ away from the wall the dissipation rate at the stern is estimated at $\varepsilon = 130\ m^2/s^3$ (Fig. 2), limiting breakup to bubbles larger than $340\ \mu m$ in diameter. Farther out from the wall the dissipation drops rapidly to approximately $\varepsilon = 10\ m^2/s^3$, making bubble breakup less likely.

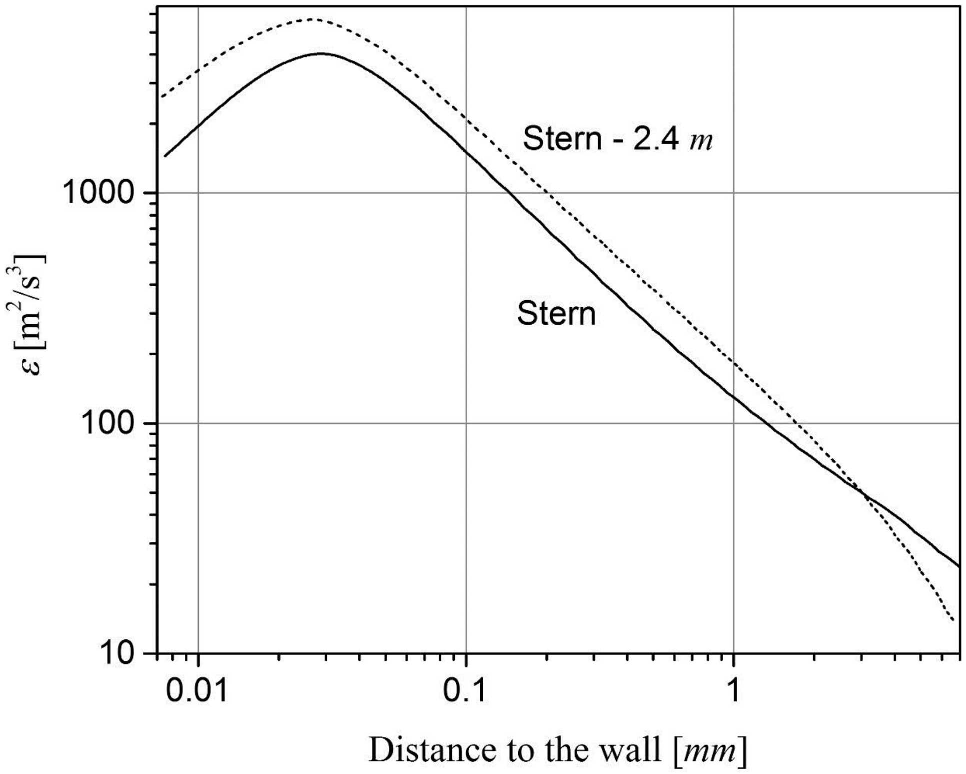

Figure 3: Turbulent dissipation rate at the stern and 2.4 m upstream of the stern as predicted by CFD for a boat speed of 18 knots

The terms in the breakup kernel in Eq. 4 are shown in Figs. 4 and 5, which show the breakup rate and the daughter size distributions for dissipation rates $\varepsilon = 10,\ 130$ and $1500\ m^2/s^3$ and for mother bubble sizes $d' = 0.4$, 1.5 and $6\ mm$ using Lehr *et al*. (2002) model. The breakup rate increases quickly with the dissipation rate, and the cutoff diameter (where the breakup rate drops below $1/s$) are consistent with Eq. 5. Beyond the cutoff diameter the breakup rate increases rapidly, which indicates that small bubbles could be produced in large quantities if larger bubbles breakup into very small daughters.

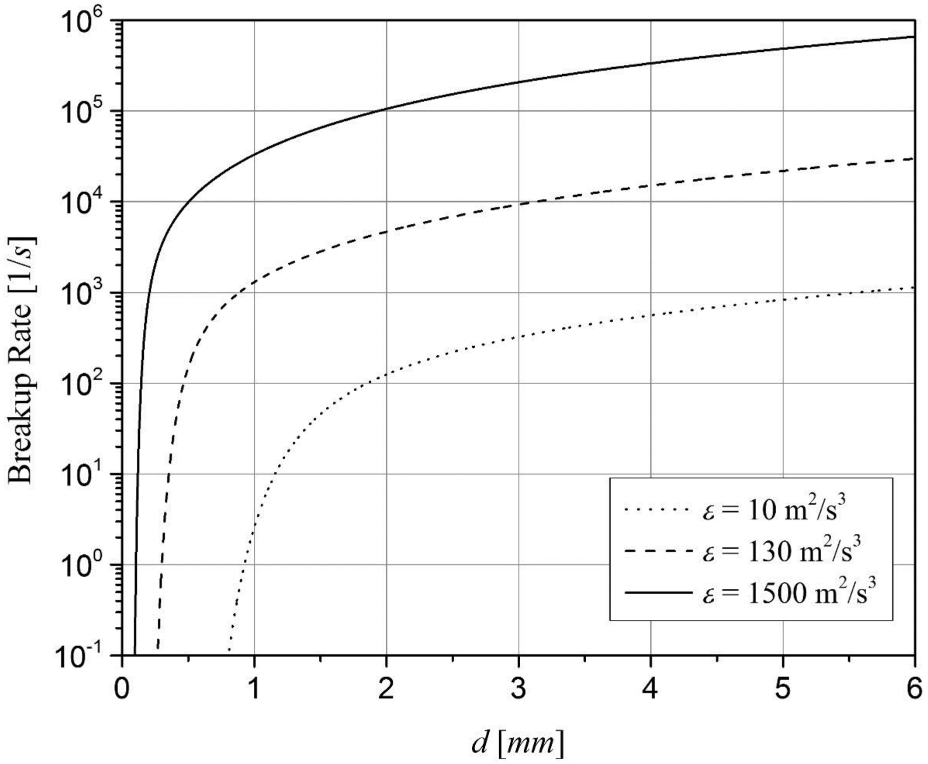

Figure 4: Breakup rate predicted by Lehr *et al.* (2002) model for different dissipation rates as a function of bubble size

The predicted normalized daughter size distributions in Fig. 5 show that for smaller bubbles, equal-sized daughters are favored, but as turbulence increases the resulting daughters are smaller. For a $d = 0.4\,mm$ bubble, the daughter distribution peaks at $d/d' = 0.794$ (two bubbles of the same volume) for $\varepsilon = 10\,m^2/s^3$, while for $\varepsilon = 1500 m^2/s^3$ the peak occurs at $d/d' = 0.34$, with bubbles as small as $d = 40\,\mu m$ possible and a 3% probability of breakup events creating bubbles smaller than $d = 60\,\mu m$.

Larger bubbles tend to break into a small and a large bubble. A $6\,mm$ bubble has a daughter distribution that peaks at $d/d' = 0.17$ for $\varepsilon = 10\,m^2/s^3$ and at $d/d' = 0.022$ for $\varepsilon = 1500 m^2/s^3$. This peak in the distribution for $\varepsilon = 1500 m^2/s^3$ corresponds to a most probable daughter diameter $d = 132\,\mu m$, but, as was the case for $d = 0.4\,mm$ bubbles, there is a 3% probability that the daughter bubbles will be smaller than $d = 60\,\mu m$.

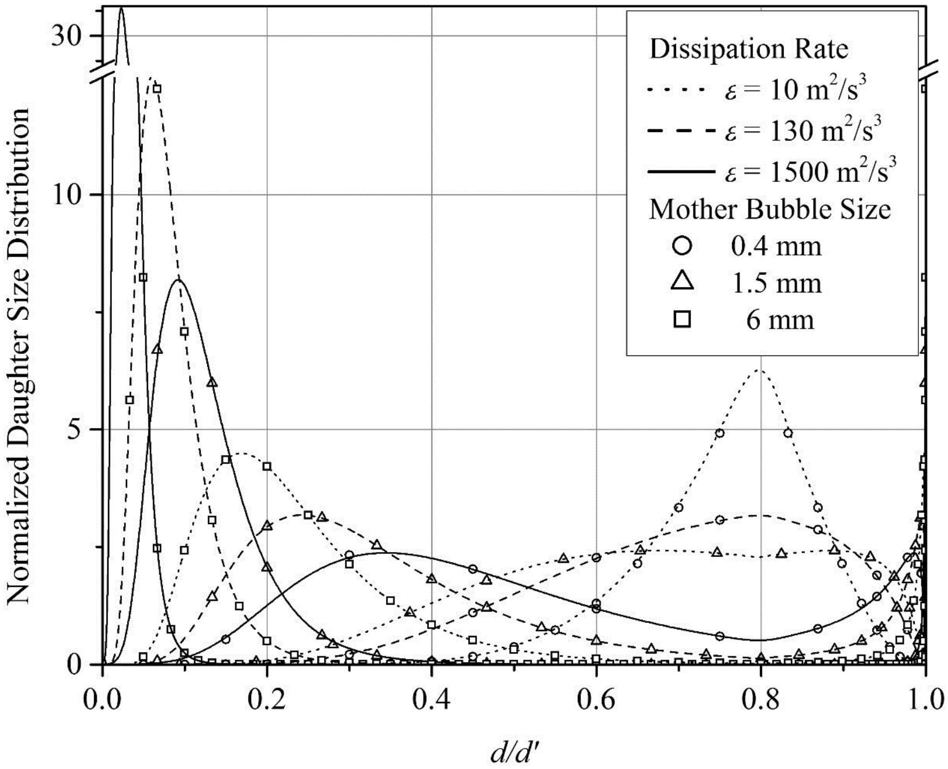

Figure 5: Daughter size distribution predicted by Lehr *et al.* (2002) for different dissipation rates and mother bubble sizes

The discussion above shows that breakup processes inside a ship boundary layer can create bubbles of sizes in the order $d = 50\ \mu m$ by multiple breakup events from bubbles sized $d = 120\ \mu m$ or larger. However, it would be difficult to explain the experimental peak in bubble size distribution at less than $d = 100\ \mu m$ (Terrill *et al.*, 2005) with turbulent breakup alone, since bubbles smaller than $d = 150\ \mu m$ have a small breakup frequency even very close to the wall, see Fig. 4. Since each breakup event produces only one small bubble and this is too small to breakup further, the peak in the bubble size distribution should not occur for bubbles smaller than $d = 150\ \mu m$ if turbulent breakup was the only process breaking bubbles up.

1.3.1.2 Shear breakup

Shear induced breakup involves the deformation of a bubble due to the velocity gradient imposed on it (Fig. 6). Similar to turbulent breakup, if the deformation is greater than the forces keeping the bubble together, the bubble will fracture typically into two equal sized bubbles. Studies by Grace (1982), De Bruijn (1991, 1993), Elemans *et al.* (1993), Janssen *et al.* (1994) and Muller-Fischer *et al.* (2008) have focused on experiments with drops where high capillary numbers can be achieved. Experiments show that at high capillary numbers bubbles elongate significantly and break into several smaller ones. In all these studies two dimensionless parameters are defined: the viscosity ratio $\lambda = \mu_g/\mu_l$ and the capillary number,

$$Ca = \frac{\mu_l \dot{\gamma} R}{\sigma} \qquad (6)$$

where $\dot{\gamma}$ is the shear rate and relates shear to capillary forces.

Experiments show that if the critical capillary number exceeds a critical value Ca_{crit}, breakup occurs. This critical capillary number is a function of the viscosity ratio only (Grace, 1982). For the air water system at $20° C$, the viscosity ratio is $\lambda = 0.0183$ and the corresponding critical capillary number is $Ca_{crit} \approx 1.3$ (Grace, 1982).

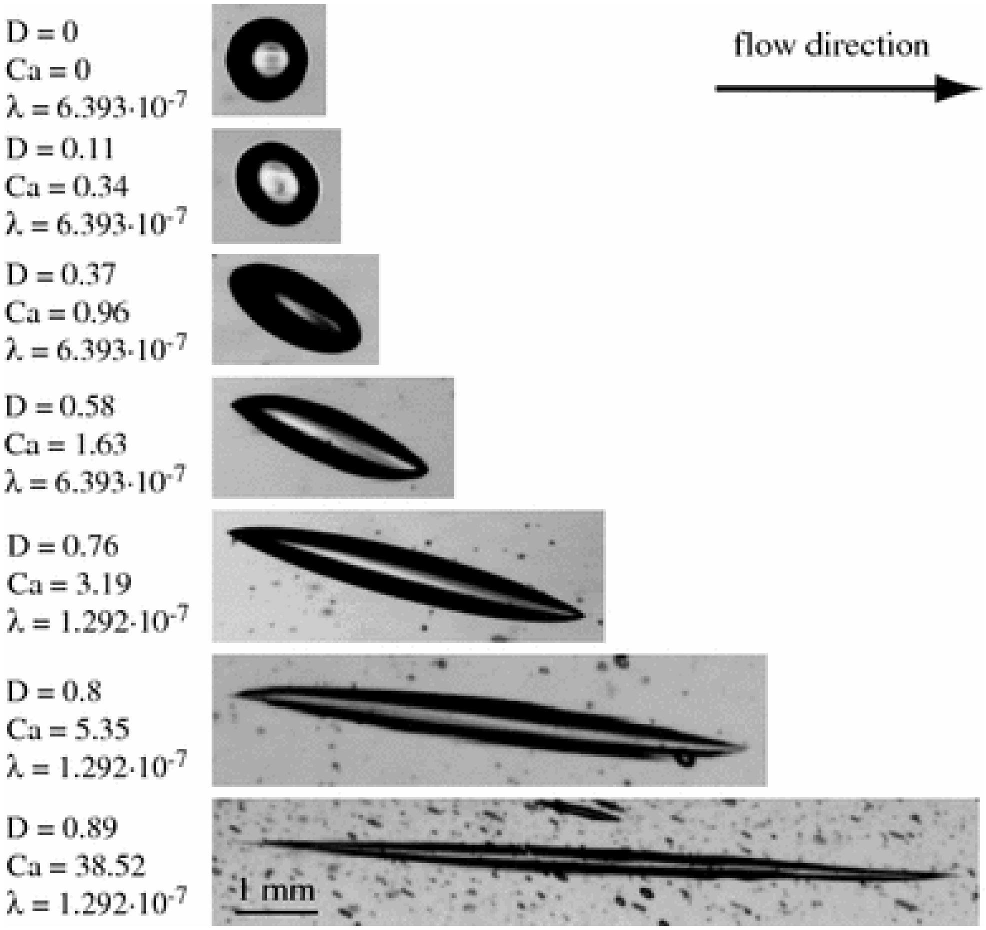

Figure 6: Maximum steady state bubble deformation and orientation (from Miller-Fischer *et al.* (2008)

Several modes of breakup are found in the presence of shear. Janssen *et al.* (1994) report that for shear rates that are near critical, breakup occurs in two equally-sized fragments and a few much smaller satellite droplets. This is consistent with the observations by Grace (1982) and Elemans *et al.* (1993). When well above the critical shear stress droplets are elongated into a long cylindrical fluid thread which subsequently breaks into a series of fragments. The work by Grace (1982) is probably the most complete, providing the bubble burst time, number of fragments and some daughter bubble size distributions. Near the critical shear stress, when the bubble breaks in two equally-sized fragments and a few satellite bubbles, there is not enough experimental data reporting the size of these satellite bubbles.

For the experiments performed in this work, single-phase CFD simulations show that at 18 knots the maximum shear rate is approximately $\dot{\gamma}\ = 100{,}000\ 1/s$, though quickly decays to values between $1{,}000\ 1/s$ and $10{,}000\ 1/s$ for distance to the wall between $100\ \mu m$ and $1\ mm$, see Fig. 7. Using $\dot{\gamma}\ = 3{,}000\ 1/s$ in Eq. 6 results that a bubble with $2\ mm$ diameter reaches only 6.3% of Ca_{crit}, and would thus not breakup. However, Müller-Fischer *et al*. (2008) show that large deformations (Fig. 6) occur before the bubbles break using glucose syrup or silicone oil as continuous fluid and air as dispersed fluid (viscosity ratios $= 1.3 \sim 6 \times 10^{-7}$). For $Ca = 0.057 Ca_{crit}$ the authors report an aspect ratio of the bubbles of 3.76, and for $Ca = 0.086 Ca_{crit}$ the aspect ratio is 7.33. Though these highly elongated bubbles are still stable in a laminar flow, they probably will not be in the highly turbulent flow inside the boundary layer of a ship.

None of the experimental studies on shear-induced breakup consider the combined effect

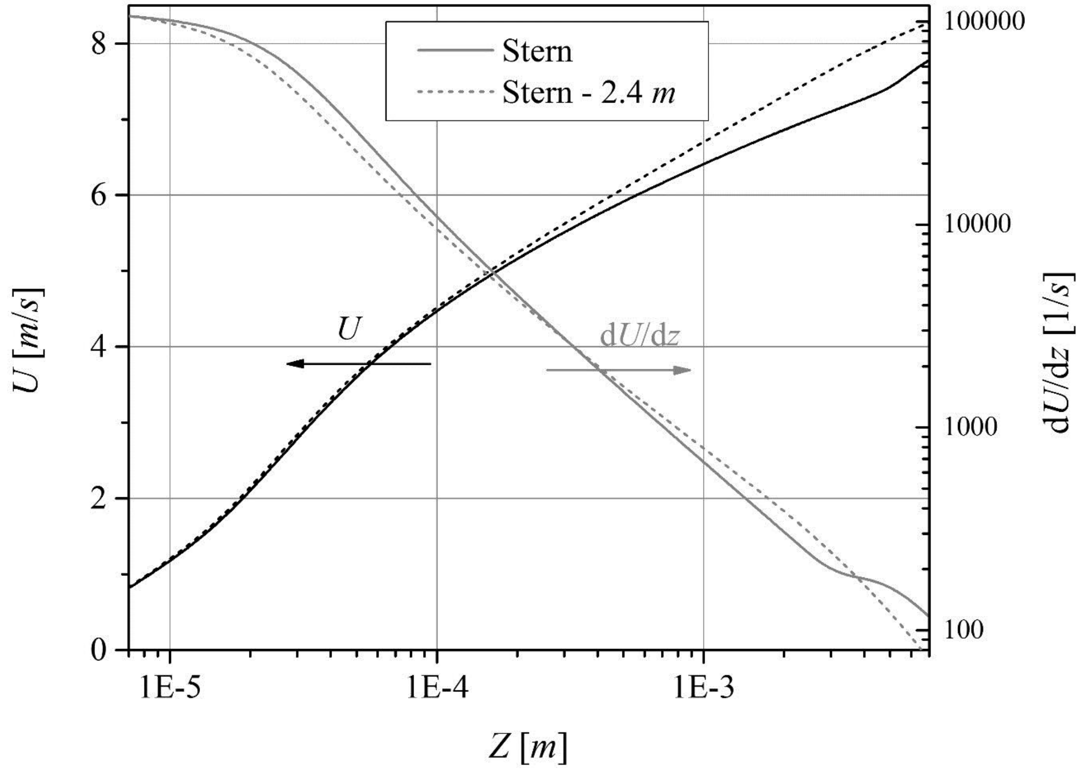

Figure 7: Velocity and velocity gradient at the stern and 2.4 m upstream of the stern as predicted by CFD for a boat speed of 18 knots

of turbulence and shear acting on a bubble. This could be of fundamental importance for turbulent boundary layers where very high shear stress and turbulent fluctuations occur simultaneously. For velocity gradients in the boundary layer that are high but not enough to break up a bubble, the added presence of small vortices unstabilizing the interface could result in bubble breakup. In a situation in which a bubble immersed in a shear velocity field suffers an affine deformation (see Elemans *et al*., 1993; Muller-Fischer *et al*., 2008) with the capillary number below the critical value, shear-induced breakup does not occur. As described in Elemans *et al*. (1993), once the bubble has become highly extended, it exhibits small sinusoidal distortions (Rayleigh distortions) of wavelength λ_R along the thread-shaped bubble. Depending on the viscosity ratio, one of these wavelengths becomes dominant and causes the thread breakup. Distortions leading to breakup could additionally be enhanced by interactions with turbulent eddies and the critical capillary number for breakup could be significantly smaller than the laminar measured value.

1.3.2 Bubble-bubble interactions

Bubble coalescence is the joining of two or more bubbles to create one larger bubble. Bubble coalescence occurs through a three step process must occur (Marrucci, 1969; Prince and Blanch, 1990). First bubbles must come in contact with each other; then they must remain in contact with each other for sufficient time for the liquid film between them to thin; and finally the film between the bubbles needs to break which creates the larger bubble.

The coalescence source in Eq. 3 is modeled as a function of the coalescence kernel between bubbles of size m' and $m - m'$, $Q(m - m', m')$ (Castro and Carrica, 2013)

$$\chi(m) = \frac{1}{2}\int_{0}^{m} f(m-m')f(m')Q(m-m',m')dm' - f(m)\int_{0}^{\infty} f(m')Q(m-m',m')dm \qquad (7)$$

Note that in Eq. 7 the coalescence rate is proportional to the void fraction squared, which means that coalescence increases rapidly with void fraction. The coalescence kernel is produced by the product of the collision rate and the coalescence probability. The collision rate increases with the bubble radii and the turbulent dissipation, while the coalescence probability increases with the contact time, which increases with the bubble radius but decreases with the turbulent dissipation (Prince and Blanch, 1990). In a downward facing boundary layer, as occurs with the bottom hull of ships and with the experimental platform in this work, buoyancy contributes to the increase in the void fraction and contact time by pushing bubbles against the hull. The high levels of turbulence, coupled with the number of bubbles, increase the likelihood of bubble collisions favoring coalescence to occur.

The study of surfactants and electrolytes on the coalescence rate of bubbles has been well studied (Weissenborn and Pugh, 1995). Electrolytes, in specific sodium chloride (salt) is well known to inhibit coalescence and consequently plays a role in the final size distributions of bubbles found in a ships wake when operating on salt water. The exact mechanism of coalescence inhibition is not fully understood, but hypotheses including: the increase in surface tension of water when salt is present, reduction in electrostatic repulsion, and reduction in the hydrophobic attraction (Weissenborn and Pugh, 1995; Craig *et al.*, 1993).

1.4 Motivation

The ability to measure two-phase flow parameters is of particular importance in fluid dynamics. The theoretical prediction of two-phase flow parameters still lacks in ability compared to its single phase counterpart. It is for this reason and the general broad scope of two-phase flows, that the continued research in two-phase flow instrumentation is so prevalent. The lack of scaling in two-phase flows also poses a fundamental problem when performing experiments and requires that full scale experiments be performed. With this in mind, this thesis focuses on the development of micro phase detection probes that have the ability to be used in full scale environments and their use in measurements in a full scale environment.

The objective of the experimental case study was to gain experimental evidence on how the processes occurring in a full scale boundary layer affect the spatial evolution of void fraction, bubble size and other relevant multiphase flow quantities, providing a dataset useful for validation and calibration of modeling and computational fluid dynamics (CFD) of ship bubbly flows. The experimental platform used is a flat bottom survey Kann boat, with details given in §2.2. Experiments were performed both in fresh water and salt water, since it is known that surfactants in general and salinity in particular, affect the bubble coalescence rate and consequently the bubble size distribution (Cartmill and Su, 1993; Craig *et al.*, 1993).

1.5 Multi-phase measurement techniques

Quantities of interest, such as void fraction, interfacial area density, interfacial velocity and size distribution can be measured with a number of different techniques. Broadly, the techniques can be broken up into two categories, intrusive (also known as local) and non-intrusive techniques. Intrusive phase detection probes are intended to pierce bubbles and droplets in a two-phase flow and directly measure the quantities of interest. Non-intrusive techniques rely on either the changing characteristics of multiphase flows to deduce or measure the quantities of interest or the detection of bubbles using various properties of bubbles.

A brief background of these techniques is presented next along with a summary of their strengths and limitations.

1.5.1 Intrusive optical phase detection probes

The principles of operation of intrusive optical phase detection probes lay in the ability to distinguish between air and water based on their physical properties. Historically, three primary configurations of probes have been used, the glass rod probes, fiber bundle probes and the U-shaped fiber probes. Early U-shaped probes relying on sharp bends in glass fibers to reflect light led to the development of glass rod style optical phase detection probes. Glass rod probes operate by piercing a bubble in an air-water two phase flow and capturing the changes in light reflected back from the probe (Miller and Mitchie, 1969; Danel and Delhaye, 1971; Bell *et al.*, 1972). Single tip probes can directly measure void fraction while double tip probes can measure velocity and size in addition to void fraction.

The Snell-Descartes refraction law:

$$n_f \sin i = n_k \sin r \tag{8}$$

is used to describe the principle relationship between light passing through mediums of different indexes of refraction. Referring to Figure 8, light is emitted from a probe with a core index of n_f into the surrounding medium with refractive index of n_k. In air, total internal reflection occurs so long as i is larger than critical angle i_c:

$$i_c = \arcsin\left({}^{n_k}/_{n_f}\right) \tag{9}$$

In water, the light coming to the tip is refracted into the water, with the tip acting as a Descartes prism. For a glass probe with refractive index of $n_{f,glass} = 1.62$ and using an angle $i_c = 45°$, internal reflection occurs at $n_k < 1.15$ and refraction at $n_k > 1.15$. Air and water have indexes of refraction of $n_{k,air} = 1$ and $n_{k,water} = 1.33$, respectively. Using a photodetector, reflected light in air can be measured, and using a double threshold, whereby the first threshold is applied to the rising slope of the signal to signify the start of a bubble and the second to the falling slope to signify the end of a bubble, a phase indicator function, Eq. 10, created (Cartellier, 1990) where **r** is any point in space and *t* is the time.

$$\chi(\mathbf{r}, t) = \begin{cases} 1 & if\ the\ probe\ tip\ is\ in\ air \\ 0 & if\ the\ probe\ tip\ is\ in\ water \end{cases} \tag{10}$$

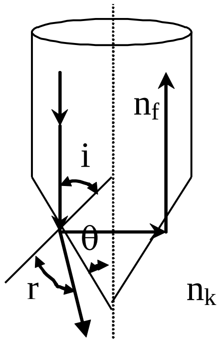

Figure 8: Optical probe schematic of total internal reflection (air) and refraction (water)

While this simple model explains the fundamentals of how an optical phase detection probe operates, the design and successful implementation relies on a number of additional considerations. The angle of a probe tip measured from the center-line of the tip axis-symmetrically to the cones' edge can have a large influence on both the light reflected back, and hence the sensitivity of the probe, as well as the strength and longevity of the probe in an experimental setting. Phase detection is possible with angles from θ=90 (a blunt tip) to θ=a few degrees, which go beyond the limits set by Eq. 9(Cartellier and Achard, 1991). The balance of the advantages and disadvantages of tip design is covered in greater detail in §2.1.1.

Closely coupled to the tip angle is the values used for the double threshold, Eq. 10. A critical amount of light must be reflected back prior to being detected by the photodetector as a probe pierces a bubble. While the amount of light is minimal, the probe tip *must* be in air before *any* light is reflected back. Similarly, as the probe exits a bubble, 're-wetting' of the probe tip takes a finite amount of time prior to the light being refracted into the water and the photodetector no longer registering reflected light. Zun *et al.* (1995) have performed a thorough analysis on these phenomenon and addressed their respective behaviors on various processing techniques. These considerations are discussed and quantified in the signal processing and uncertainty of the probes in §2.1.7.

Attempts have been made at using the aforementioned properties to directly measure bubble velocities (Barrau *et al.*, 1999; Cartellier and Barrau, 1998). Using the rising slope of the reflected light will yield a bubble velocity that is proportional to the slope of the signal. The limiting factor of this technique is the influence of the bubble size and the angle that the bubble is pierced. In the case of a normal plane of air approaching the probe, the slope – to – velocity ratio would remain the same. When the plane of air is no longer normal, but pierced at an oblique angle, the slope – to – velocity ratio will change. If the oblique angle is well know this can be calibrated for, but is clearly a limiting factor in real world bubbly flows, where bubbles can be pierced at any infinite number of angles. This technique is more thoroughly discussed in Chapter 3.

In an effort to reduce the size of optical probes of the era, Danel and Delhaye (1971) used a single 40µm fiber bent into a ‘U’ shape. One of the fiber’s ends was attached to a light source and the other to a phototransistor. The active region of the fiber defined by the outer edges of the ‘U’ shape was on the order of 100µm, compared to 500µm of the fiber bundle of Hinata (1972) and 300µm of the glass rods of Miller and Mitchie (1969). Using the same characteristics as glass-rod probes, the tight bend in the fiber acts in effect as a tip, with light either reflected through the fiber in air or refracted into the water.

A fiber bundle probe created by Hinata (1972) used an array of a few hundred 30µm fiber optic cables bundled together. The fiber bundle, polished square at the end, was attached to a 500µm glass rod coated with a cladding material to aid in internal reflection, which was also polished square. The fiber bundle consisted of both light emitting fibers and light returning fibers which were separated at a ‘Y’ junction. Using the same properties of glass rod probes, though intended for mercury-air flow, light, from a lamp at one end of the ‘Y’, is reflected back when the probe is in the liquid metal and scatters into the surrounding air when in air. A photo transducer on the other end of the ‘Y’ was used to receive the returning light and processed into a phase indicator function.

1.5.2 Non-intrusive optical measurement methods

Systems similar to the UTC bubble size analyzer (Randall *et al.*, 1989) have been used in various applications where the flows are constrained to tubes and pipes such as Chen *et al.* (2001) and Yianatos *et al.* (2001) This fundamental technique involves using two or more phototransistors to develop a similar signal to the phase indicator function, Eq. 10, as the bubbles pass through a measurement domain. The measurement domain consists of a capillary tube that the bubbles travel through. Signals generated by the phototransistors are stored to memory where various processing schemes can be applied to them. The ability to measure both velocity and bubble size requires that the measurement domain acts purely in a passive way and has minimal effect on the natural flow of the liquid and bubbles.

More active methods exist, such as capillary suction probes (Garigou and Greaves, 1991), where an active vacuum is maintained on a capillary tube. The capillary tube is used to continuously withdraw a small stream of gas-liquid mixture through a funnel-shaped opening. The mixture then passes through an array of photodetectors where, along with knowing the capillary diameter, the bubble sizes can be measured. The selection of the diameter of capillary tube is important in these methods, as it is desirable for the bubbles to turn into slugs (coalesce until the bubble size approaches the diameter of the capillary tube) within the capillary, which yields more accurate measurements (Garigou and Greaves, 1991). The capillary suction probes do not have the ability to measure velocity, as the act of withdrawing the bubbles from the flow adversely affects the local velocity.

Visual based optical phase detection typically involves the use of cameras with high shutter rates under constant illumination or long exposure cameras with pulsed illumination (Hsu *et al.*, 1969; Grau and Heiskanen, 2002; Chen *et al.*, 2001; Terrill *et al.*, 2005). The use of visual methods requires that the flow be highly accessible (or channeled to a viewing area) and sufficiently clear to be visualized. If properly calibrated, these systems can provide comprehensive and accurate results in void fractions, bubble velocity and size.

The processing of visual methods can become computationally expensive. Image frames must be individually analyzed with criteria set to distinguish between the phases and often requires additional criteria to separate any debris that can be captured in the images. The computation of bubble sizes and void fraction can be computed by individual frames. Computing velocity requires processing of sequential images with tracking of either bubble interfaces or bubble centers. The strength of these systems is the ability to directly measure both the bubble size and shape with minimal error. In the realm of bubbly flow measurements, the ability to directly measure bubble sizes has led to some unique combinations of equipment. Terrill *et al.* (2005), wanting to measure in the wake of a full size naval ship went to extensive measures to adapt a lab based piece of equipment to cope with the elements encountered in the wake of a ship. While highly accurate, the sheer size of the necessary equipment has limited the wide spread use of these systems.

1.5.3 Conductive based phase detection

Conductivity probes can be used to measure bubbly flows using the differences in electrical conductivity of air and water. Neal and Bankoff (1963) were the first to pioneer conductivity probes and their use to measure two phase flows. Numerous design and improvements have been made based on the ability to measure the impedance signals from each of the probe tips. Single, double and four sensor probes have been widely deployed to measure both bubbly and slug type two phase flows, see for example Kim *et al.* (2000), Kataoka and Ishii (1984) and Terrill *et al.* (2005). A processing algorithm similar to that of optical phase detection probes is used, where-by the return signal when a probe tip is in air varies from that of the probe tip in water. A phase indicator function Eq. 10 is created, and stored for post processing. A review by Le Corre *et al.* (2003) has shown that both optical and conductivity probes show reasonable agreement under similar flow conditions with similarly sized probes.

More recently, the use of wire mesh probes has given the ability to recreate bubble distributions at a given point in space and time throughout the entire measurement domain of a pipe (Prasser *et al.*, 1998; Prasser *et al.*, 2001). The methodology developed by Prasser *et al.* (1998) uses an array of wires spaced equidistant from each other throughout a pipe's cross-section. As clouds of bubbles pass through the array of wires, the conductivity between each pair of wires is measured with respect to time. Hence, the size and residence time of each bubble passing the plane of wire mesh can be measured. The device created was limited to laboratory flows, but addressed the very difficult problem of measuring an entire cross section simultaneously to get both bubble sizes and their distribution within a pipe.

Nonintrusive conductivity devices have the ability to measure special averaged flow properties such as void fraction. Most systems use, at a minimum, a pair of electrodes and measure the changing impedance of the flow (Ceccio and George, 1996). Measuring in a fluid with constant properties is essential with this technique. Variations in salinity or particulate matter could result in the change of conductivity, which could be perceived as a change in void fraction and hence throw off the measurements. Recently the use of multiple electrodes along a pipe has given the ability to deduce the velocity of a mixture in addition to the void fraction as clouds of 'void' travel from one pair of electrodes to another (Jin *et al.*, 2008).

One of the fundamental limitations of both intrusive conductivity, optical and UTC style systems is that the processing schemes require a degree of subjective processing. While the theory is well understood, the wetting and de-wetting times pose a fundamental error, which is dependent on both the bubble velocity and the shape of the probe tips (Delhaye and Chevrier, 1966). This problem often necessitates the use of a calibration procedure which must be individually applied to each probe.

1.5.4 Hot-wire / hot-film probes

Hot-wire/hot-film anemometers have been extensively used in two phase flows (Hsu *et al.*, 1963; Goldschmidt, 1965; Delhaye, 1968). Hot wire anemometers work by maintaining the wire at a constant temperature and monitoring the current required to maintain that temperature. In air less current is needed to maintain a set temperature than in water. Measuring the void fraction using a hot-wire anemometer is a simple process of integrating the time the sensor is in air with respect to the measurement duration. Directly measuring the velocity of bubbles requires that the sensor wire be extremely sensitive and the probe temperature set properly to prevent degassing air bubbles from growing on the sensor. Further care must be taken to avoid fluctuations in the fluid temperatures. These two necessities mandate that the wire be of a thin gauge and hence is most suitable for lab flows. The primary advantage of hot-wires over the previously mentioned local phase detection methods is that they work regardless of the fluids conductivity or optical properties.

1.5.5 Radiation absorption, acoustic and other method

Radiographic techniques are a non-intrusive void fraction and void distribution measuring method. There are numerous configurations, but all rely on the same basic principles. A radioactive source (typically Cesium-137, Thalium-170, Iridium-192 or Selenium-75) is focused through a test section; water in the test section attenuates radiation without a significant amount of energy being deposited. The void fraction is the percentage of the flow channel volume not occupied by the water; measuring the attenuation of the radiation beam can detect the void fraction in the test section (Harvel *et al.*, 1996). Collectively, the radioactive methods provide an accurate method to measure void fraction, as long as the radioactive source remains strong.

Acoustic methods use the changing velocity of sound to deduce void fractions. Sound velocity through a two-phase mixture depends primarily on the void fraction and, to a lesser extent, on the void size. Acoustic techniques lend themselves to measuring two phase flows in which void fractions are low and in conditions where large measurement domains are desired, such as the far wake of ships or general oceanographic measurements (Trevorrow *et al.* 1994; Vagle and Farmer, 1998).

Visual light scattering techniques measure the concentration of particles based on the signal attenuation effects of light absorbed and reflected from the dispersed phase (Becker *et al.*, 1967). Though implemented primarily for solids in fluids, similar effects can be seen with micro bubbles in fluids.

Some additional techniques that use similar properties as the aforementioned methods include, electro-magnetic metering, microwave absorption, nuclear magnetic resonance, and infrared absorption.

CHAPTER 2: DUAL TIP COMPOUND ANGLE PROBES AND APPLICATION TO KANN BOAT

2.1 Probe Development

An in depth design, and the operation and signal processing of the optical phase detection probes is presented below. Note that the details given pertain to many two-phase flow types, but are tailored to the application of measuring in the high shear, turbulent flow of the Kann boat which was operated in conditions where many debris were present.

2.1.1 Probe tips

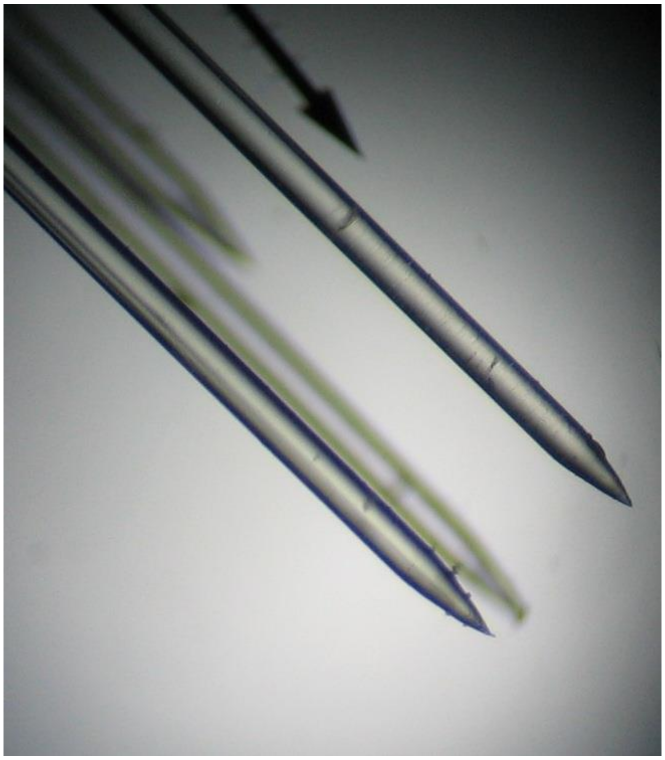

Figure 9: A 4-tip glass probe made by the author

In a controlled laboratory environment, the design and implementation of probe tips poses few challenges in terms of achieving long life and ability to accurately measure bubbles. Miller and Mitchie (1969) and Danel and Delhaye (1971), among others, laid the foundation for intrusive optical phase detection probes which resulted in the extensive use of glass fiber probes in laboratory settings; see for example Hoschek *et al.* (2005), Hong *et al.* (2004) and Blenkinsopp and Chaplin (2010). Early in the development of the latest generation of probes, glass fiber optic cable was used in designs similar to those of Le Corre *et al.* (2003). Following the work of Takahashi (1990), glass fibers were acid etched to a conical shape and placed to provide the ability to measure in 3 principle directions (Fig. 9). This probe was used in the preliminary measurements that is the topic of Perret *et al.* (2013), Perret and Carrica (2011) and Perret (2013).

The glass fiber probes have been used in numerous studies and applications due to their ease of manufacturing, simple implementation and the wide-spread availability of the principle materials (fiber optic cables). The primary problem encountered with glass fiber probes is the lack of strength of the glass itself. Even in a laboratory setting, with minimal contaminants, glass fibers have a tendency to break. Sapphire (the crystalline form of Aluminum Oxide, Al_2O_3, also known as Corundum) can be made to have the necessary optical properties to be used in phase detection, and has the additional characteristic of being one of the hardest materials known.

Commercially available probes made from Sapphire are available from RBI (Milan, France) and have successfully been used in full scale experiments alongside in house (IIHR) built Sapphire probes by Johansen *et al.* (2009). The RBI probes are made from a pair of 375 µm Sapphire rods, which are polished down to approximately 30 μm at 15° with a final rip angle of 45°. The two tips are placed in line with each other offset by a given distance. The IIHR probe (Johansen *et al.* 2009) used a pair of 125 μm fibers polished at 45° and placed parallel and touching one another at a given offset (see Figure 10).

Figure 10: Scale comparison of RBI probe (left), IIHR probe (middle, Johansen *et al.* 2009) and probes developed in this thesis

The probes available from RBI (Milan, France) and the ones made by Johansen *et al.* (2009) were effective in their measurements, but they had limitations. The effective tip diameter, which is a measurement of the cross section that a bubble sees when it is pierced by the second tip in a two-tip probe design, posed as the majoring limiting factor in their designs. Minimizing the effective tip diameter is highly desirable due to the ability it gives in measuring smaller bubbles and reducing the influence the probe has on the surrounding flow. The method that RBI uses to deduce the effective tip diameter is to have the two tips angle towards each other, and oriented such that they are in line with the flow direction. This method puts the second probe tip directly downstream of the first. Despite the tips being in line with each other, a common occurrence is to have the bubble follow the trajectory of the leading tip, which in turn draws the bubble away from the second tip. This is most evident when the bubbles pierced are small, compared to the diameter of the Sapphire rod. When this occurs, the second tip typically does not register any bubble being pierced and hence bubble velocity and chord length cannot be computed. The method used by Johansen *et al.* (2009) to reduce the effective tip diameter simply involved the use of smaller diameter Sapphire fibers in place of the Sapphire rods used by RBI. With this method the minimal effective cross section area is approximated by:

$$A_{eff} = \left(\frac{3D_f}{4}\right)^2 \pi \tag{11}$$

with D_f being the fiber diameter. The minimal effective cross section also serves as a metric as to the smallest bubbles that can be measured and can be approximated to have the diameter of 1.5 times the fiber diameter. While this minimal diameter is theoretically correct, there are a number of potential circumstances that can prevent bubbles of that size being pierced. Primarily, in order to attain a proper signal contrast between air and water the entire probe tip must be surrounded by air. While a bubble of diameter 1.5 D_f would be completely pierced by the forward tip, it would most likely only graze the second tip.

One objective of the probe development process was to reduce the effective cross sectional area of the probes, to allow for the measurement of bubbles expected in the boundary layer of the Kann boat. Using a double angle polishing technique developed for this thesis, double tipped probes able to measure 50 µm bubbles were manufactured. Starting with 210 µm Sapphire fibers available from Micromaterials (Tampa, FL), each fiber tip was polished using diamond lapping film at a 5º axis-symmetric taper to reduce the effective fiber tip diameter to 20 µm where a 45º angle is polished (see Fig. 12). The taper is used to reduce the effective diameter of the fiber while maintaining adequate strength and the 45º maximizes the contrast of the light signal. Each fiber tip is then mated with optical gel to a 210/240 µm glass fiber optic cable within a piece of stainless steel capillary tubing and is housed in a stainless steel carrier. The stainless steel carrier is then filled with epoxy to further secure the coupling and reduce damage from vibrations and impacts. Upon completion the probe tip-to-tip distance was measured using an optical comparator. The fiber optic cables terminate with an industry standard ST connector which allows them to be used with a variety of electronic units.

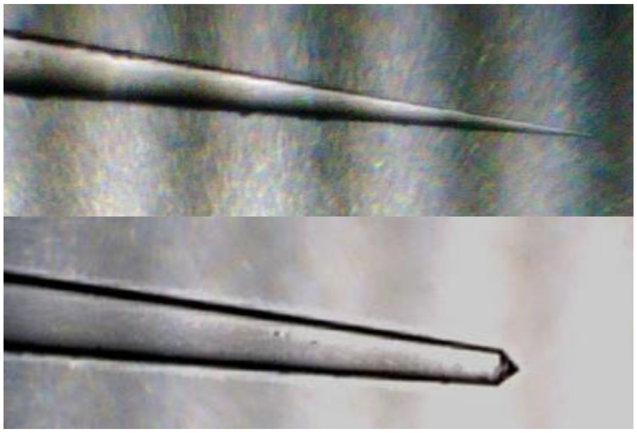

Figure 12: Probe tips at two steps in the building process

The two tips, separated by a known distance, are joined such that the taper on each tip is parallel and touching the other. This ensures that any bubble pierced is minimally affected by the probe itself and adds a level of confidence in the computation of bubble velocity, as the

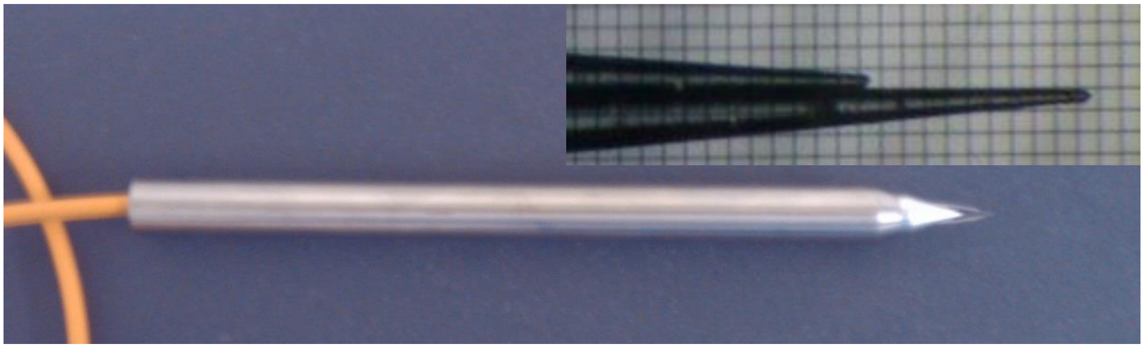

Figure 11: Completed double tip probe. Detailed tip against 50 µm grid

likelihood of a second bubble piercing the second tip prior to the first bubble is dramatically decreased. The added benefit of having the tips joined in this fashion is that the cross section that the bubble sees is minimized and the mechanical strength of the tips is increased.

2.1.2 Details of probe manufacturing

The methods used in the construction of the sapphire tips of the optical phase detection probes are described in detail below. While there are many methods that can be used to shape sapphire, the methods described below achieve a balance in maintaining accuracy, speed of shaping and ease of use. The tradeoffs in various aspects of the probe shape and designs are also described below and how they pertain to the bubble measurements carried out on the Kann boat.

The fiber tips are made using an abrasive manufacturing technique that was pioneered by Johansen *et. al.* 2010 and has since been refined to reduce tip runout, which is the eccentricity of a rotating object, and allow more control in the geometry of the tips. Much time has been invested in eliminating the runout of the working end of the sapphire. Runout is caused by the quality of the sapphire fiber that is available for purchase, and the machine tools that are used to hold the fibers. Since the sapphire fibers come from a single source, there is little that can be done to correct the off center and the asymmetries of the fibers. A micro collet made by Big Daishowa (Mega Micro Chuck) is used to hold the fibers. The micro collet is held in a lathe with a precision ground adapter, made specifically for this purpose. Typical runout on the collet once indicated, which is the process of finding the collet center and making it coaxial to the adapter, is $< 0.0001''$. In an effort to reduce the effect of the eccentricity of the sapphire fibers, the fibers are held as closely to the exit of the collet as the grinding and polishing fixtures allow.

Shaping the fibers is achieved using abrasive diamond lapping films. A simple rotating polisher is attached to an angle plate that is set parallel to the vertical centerline plane of the fibers. The taper angles on the fibers are thus controlled by setting the angle plate at the desired angular rotation. Traversing the angular plate to and away from the fiber controls the size of the angular features on the fibers. A typical grinding and polishing schedule starts with $30\ \mu m$ grit lapping film used as a course/fast material removal abrasive and followed with $10, 3, 1$ and $0.5\ \mu m$ films. Water is used as a lubricant and cleaner to reduce clogging of the lapping film and achieve a better final polish.

As discussed above in §2.1.1, the primary taper angle was selected to be 5º. The angle is a balance between strength of the fiber and minimizing the effect of the probe on the bubble traveling up the length of the tip. Using a smaller angle decreases the effects of the probe on the bubble at the cost of strength and, to a lesser degree, increased manufacturing time. The details of the deformation caused by the probe tips is covered in greater detail in Chapter 4. The taper angle, along with the final polish, play a role in the characteristics of the return signal from the probe tips. The necessity for a fine 'mirror' polish helps in guiding more light down the fiber to the active 45° region of the tip. If a rougher polish is used (eg. $> 3\mu m$ instead of $0.5\mu m$), the incident light that strikes the sections of the 5° taper is lost through the rough interface and cannot contribute to the return signal. These details are also covered in greater detail in §3.4.

The tip-to-tip distance of a probe is a compromise in the accuracy of measuring the velocity (and hence chord length) and in the minimum size of bubble that can be pierced by the first and subsequently, the second tip. The main factor in error of the bubble velocity (Eq. 20, §2.1.7) is the uncertainty of the tip-to-tip distance. The larger the tip-to-tip distance, the less influence its errors become in the computation of velocity. As the tip-to-tip distance decreases, the opposite is true, and the relative error increases significantly.

The most noticeable trade-off in long tip-to-tip distances is the interference that the first tip's taper has on the trajectory of small bubbles. The smallest bubbles that can reliably be pierced by the first tip are often stretched and deformed by the first tip's taper to the point that they are guided away from the axis of the probe by imbalances in the surface tension around the perimeter of the bubble caused by non-coaxial bubble pierces and the nature of the double-tip probe geometry, which is not axisymmetric. An illustration of this can be seen in Fig. 13, where an approximately $200\mu m$ bubble is pierced by a probe with a tip-to-tip distance of $524\mu m$. The bubble can be seen to strike in a nearly perfect orientation, on center with a longitudinal velocity vector in line with the primary tip. Details of the entire piercing process are described in Chapter 4. What is noteworthy in the context of probe design is what occurs when the bubble reaches the second tip. As the bubble was pierced on centerline, the bubble has a tendency to 'follow' the primary tip, which leads it to the second tip. The deformation in the bubble causes the bubble to form more of an oblique ellipsoidal shape rather than maintaining a spherical shape. When the bubble reaches the point of contact with the second tip, the deformation has become significant enough that the increased surface tension and pressure forces cause the bubble to be pushed away from the second tip. This results in inaccuracies in the measurement of the bubble velocity. Decreasing the tip-to-tip distance has the benefit of having the bubble strike the second tip before significant deformations can occur.

The Young-Laplace equation relates the pressure difference across the interface of a bubble to the radius of curvature of the bubble by:

$$\Delta P = \gamma\left(\frac{1}{R_1} + \frac{1}{R_2}\right) \tag{12}$$

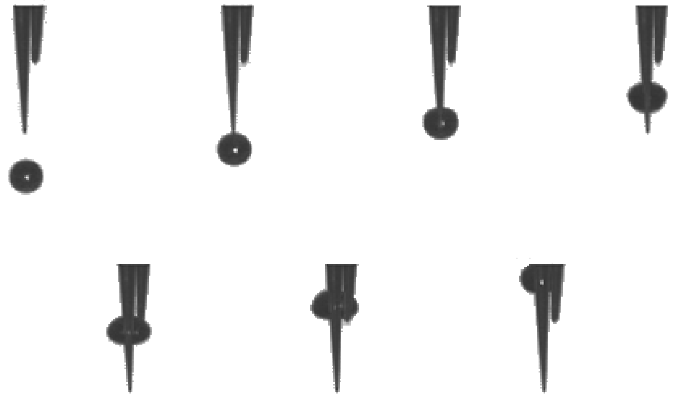

Figure 13: Single bubble piercing

where ΔP is the pressure difference across the fluid interface, γ is the surface tension and R_1 and R_2 are the principal radii of curvature. In Fig. 13, initially the bubble has principle dimensions of $R_1 = R_2 \approx 100\mu m$, which equates to a pressure difference of $1.4\ kPa$. At the point where the bubble encounters the second tip, the volume occupied by the segment of the probe tip equates to approximately 22% of the initial volume of the spherical bubble. The deformation of the bubble, assuming it remains symmetric about the axis of the probe tip (having the shape of a circular ellipsoid), has $R_1 \approx 62\ \mu m$ and $R_2 \approx 134\ \mu m$ equating to a pressure difference of $1.7\ kPa$.

The active tip size requires some consideration as well. Defined by the 45° angle, it has a significant effect on the initial deformation of smaller bubbles and the intensity of light that is returned when the probe is in air (total internal reflection). Increasing the size of the active tip increases the available surface area to directly reflect light in the fiber, and consequently makes the tips more sensitive and easier to detect the contrast between air and water. Note that there are diminishing returns to increasing the surface area to the active tip; this is reached as the saturation point of the photodetector is reached. The tradeoff comes in the amount of deformation the large active sizes cause, which is most evident in smaller bubbles. As the small bubbles, which have minimal virtual mass, encounter the active tip, which is comparatively blunt, they have a tendency to either bounce off the tip or to significantly deform. The probes used in the Kann boat experiments had active tips between $15 - 30\mu m$. With this size, bubbles in the $50\ \mu m$ can be reliably pierced, and is the source of the self-imposed size limit in §2.1.1. Larger bubbles ($R_{1,2} > 375\ \mu m$), which carry more virtual mass, and having less surface tension force to resist piercing are not affected by the size of the probe tips.

2.1.3 Electronics

Optoelectronic units provided by RBI (Milan, France) were used for the acquisition of the phase indicator function. Each optoelectronic unit contains an infrared laser light source coupled to a 50/50 optical coupler and then through a fiber optic cable to the probe. The light reflected back (§1.5.1) is picked up by the coupler, which is then sent to a photodiode. The electric signal of the photodiode is amplified and then sent to the analog output and to a comparator that generates a digital signal, with a resolution of approximately 1 μs, which is read by a PC and stored for processing. The comparator operates on an adjustable double threshold, with low and high levels adjusted via potentiometers. Threshold values are set based on a 5 V signal in air and 0 V signal in water. Typical threshold values are between $0.5 - 1.5\,V$ $(0 - 30\%)$ for the low level threshold and $3.5 - 4.5$ $(70 - 90\%)$ for the high level threshold.

2.1.4 Signal conditioning

The digital signal coming from the optoelectronic units often require a degree of conditioning to filter certain un-natural signals. Examples of un-natural signals include extended periods in air, which can result if the probe breaches the surface of the water and results in bubbles that are on the order of meters long. Such occurrences are removed from the phase indicator function. High frequency noise can also become prevalent when vibrations from the boat cause brief interruptions in the junction between the fiber optic ST connectors and the optoelectronic units. An example of this is shown in Fig. 14, where vibration cause the returning light to fall below the threshold that would otherwise indicate the probe tip being in air. These are removed from the signal with the indicator function placed at its proper value (1 – if in air, 0 – if in water).

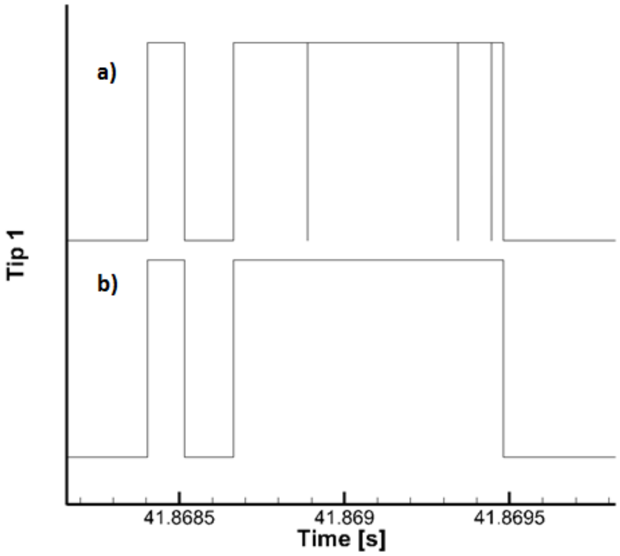

Figure 14: Noise in signal prior to filtering (a) and post filtering (b)

2.1.5 Signal processing

Dual tip probes work by measuring the phase indicator function at two tips with a known distance (L) between them, as can be seen in the idealized schematic in Fig. 15. The cross-correlation velocity:

$$U_{corr} = \frac{L}{\tau_d} \tag{13}$$

is computed in a given integration interval using the maximum of the cross-correlation time delay:

$$\tau_d = \underset{t}{\operatorname{argmax}}[x_1(\boldsymbol{r},t) \cdot x_2(\boldsymbol{r},t))(t)] \tag{14}$$

between the two probe tip indicator functions and the probe tip distance. In Eq. 14, argmax is the argument of the maximum, which is the point where the function value is maximized, and in the case of the cross-correlation, the function is the sliding dot product of the indicator function from the first and second tip with respect to time. Computing the cross-correlation velocity is done to aid in the ‘finding’ of bubble pairs. In the high velocity flows with small bubbles present experienced, it became evident that overlapping signals can occur. This results in multiple possible bubble pairs, where by one bubble would have a very high velocity and the other a very low velocity, which is un-physical for the flow conditions experienced. To eliminate this, bubbles pairs that form velocities within a window of the cross-correlation velocity are considered prior to bubble pairs outside the cross-correlation window. Once a bubble pair is found, the velocity of an individual bubble can be computed by measuring the time-of-flight of the bubble’s air/water interface between the two tips for both the bubbles leading (rising) edge and trailing (falling) edge:

$$V_{tof(r,f),i} = \frac{L}{t2_{(r,f),i} - t1_{(r,f),i}} \tag{15}$$

Taking the average of the leading and trailing edge of each bubble yields a time of flight velocity for each bubble, that is then used to compute the mean bubble velocity for each location measured:

$$U_{tof} = \frac{1}{N}\sum_{i}^{N} V_{tof,i} \tag{16}$$

The cord length of the bubble can be determined by using the bubble velocity and measuring the time in air of each of the probe tips (Δt):

$$cl_{(1,2),i} = V_i(t1,2_{i,-} - t1,2_{i,+}) \tag{17}$$

Using the average chord length of the two tips, the mean chord length is computed by

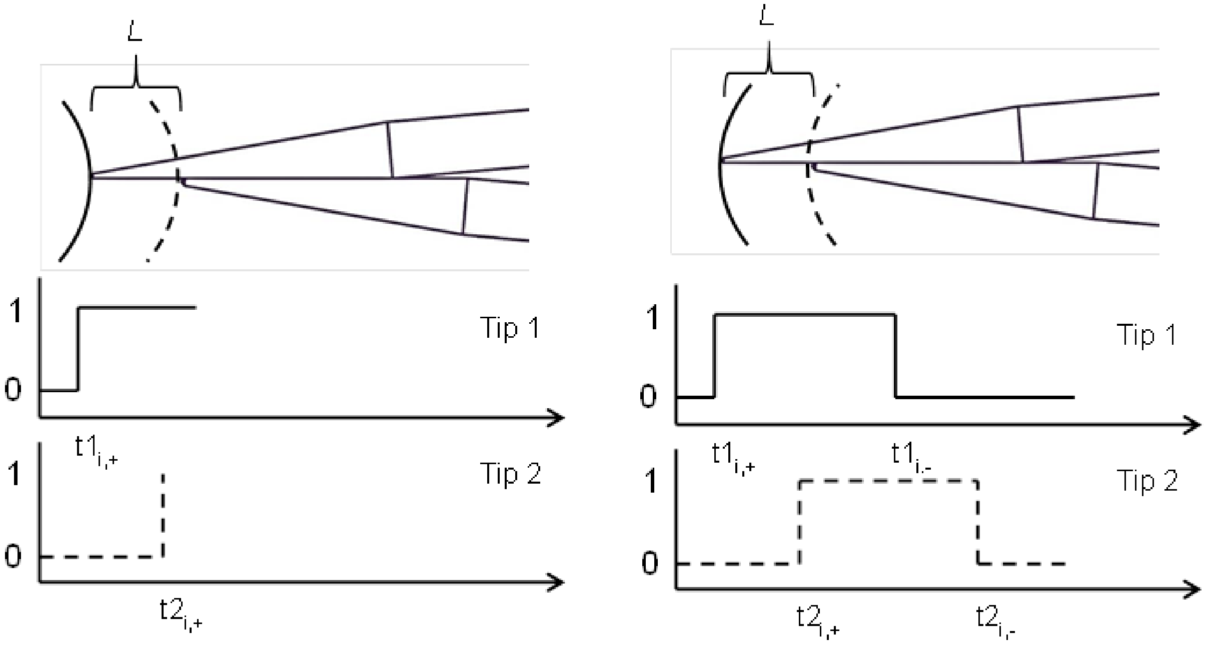

Figure 15: Idealized bubble piercing and measurement of bubble duration time and leading and trailing edges of a bubble

$$CL = \frac{1}{N}\sum_{i}^{N} cl_i \qquad (18)$$

Note that the cord length of the bubble simply corresponds to any straight line that bisects the bubble, which usually is smaller than the bubble diameter, but may be longer than an equivalent spherical bubble, in the case of an elongated bubble. Assuming that all bubbles are spherical, a bubble size distribution may also be computed using an unfolding technique described in §2.1.6. The time averaged void fraction is computed from the indicator function with:

$$\alpha(\boldsymbol{r},t) = \frac{1}{T}\int_{t-\frac{T}{2}}^{t+\frac{T}{2}} x(\boldsymbol{r},t)dt \qquad (19)$$

where T is an integration period where the averaged void fraction is reported.

2.1.6 Bubble size distribution

Chord length distributions are comprised of counts of chord lengths, Eq. 17 that fall within the chord length interval of *cl* ± *d cl* and can be directly measured. The process of finding bubble size distributions from chord length distribution is known as unfolding and can be undergone with a few key assumptions. Multiple methods have been proposed in literature that addresses various aspects of their targeted flows (Clark and Turton, 1989; Liu *et al.*, 1998; Johansen *et al.*, 2010). The main difference between chord length and bubble size distributions comes from the probe detecting larger bubbles more easily than smaller bubbles due to their larger cross-section. Additionally, bubble sizes that contribute to each count in a given chord length interval can either have a diameter of $D = cl$, when the probe pierces a bubble through the center, or $D > cl$, when the probe pierces a larger bubble through a side such that the measured chord length is still *cl*.

Clark and Tutron (1989) addressed the unfolding process for bubbles of various shapes and propose a number of parameters to correct for the various shapes. Their method is limited to regular bubbles size distributions, where the contribution of larger bubbles to smaller chord lengths is well defined and can be geometrically quantified. Liu *et al.* (1998) expanded the methods to address bubbly flows for non-uniform bubbling systems, where bubbles are not only non-uniform in size, but also in space. Johansen *et al.* (2010), using similar, but larger optical probes as this experiment, addressed a number of other issues coming from the finite bubble size that can be pierced by any given probe size. The bubble flow measured in this experiment is somewhat unique due to the high velocity gradients experienced and the proximity of the hull which can alter both the shape and size of measured chord lengths.

In this work a simplified version of Johansen *et al.* (2010) method was adopted. The primary assumption, confirmed by the results presented in §2.3.6, is that the bubble size distribution $f(\boldsymbol{r},m,t)$ quickly drops for larger bubble sizes. This allows neglecting the contribution of larger bubbles to a given chord length and use the simpler assumption $D = cl$. The computation of the impact probability corrected by cross section is still applied. As a consequence, the processing does not need to perform derivatives of the experimental chord length and results in smooth distributions, at the expense of more uncertainty in the results. However, it is believed that this uncertainty is small and acceptable, and also provide in §2.3.6 the chord length distributions so interested readers can obtain bubble size distributions using other methods.

2.1.7 Error analysis

Uncertainty in the data has been quantified following the methodology described in Johansen *et al.* (2010), with a summary given below. Systematic and precision uncertainties were estimated, with the measurement time chosen as long as possible to increase the number of bubbles measured and thus minimize the precision errors. The measurement error can be interpreted as the confidence on the ability of the instruments and experimental procedures to measure the given values for a specific sea state and boat operational condition.

The uncertainties considered in this analysis are systematic and random error, and are combined into the standard uncertainty (u_x) using the root-sum-squares (RSS) method:

$$u_x = \left(b_{\bar{x}}^2 + s_{\bar{x}}^2\right)^{1/2} \tag{20}$$

where, $b_{\bar{x}}^2$ is the RSS of systematic uncertainties, $s_{\bar{x}}^2$ the random uncertainty and $\bar{x}$ the mean of the measurement values taken.

The uncertainty in the average time-of-flight velocity (Eqs. 15 & 16) is computed as follows:

$$u_{\bar{U}_{tof}}^2 = \left(\frac{\partial U}{\partial L} u_L\right)^2 + \left(\frac{\partial U}{\partial t} B_r\right)^2 + \left(\frac{T_{\nu,95} s_V}{\sqrt{N}}\right)^2 \tag{21}$$

where u_L is the uncertainty in the tip-to-tip distance:

$$u_L^2 = B_L^2 + B_p^2 \tag{22}$$

with contributing errors coming from the measured tip-to-tip (B_L) distance as measured with an optical comparator (§ 2.1.1), taken to be 5 μm. B_p is the error in where the on the probe tip the signal rises and falls (§ 1.5.1) and is taken to be 15 μm, the longitudinal location where the 50% of the probe tip would be in air and 50% in water (by area). B_r, is the time resolution error, taken as half the data acquisition sampling rate, 0.5 μs. $T_{\nu,95}$, is the student's T value, with N-1 degrees of freedom and s_V the standard deviation of mean velocity.

The uncertainty in the average bubble chord length (Eqs. 17 & 18) is computed as:

$$u_{CL}^2 = \left(\frac{\partial cl}{\partial V} u_{U_{tof}}\right)^2 + \left(\frac{\partial cl}{\partial \Delta t} u_{\Delta t}\right)^2 \qquad (23)$$

where $u_{\Delta t}$, the uncertainty in the average time the tip is in air, has contributing factors of:

$$u_{\Delta t}^2 = B_r^2 + B_{pt}^2 + \left(\frac{T_{\nu,95} s_{\Delta t}}{\sqrt{N}}\right)^2 \qquad (24)$$

and B_{pt} is the rise and fall time error computed as:

$$B_{pt} = \frac{U_{tof}}{B_p} \qquad (25)$$

and $s_{\Delta t}$ is the standard deviation of the average time in computing the chord length Eq. (18).

The uncertainty in the void fraction, Eq. 19, is computed as:

$$u_\alpha = \frac{\partial \alpha}{\partial t} u_{\Delta t} \qquad (26)$$

where $u_{\Delta t}$ is computed from Eq. 24. The contributing errors in time and bubble count are considered negligible.

An additional source of uncertainty pertaining to the measurements taken on the Kann boat, discussed in greater detail in §2.3.2, is the variation in the measured quantities produced by changes in sea state and free surface conditions. As the sea state changes, the naturally occurring entrainment, bubble breakup and coalescence processes change. Results show that the void fraction is highly dependent on the sea roughness, with other variables less dependent. Since data has not been discriminated by sea state, this introduces an uncertainty in the results due to changing environmental conditions.

Except when noted, the error bars shown in subsequent plots represent the measurement errors for the specific dataset. Precision errors are computed using that dataset and do not include the uncertainty caused by changes in environmental conditions. The bounds of confidence for void fraction and chord length due to environmental variations are shown in Figs. 20 and 21 and can be taken as representative order-of-magnitude for all subsequent plots.

2.2 Kann Boat

2.2.1 Boat description

Full scale experiments were performed on a $6\,m$ flat bottom survey boat. The boat provides a nearly horizontal lower surface measuring $3.44\,m$ in length which is uninterrupted from the bow to the stern and constrained on either side by two bilge keels $1.2\,m$ apart. The boat is driven by a 115 horsepower outboard Mercury 4-stroke motor, which is capable of propelling the boat at speeds in excess of 24 knots ($12.35\,m/s$). Boat speed was manually controlled and was maintained between ±0.35 knots ($0.18\,m/s$) for all boat speeds. Bubbles are entrained naturally at the bow, by the breaking bow wave, and along the hull-to-water contact line, and travel uninterrupted to the stern.

Numerical simulations show that the flow under the flat plate between the bilge keels of the boat is essentially straight from bow to stern, with cross flow only observed on the outer region of the bilge keels.

shows estimates (based on single-phase CFD computations) of the boundary layer thickness, δ, and the location of the distance to the wall where the logarithmic velocity profile ends at $y^+ = 800$ approximately, Δ. At this distance the velocity gradient becomes weaker and depends more on the external pressure gradient. Thus Δ is an estimation of the thickness of the high velocity gradient region near the wall, which

shows varies from $3\,mm$ at 18 knots to $6.5\,mm$ at 7.5 knots, see also Fig. 7.

Table 1: Estimated boundary layer thickness and end location of the logarithmic velocity profile

Boat Speed [knots] (m/s)	**Δ [mm]**	**Distance to $y^+ = 800$ Δ [mm]**	***Fr***
2.5 (1.29)	78	12.0	0.17
5 (2.57)	72	8.7	0.33
7.5 (3.86)	67	6.5	0.5
10 (5.14)	63	5.0	0.67
12 (6.17)	61	4.2	0.8
14 (7.20)	59	3.7	0.94
16 (8.23)	57	3.3	1.07
18 (9.26)	56	3.0	1.21

2.2.2 Positioning

Measurements were taken at two locations below the hull, at the bow and at the stern, see Fig. 16. At the bow, measurements were taken $316\ cm$ fore of the end of the flat plate section and $112.1\ cm$ to port of the starboard bilge keel. This location, herein called ‘the bow’, was selected as close to the leading edge of the flat plate section as physical limitations allowed, and chosen to provide the initial two phase flow quantities from the bow entrainment. The stern measurement point was located $2.75\ cm$ fore of the end of the flat plate section and $18.3\ cm$ to port of the starboard bilge keel, and is herein called ‘the stern’. This location represents the final two-phase flow quantities exiting the stern of the boat, after the bubbles have traveled the approximate $3.1\ m$ of flat plate between measurement locations and allowing maximum interaction between the bubbles and the boundary layer. Positioning the probes on opposite sides of the boat was necessary to avoid interference of the bow probe with the stern measurement point.

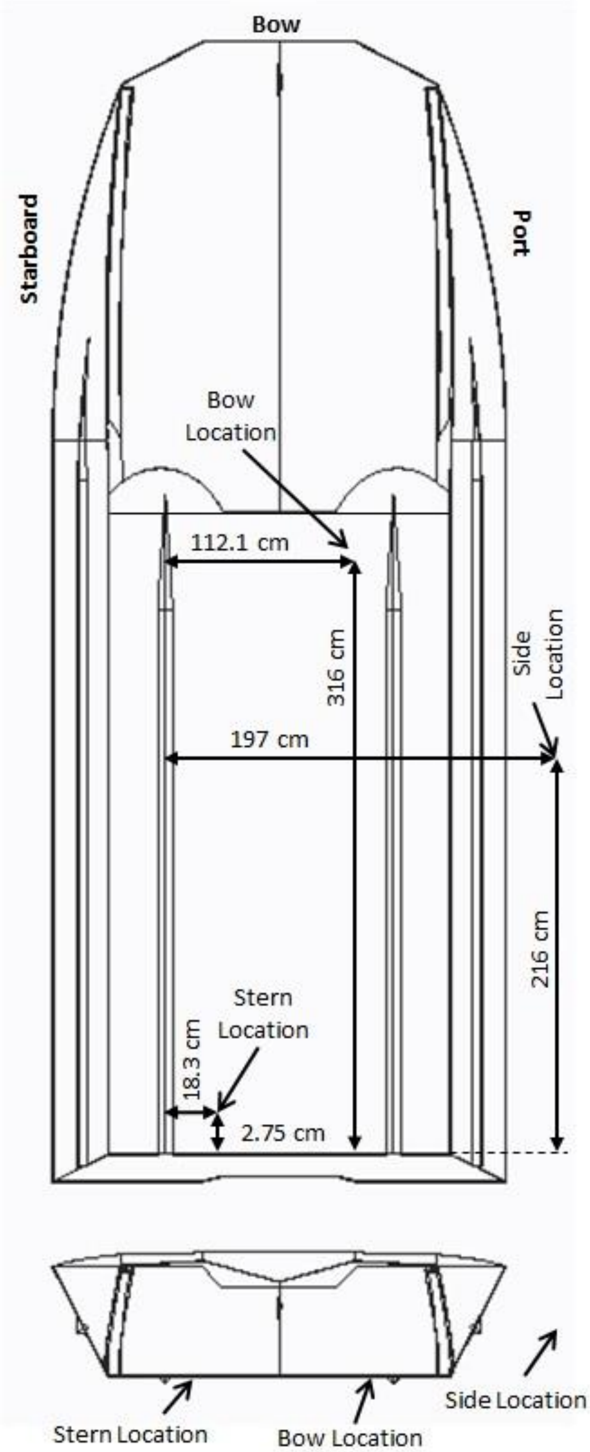

Figure 16: Probe locations, viewed from the bottom (top) and the bow (bottom) of the Kann boat

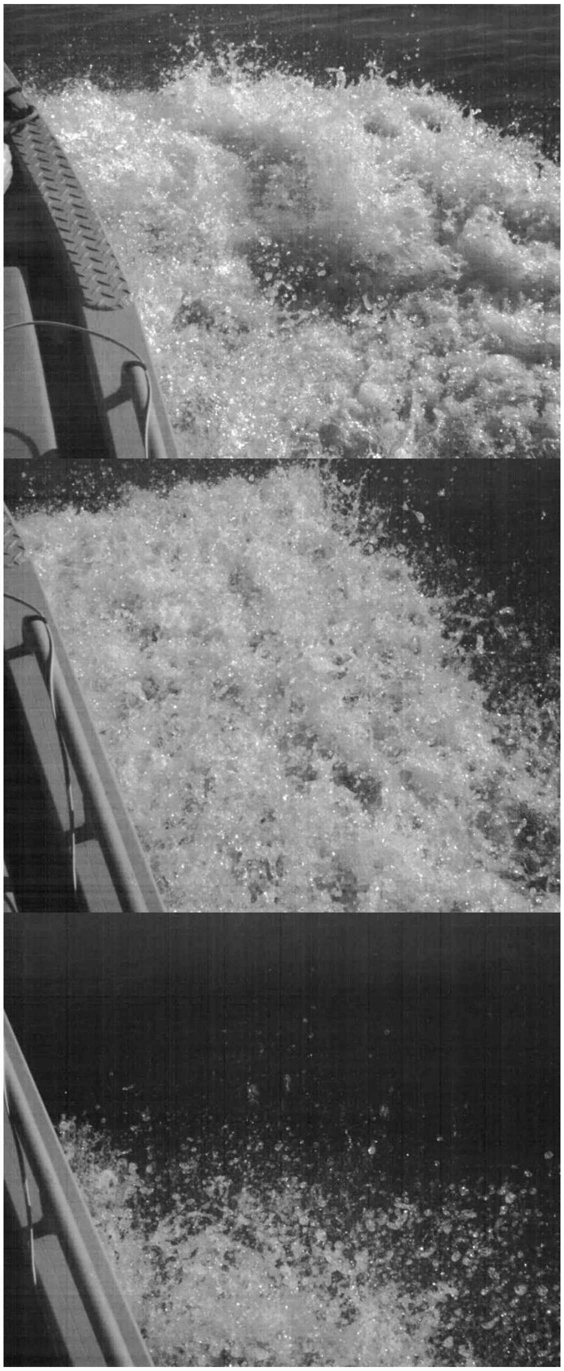

Figure 17: Bow breaking wave at 10 knots (top), 14 knots (middle) and 18 knots (bottom)

Measurements were also taken along the side of the boat at a location 3.78 m aft of the bow and 149 mm to port of the port side of the boat (Fig. 16). This location was selected aft of the bow breaking wave (Fig. 17) and was chosen with the intention of capturing the entrainment due to the bow breaking wave with no interaction with the boat.

Since the goal was to measure in the very thin boundary layer, the probes had to reach very close to the hull of the boat (Fig. 18). Each of the probes was positioned with a stepper motor driving a 100:1 gearbox attached to 2:1 right angle bevel gear boxes to precisely control the distance of the probe tip from the hull of the boat (Fig. 19). The positioning mechanisms was to be able to repeatedly position the probes throughout the measurement domain of 0 to 50.8 mm below the hull in the stern and 0 to 25.4 mm (in fresh water) and 38.1 mm (in salt water) below the hull in the bow over a number of days with sufficient positional accuracy to properly discretize the developing boundary layer. Positional accuracy of $\pm 0.1mm$ was achieved throughout the measurement campaigns. The side probe was attached to a linear traverse controlled by a stepper motor with a positional accuracy of $\pm$ 0.5 mm. For the side, the

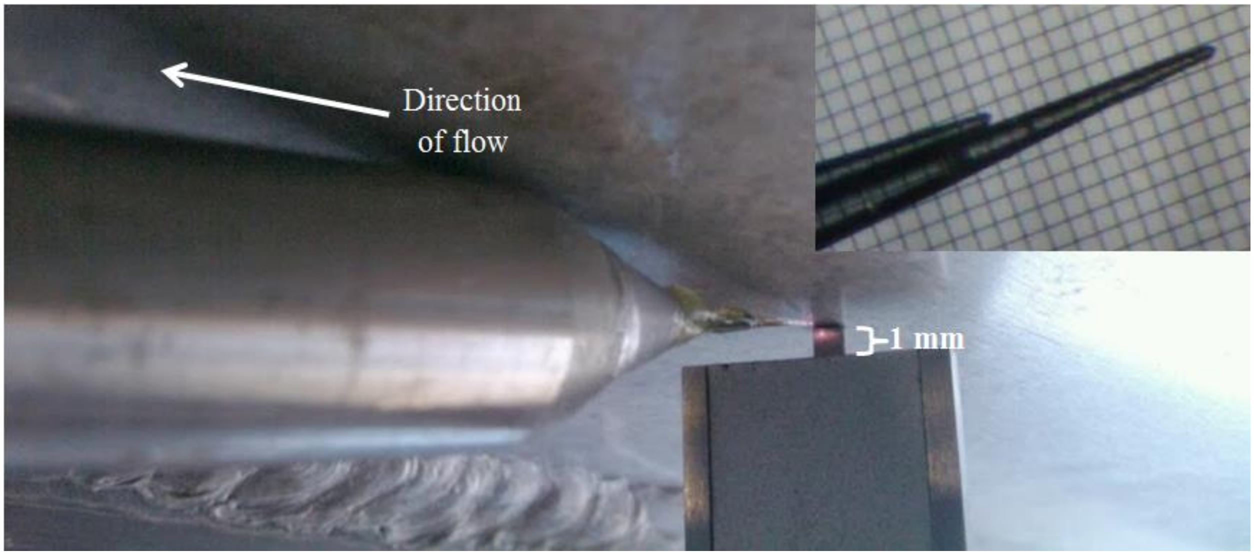

Figure 18: Detail of the bow probe against the bottom of the boat compared to a 1 mm opening in a caliper. The detail of the tip is compared to a 50μm grid

measurements were taken from the free surface of the water relative to the boat at rest downwards.

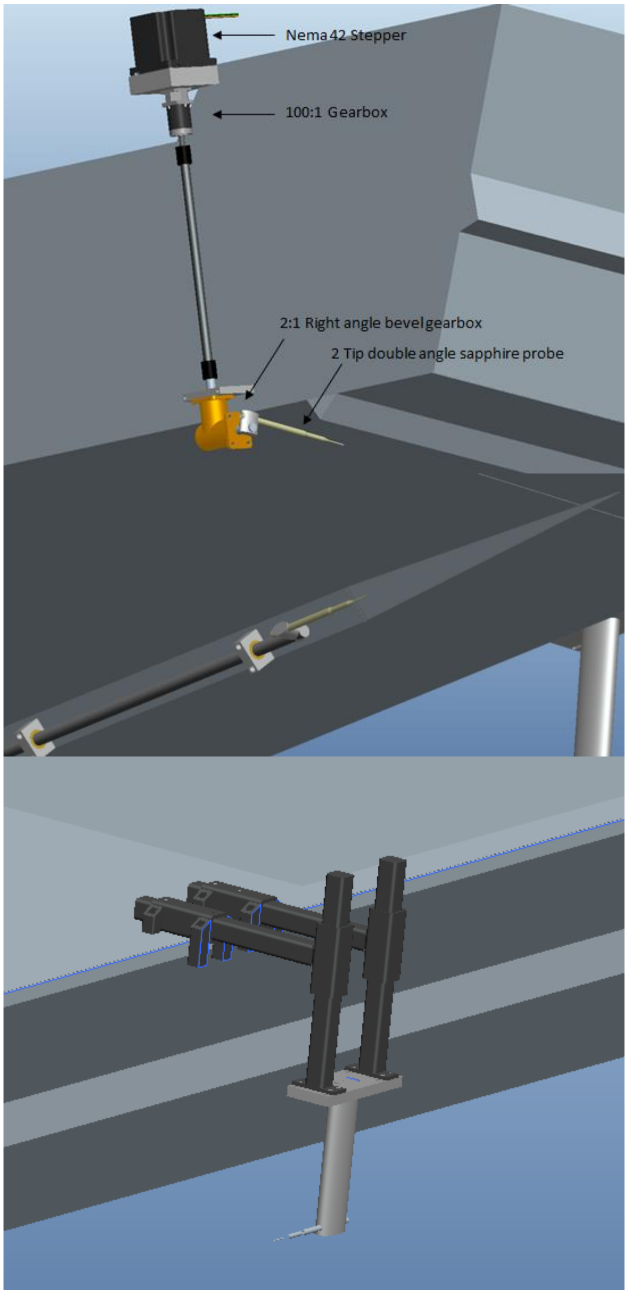

Figure 19: Schematic of positioning systems at the stern (top), bow (middle) and side (bottom)

2.3 Kann boat measurements

2.3.1 Experimental conditions

Fresh water measurements campaigns were conducted on the Coralville Lake in Johnson County, Iowa, between the Mehaffey Bridge and the Sugar Bottom Campgrounds, where the dammed Iowa River has a straight section sufficiently long enough to allow for 3-6 minute runs depending on speed. The three days of 2012, July 19th, 31st and September 28th, were selected for data collection based on the calmest forecasted weather conditions allowing measurements to be taken from sunrise to late afternoon.

The salt water measurements campaigns were conducted in the St. Andrews Bay and along the Panama City Beach in Panama City, Florida. The measurements were taken during the week of May 22nd through the 26th. In an attempt to maintain consistency with the fresh water measurements, the experimental locations each day were selected to be in the lee shore whenever geographically possible. Environmental issues related to varying sea states, wave heights and wind speeds are addressed in §2.3.2.

Measurement runs were taken for boat speeds of U_0 = 5.14, 7.2 and 9.26 m/s (10, 14 and 18 knots) in dynamic or static mode. In dynamic mode, the probes were moved at a slow rate, varying from 1 mm/min to 10 mm/min through the measurement domain with the intention of getting finely discretized spatial distributions of void fraction, chord length and bubble velocity. In static mode, the probes were maintained at a given location for the duration of the measurement run. The objective of the static mode measurements is to collect sufficient statistics at each location to compile bubble chord and size distributions. Repeat runs of the same measurements were ensemble averaged ensuring convergence of all values.

Being a small boat, the static trim changed by redistributing the weight. The trim affects the behavior of the boat, mainly at lower speeds, by changing the boat attitude. Higher pitch angles result in higher resistance and bubbles entrained further downstream. At higher speeds, beyond 6 knots, the weight distribution is less important since the boat takes a bow-down attitude. The static trim of the boat was set by the distribution of the weight of the electronics onboard to maintain nearly zero pitch and roll angles. Dynamic averaged measurements of pitch and roll were measured and are summarized in Table 2. The same distribution of weight on the boat was maintained throughout all of the measurement days.

Table 2: Boat static and dynamic trim

Boat Speed [Knots] (m/s)	**Pitch [Degrees]**	**Roll [Degrees]**
0 (0)	0.4	.3
7.5 (3.86)	-2.7	1.0
9.8 (5.04)	-4.2	1.9
13.4 (6.89)	-3.7	2.0
15.3 (7.87)	-3.6	1.7
15.7 (8.08)	-3.4	1.6
17.6 (9.05)	-2.8	1.5
20.5 (10.55)	-2.0	2.0

2.3.2 Environmental impacts

As noted in Johansen *et al.* (2010) there is an influence from the relative direction of the boat to the waves on void fraction and other two-phase quantities. When traveling into the oncoming waves the void fraction increases in comparison to traveling with the direction of the waves. Similar environmental influences are seen with the Kann boat. The Kann boat, having a shallow draft and flat profile, is very susceptible to subtle changes in the sea and wind state.

In the simplest description, waves are characterized by the wave spectrum, amplitude and direction relative to the boat advance direction. Wave interaction with wind produces additional non-linear effects like wave spilling and breaking. In this work waves were not directly measured, due to complexity and changing conditions. However, environmental effects proved to be very important and should be characterized as well as possible in future full-scale measurement attempts.

Figure 20 shows the influence of wind speed on void fraction and average chord length at the stern of the boat 5 mm away from the hull and at a boat speed of 14 knots in fresh water. The wind speed has the effect of roughening the surface of the water, in addition to increasing the size of the waves. On the Coralville Lake, where there are approximately 1.5 miles of fetch, the development of waves is somewhat hindered, but there is wind induced chop which creates small amplitude waves with short wave lengths. This is similar to St. Andrews bay in Panama City, FL, where there are approximately 4 miles of fetch. In both cases, Coralville Lake and St. Andrews bay, the void fraction and chord length show strong correlation with increasing wind speed. The roughness of the water and the wind induced chop serve to increase the bubble entrainment as

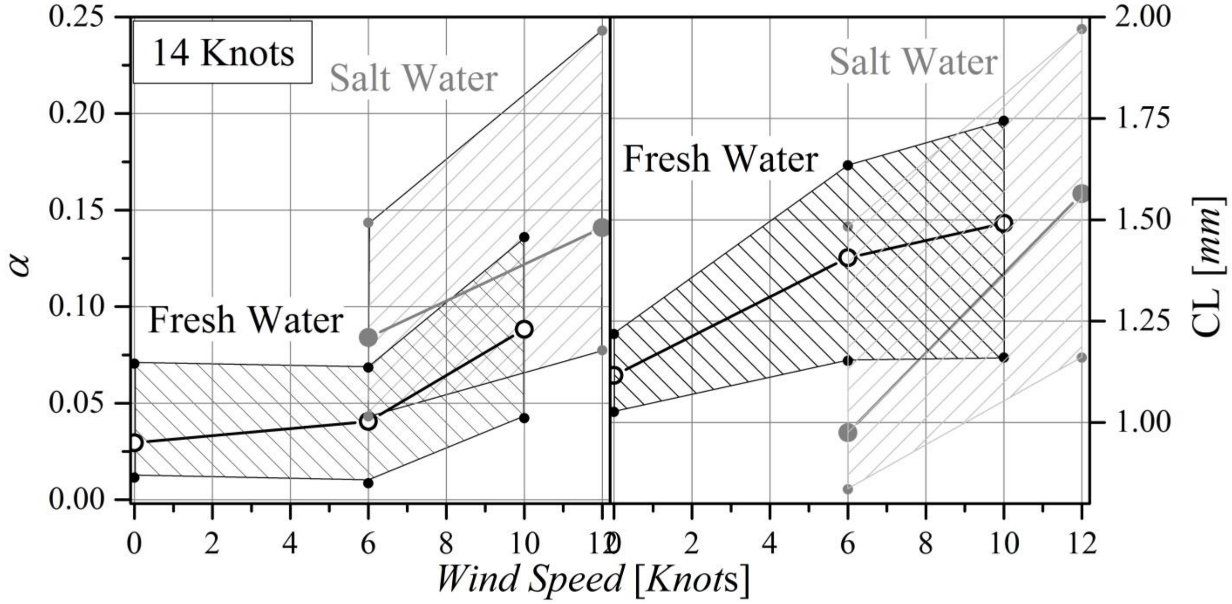

Figure 20: Void fraction and chord length as a function of wind speed 5 mm away from the hull in the stern at 14 knots

the bow of the boat hits the waves, trapping pockets of air and bubbles against the flat hull where they are subsequently pulled underneath the boat. The bands of measurement extremes between the trials taken at that wind speed show the extent to which the averaged measurements vary within those specific conditions.

The void fraction is seen to increase approximately 30% in salt water and 100% in fresh water with an increase in wind speed from a light breeze of 4 to 6 knots to a moderate wind of 10 to 12 knots. With no wind, in fresh water, the void fraction asymptotically approaches a minimum of 0.03%. This largely has to do with the water being essentially smooth, with the only mechanisms for air entrainment being at the hull to water contact line and the breaking waves created by the boat. The change in void fraction in salt water tends to be greater than in fresh water from the additional fetch the wind has to build waves and surface roughness. Similar trends are seen in the average chord length, where the increasing wind speed has the effect of entraining larger bubbles. The processes that occur to breakup the bubbles, discussed in §0, start from larger bubbles and thus results in bubbles tending towards larger sizes.

Similarly to the effects seen by the wind, waves affect the multiphase quantities, primarily by the relative direction that the waves are encountered and the types of waves encountered. Two types of waves were seen. Within St. Andrews bay and on Coralville Lake, the waves are wind induced chop as discussed above. Outside the bay, along Panama City Beach, there is the addition of swell. The swell tends towards longer wave-length waves with typically higher wave heights than the wind chop found inside the bay. The longer wave length acts to rock the boat side to side, as the wavelengths were much greater than the beam of the Kann boat. Traveling parallel to the beach results in broadside waves approaching the boat. A note should be made that running parallel to the beach within two hundred meters yielded nearly no wind chop. The proximity to the beach does not allow sufficient distance for the chop to build, but does allow, to an extent, ripples and surface roughness to be generated. Additionally, the tall buildings and structures built along the beach serve to block the wind in certain areas, and conversely accelerate the wind speed in other areas.

Due to excessive weather conditions for the Kann boat, only two days' worth of measurements were conducted outside of the St. Andrews bay and along the beach. The second day saw an overnight decrease in the swell, and as can be seen in Fig. 21, the net effect is a reduction in average chord length and to a lesser extent a reduction in void fraction. This implies that, unlike inside the bay, the increasing swell minimally affects the void fraction, but the bubbles entrained are of larger size, meaning that significantly fewer bubbles are entrained to correspond with the nearly 20% decrease in chord length. A similar conclusion can be made by evaluating what occurs as the boat crosses another boats' wake. The wake can be crossed in one of two primary directions: longitudinally or transversely. Crossing another boats' wake transversely, relatively perpendicular to the other boats direction of travel, is in effect similar to encountering wind driven chop. The boat experiences short waves closely spaced together. When a wake is crossed in a parallel fashion, which occurs either when being overtaken or overtaking

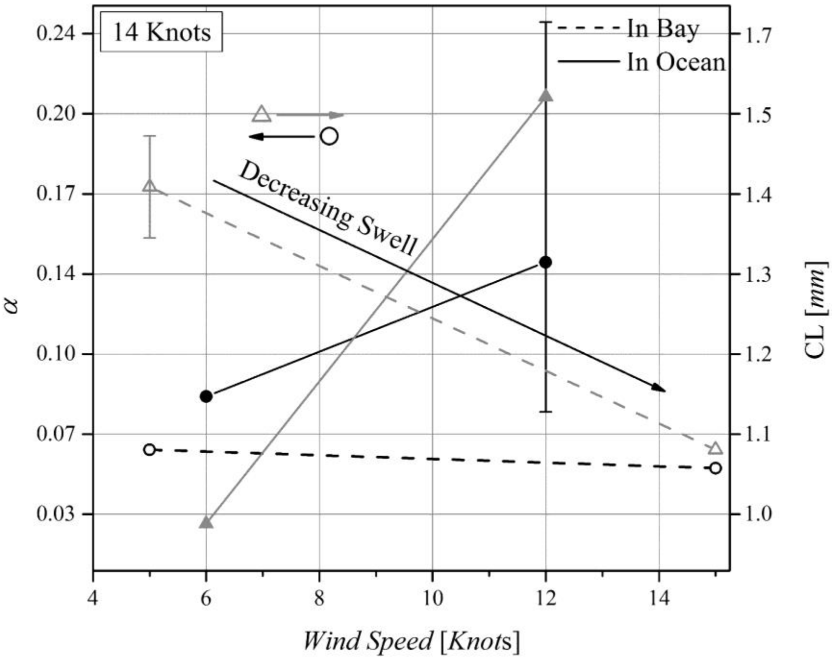

Figure 21: Void fraction and chord length as a function of wind speed 5 mm away from the hull at the stern at 14 knots, in salt water

another boat, the wake acts to rock the boat from side to side, similar to the swell experienced outside of the bay, parallel to the beach. Figure 22 shows time evolution of void fraction, chord length and bubble velocity integrated over 2 s. Data was taken at 18 knots on the Coralville Lake where the boat traffic is more constrained and in closer proximity. Figure 22 shows that longitudinally and transversally crossing a boat wake yield spikes in void fraction relative to the average void fraction. The average chord length also tends to increase, while the bubble velocity appears unaffected. The occurrence of a strong wind gust appears to reduce void fraction, chord length and bubble velocity by momentarily "flattening" the water surface.

In view of the preceding discussion, all subsequent measurements are presented as if they were taken on one continuous measurement, ensemble averaging all takes for each probe location and boat speed. This gives a representative average and a basis for comparisons among measurement locations and speeds, but adds significant data spread since the sea state, not properly measured, is removed as controlled variable defining the experimental condition. Key to

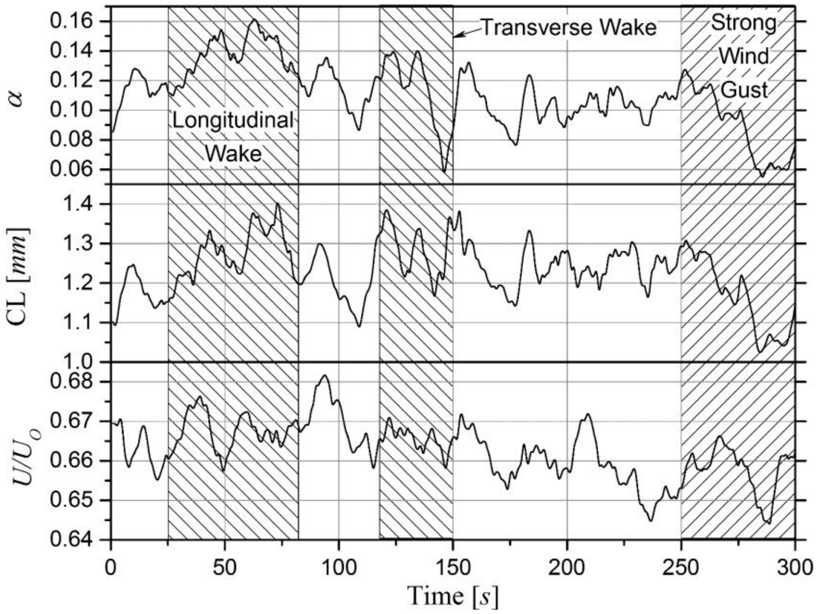

Figure 22: Time history of void fraction, chord length and bubble velocity 5 mm away from the hull in the bow crossing boat wakes

this point is that some measurements, taken purely for comparative purposes, may not correlate with measurements taken to represent average values, as the day they were taken on only represents that specific sea and wind state and not an average value. These measurements are discussed and are used for a general qualitative understanding of the bubble entrainment and transport processes and how they are influenced by one specific variable. Proper discrimination of environmental effects on the two-phase parameters requires high-quality measurements to characterize the free surface roughness, which in turn requires a very significant effort due to the amount of data required under different environmental conditions. Such a study has not been done in this work.

2.3.3 Runs at a range of speeds

Measurements to evaluate the bubbly flow parameters at the stern were taken at a range of boat speeds with the stern probe $5\,mm$ away from the wall in fresh water and at several distances to the hull in salt water. These measurements were taken on a calm day on the Coralville Reservoir and parallel to Panama City Beach. Results are reported in Fig. 23. The Froude number, $= U_0/\sqrt{Lg}$, is reported in

. The transom stern becomes dry at approximately $Fr = 0.5$. This number is slightly higher than those observed for larger ships; in Athena R/V, for instance, transition from wet to dry transom occurs approximately at $Fr = 0.35$ (Wilson *et al*., 2006). The higher Froude number needed for dry transom can be explained by the large draft-to-length ratio of the boat compared to most large ships. During the transition from a wet to dry transom a number of aspects of the flow change. Except for this section, discussion in this paper is centered in the dry transom condition, for speeds of 10 knots and higher, guaranteeing that bubbles reaching the transom have undergone similar flow conditions.

The void fraction at $5\,mm$ shows an initial peak of 2.5% around 5 knots in fresh water and a spike of 13% in salt water (likely due to fairly choppy conditions during the salt water measurements), then goes to very low values and at 10 knots grows quickly peaking again at approximately 8% for 18 knots to 20 knots in both salt and fresh water. Interestingly, beyond 18~20 knots the void fraction starts to decrease again as does the impact rate, but the average chord length remains approximately constant. The impact rate of bubbles with the probe grows steadily with boat speed beyond 10 knots, reaching approximately $300 - 400\ \text{bubbles}/s$ at a speed of 21 knots. In fresh water the average bubble chord length peaks at approximately $2.5\ mm$ at the same speed of 5 knots where the void fraction shows a peak. This speed corresponds as well to a local peak in the bubble impact rate, and indicates that higher void

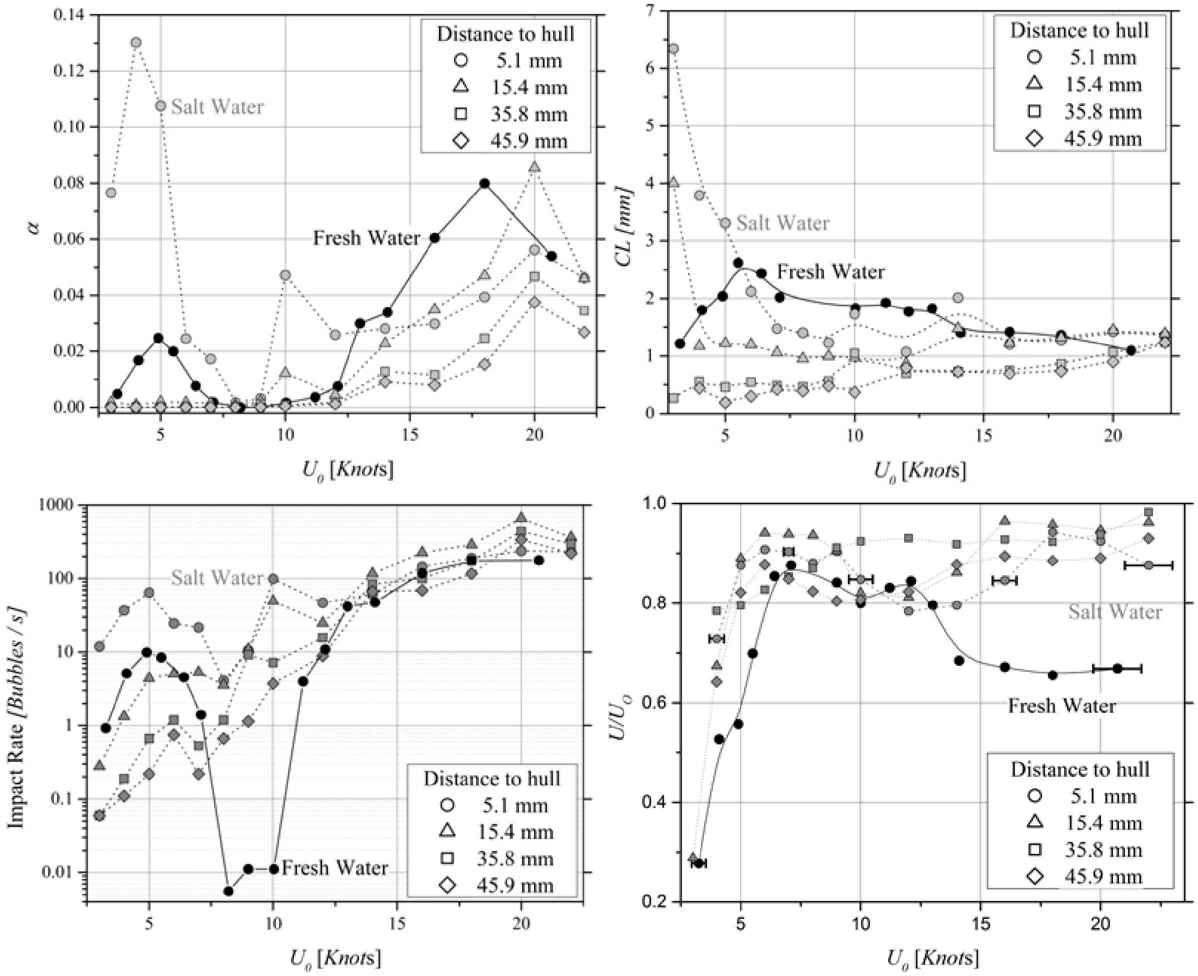

Figure 23: Void fraction (top left), chord length (top right), bubble impact rate (bottom left) and bubble velocity (bottom right) at the stern as a function of boat speed

fraction at low velocity promotes significant coalescence. In salt water, where large void fraction is observed at very low speed the peak bubble size reaches $6.5\,mm$ at $5\,mm$, at a speed of 3 knots, the lowest measured. This confirms the observation in fresh water, that at low speeds and high void fraction bubbles accumulate at the bottom of the hull and coalesce. Further indication of this is the strong decrease in void fraction and average chord length observed at low speeds as the distance to the hull increases (since the bubbles rise and accumulate at the hull), and as the velocity increases (since more turbulence breaks and disperses the bubbles). At low speeds only the smallest bubbles can be found further away from the hull. At the same time Fig. 23 shows that the bubble velocity is a fraction of the boat speed for boat speeds below 5 knots, indicating that the probe is well within the boundary layer at these low speeds. At higher boat speeds the bubbles quickly start moving with velocities above 80% of the boat speed, though in salt water a decrease is observed beyond 13 knots. The point where the bubble velocity with respect to the boat velocity stops increasing occurs for boat speeds between 5 and 7 knots, coincident with the speeds where at $5\,mm$ away from the hull the void fraction and impact rate decrease to a minimum, and as the chord length also decreases.

At $5\,mm$ from the wall the impact rate and void fraction show a low at approximately 7 knots, with the effect more remarkable in fresh water. At this speed the transom becomes dry and the boat trims bow down, essentially entraining less air bubbles. In fresh water this effect is stronger since the water was calmer when the experiments were performed than in the case of the salt water experiments, resulting in less bubbles and thus lower impact rate. As the speed increases air entrainment quickly picks up in both fresh and salt water.

It is speculated that at low boat velocities large pockets of air are entrained at the bow tend to get trapped under the hull. These pockets are then transported down the hull and break up into smaller, yet still comparatively large, pockets and bubbles. The expectation is that these will remain in the form of a bubble that tumbles along the hull, where buoyancy acts pushing them up, but the hull constrains them down. As the boat speed increases, and with it the shear rate, Fig. 23 shows that the average bubble chord length at $5\,mm$ decreases with increasing boat speed, supporting the view that bubble breakup becomes the dominant effect to determine bubble size distributions in high-shear flows. On the other hand, farther out from the hull the average chord length increases with increasing boat speed, indicating that as turbulence increases the gravitational filter (larger bubbles rise faster and leave only small ones behind) is overcome by mixing and consequently larger bubbles are also found at higher depth.

2.3.4 Bubble velocity

Bubble velocities are reported in the boat frame of reference in Fig. 24, with the bubbles seen moving relative to the probe. A positive velocity is thus a bubble moving from the bow of the boat to the stern. In both fresh and salt water at all boat speeds and locations, the bubble velocity is lower than the boat speed, suggesting that the effects of the boundary layer reach further from the hull than the maximum displacement of the probes. At the bow, a shallower velocity profile is observed in both fresh and salt water. The velocity gradient is greatest within $5\,mm$ of the hull of the boat as expected by the presence of a no-slip boundary condition in the liquid phase. Note however that the bubble velocity does not reach zero, indicating that there is a slip velocity between the bubbles in contact with the hull and the wall. The slip velocity is largely attributed to the sharp velocity gradient in the region closest to the hull (see Fig. 7), where bubbles very close to the hull experience a pull on their outer surface that produces the relative velocity while also contributing to their deformation and breakup.

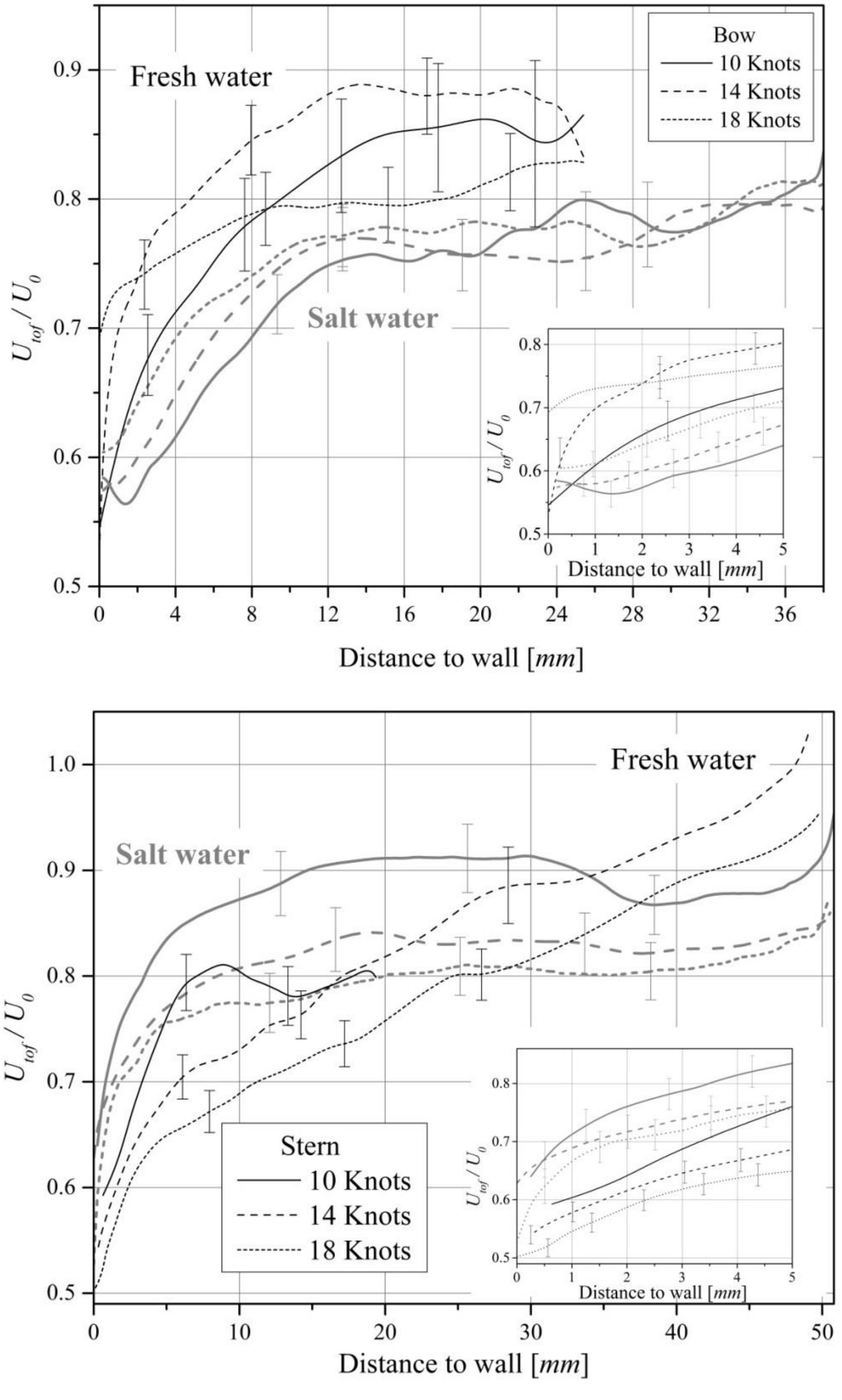

Figure 24: Bubble velocity at the bow (top) and stern (bottom)

The pull of the outer surface of the bubbles can be evaluated by a plot of the chord length to bubble velocity, Fig. 25. This figure shows the average time of flight velocity, Eq. 16, of all bubbles that fall within the corresponding chord length interval of $cl \pm dcl$. For bubbles smaller than 100 μm the optical probes become more intrusive and the velocity measurements become less reliable, as discussed in more detail in §2.3.7 that focuses on the limitations of the instrumentation. It can be seen that close to the wall, smaller bubbles move slower than larger bubbles at the same location due to them not experiencing the same pull on their outer surfaces. This trend goes away with increasing distance to the wall, at 30 mm from the wall, where the velocity gradient is significantly lower than closer to the wall, nearly all bubble sizes have the same velocity.

The extent of the bubble slip relative to the liquid phase can be seen by evaluating the local shear rate experienced by the bubbles and comparing it to the liquid shear computed by CFD. Figure 26 shows that at approximately 500 μm and closer from the wall the velocity gradient of the bubbles diverges from that of the liquid. The maximum shear rate measured from

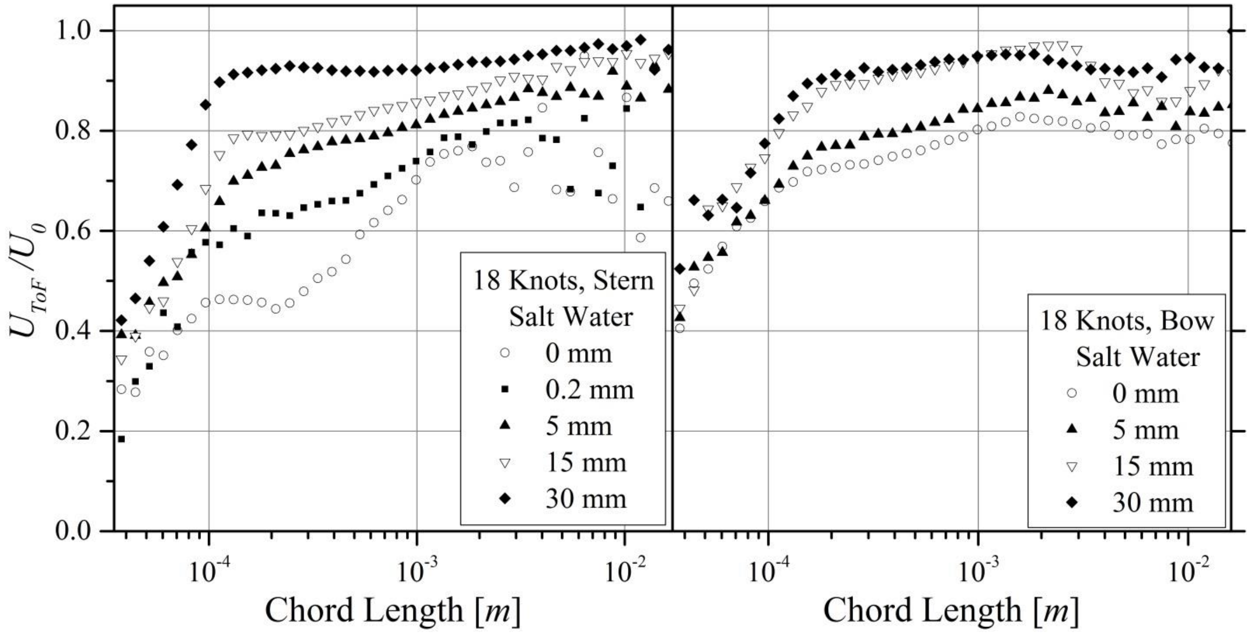

Figure 25: Bubble velocity for different chord lengths in salt water, stern and bow

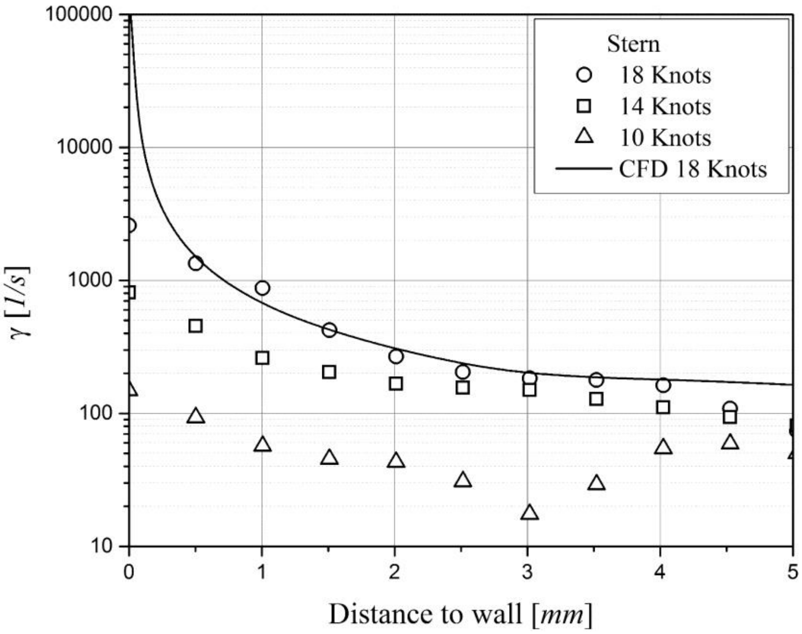

Figure 26: Shear rate for the stern in salt water

the bubbles is approximately $\gamma = 2{,}500\ 1/s$ and occurs at 18 knots right at the hull and decreases to $800\ 1/s$ and $150\ 1/s$ at 14 and 10 knots, respectively. This compares to the single-phase value predicted by CFD of about $\gamma = 100{,}000\ 1/s$ at 18 knots. The liquid velocity gradient in the two-phase flow will be higher than the bubble velocity gradient, but likely lower than the single-phase velocity gradient predicted by CFD. As discussed in §1.3.1.2, the maximum shear rate measured is not sufficient to break up the bubbles by pure shear, but contributes to their deformation.

Bubble velocities at the bow probe location are higher in fresh water than in salt water, an unexpected result showing the extent of effects of the differences in environmental conditions already discussed in §2.3.2. The breaking wave in this region of the flow is especially sensitive to pitching and rolling, quickly changing location along the hull and strength as the boat pitches. Even though absolute values are different, general trends are the same for bubble velocity in fresh and salt water experiments. In both cases the bubble velocity reaches the far-field velocity closer to the wall as the boat speed increases. At the stern the situation reverses and the far-field velocity is reached closer to the wall for lower boat speeds, as if the boundary layer was getting thicker with boat speed. It is speculated that this behavior is due to the higher void fractions and mixing present far from the wall at higher speeds, as discussed in §2.3.5.

The RMS bubble velocity fluctuations are shown in Fig. 27. At the bow the fluctuations tend to be more uniform with distance to the wall. This is because the fluctuations at the bow are mostly due to turbulence caused by the bow breaking wave, which has not yet been influenced significantly by the boat wall. At the bow the relative fluctuations decrease with boat speed, indicating that the absolute magnitude of the fluctuations varies little with boat speed. The RMS of the bubble velocity fluctuations show a more traditional wall-bounded pattern at the stern, where there is a decrease in intensity as the distance to the wall increases and the RMS for all boat speeds tend to collapse. Of particular interest is that the bubble velocity fluctuations peak at the wall instead of decreasing to zero. Though the boundary layer is too thin to measure the viscous sublayer, bubble velocities are considerably high near the wall and fluctuations are also high.

Figure 28 shows normalized bubble velocity distributions for 10 and 18 knots at bow and stern and at different distances from the hull. The bubble velocity distribution gets wider closer to the hull, as expected by the larger RMS fluctuations shown in Fig. 27. The bubble velocity shows a considerably wide range near the wall. At 10 knots at the bow, for instance, the bubble velocity can be as low as $0.2U_0$ and as high as $1.4U_0$. In general, the bubble velocity distributions for fresh and salt water show tails of low but non-zero probability of fast bubbles at all distances from the hull, though the effect is weaker in fresh water at 18 knots. These high-speed bubbles, moving faster than the boat speed, can only be present in the flow if they are carried by high-speed water reaching to the probe measurement point. A possible explanation for those bubbles moving considerably faster than the boat is that the water surface waves induce a velocity fluctuation that is superimposed with the turbulence generated by the boat itself.

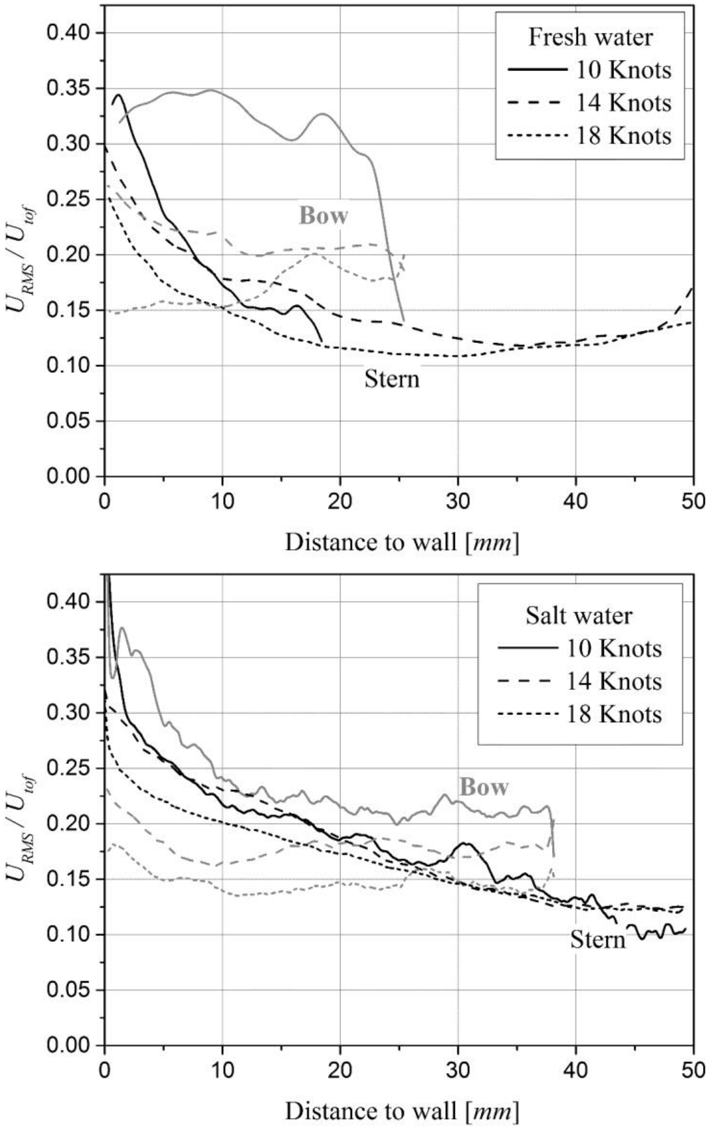

Figure 27: RMS of bubble velocity fluctuations in fresh water (top) and salt water (bottom)

2.3.5 Void fraction

Void fractions as a distance to the wall for bow and stern are presented in Fig. 29. In the bow, the void fraction peaks at distances to the wall between 2.5 and $10\ mm$, more clearly defined at 10 knots in salt water and less noticeable at 14 knots. Significant differences in bubble

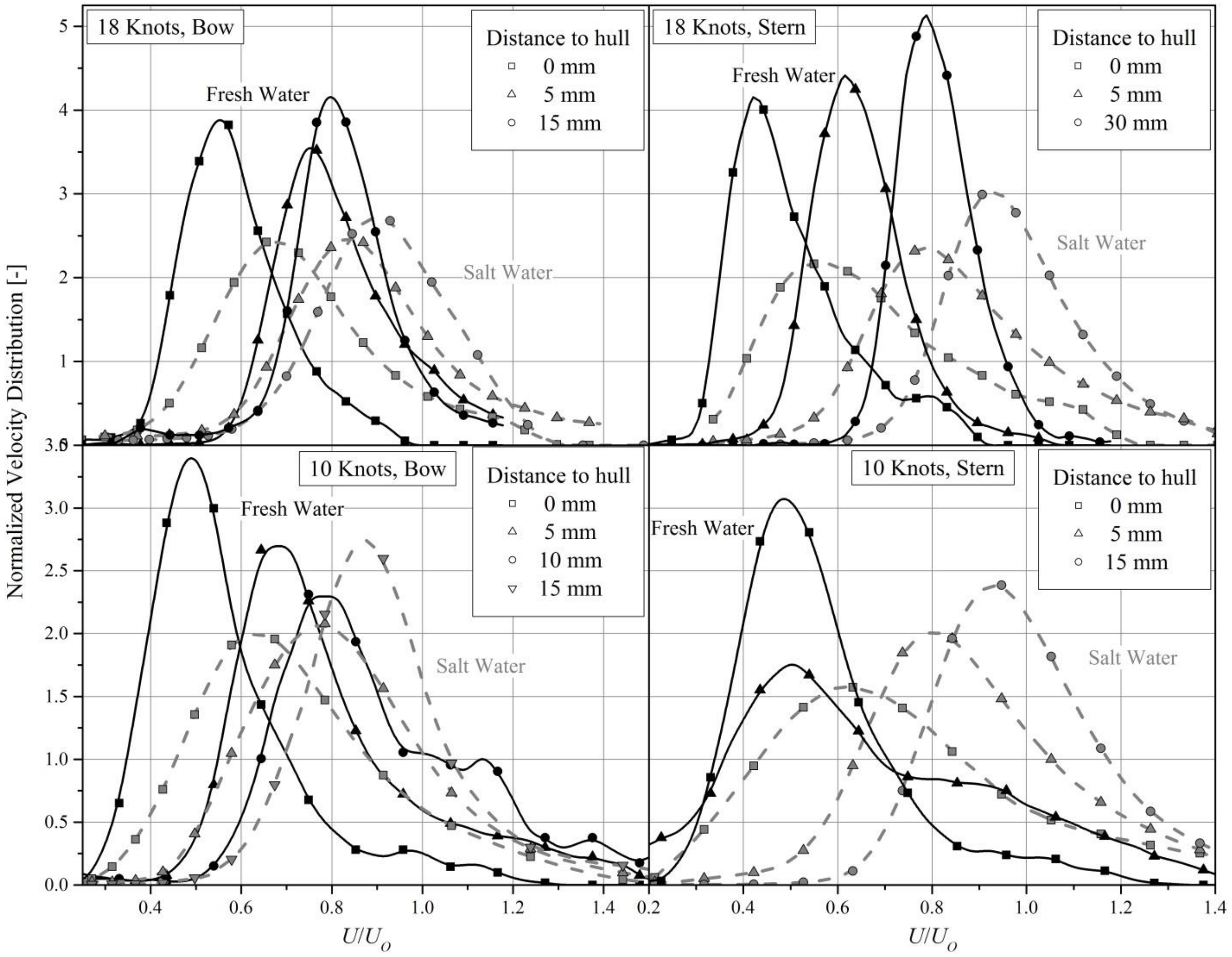

Figure 28: Bubble velocity distributions at 10 knots (bottom) and 18 knots (top) for the bow (left and stern (right) probes

entrainment (and thus void fraction at the bow) are observed between salt water and fresh water at 10 knots, with much less noticeable differences at 14 knots and 18 knots, again evidence of strong environmental effects. The much higher void fraction observed at 10 knots in salt water is believed to be caused, in particular, by the impact of the bow with the rougher water surface occurring when the experiments were performed. As the boat speed increases the entrainment caused by the boat's bow wave becomes dominant and the environmental effects become less noticeable, as shown by Fig. 29. The much more uniform void fraction with distance to the wall for the higher velocities shows that the bubbles entrained are primarily homogenously distributed throughout the water column. In the case of 10 knots, bubbles have additional time to rise from the point of entrainment to where they are measured at the bow location, thus displaying a peak near the wall, especially in salt water. This causes the highest void fraction to occur at 10 knots near the wall in salt water, while in fresh water occurs at 18 knots away from the wall since there's much less roughness-induced entrainment and the void fraction at 10 knots is much lower.

As noted by Baker and Chao (1965), the relative vertical bubble velocity in turbulent flows is similar to the rise velocity of a single bubble in quiescent liquid and can reach $250\ mm/s$ for the larger bubbles measured at 10, 14 and 18 knots. Thus, in the $0.5\ s$ it takes at 10 knots for a bubble to travel from the bow probe to the stern probe location (disregarding the relative bubble velocity, §2.3.4), bubbles have sufficient time to travel the full extent of the measurement domain. This is what leads to the accumulation of bubbles below the hull and the peaks in void fraction observed at the stern.

Despite the rise velocity of the bubbles and the buoyancy helping accumulation below the hull, there is a sharp decrease in the void fraction between 0 and $2\ mm$ in the stern. This partly can be attributed to the shape and size of the bubbles. Bubbles close to the hull are constrained by the non-penetration condition near the solid wall, and turbulence can only push them away from it, creating an anisotropy that favors accumulation near the wall but not at the wall. Surface tension also helps maintain a spherical shape and keep the longest chord lengths at least one radius away from the wall, assuming bubbles can maintain spherical shape in the high-shear wall region, see discussion in §1.3.1.2 and §2.3.4.

In general, for all speeds the void fraction measured in salt water is higher than that for fresh water. This is likely due to the rougher free surface conditions observed in the sea trials. In all other aspects trends are the same for fresh and salt water. The results for void fraction at the stern for 18 knots are similar for salt and fresh water, with a plateau of 11% reached at $10\ mm$ and maintained through $2\ mm$. At 14 knots there are peaks in void fraction at different locations for fresh and salt water. In salt water the void fraction reaches 15.5% $2\ mm$ away from the wall, whereas in fresh water the peak is observed at $7\ mm$ and only reaches 9%. In fresh water, at 10 knots, the void fraction sees a steady increase to a maximum of 1.8% at approximately

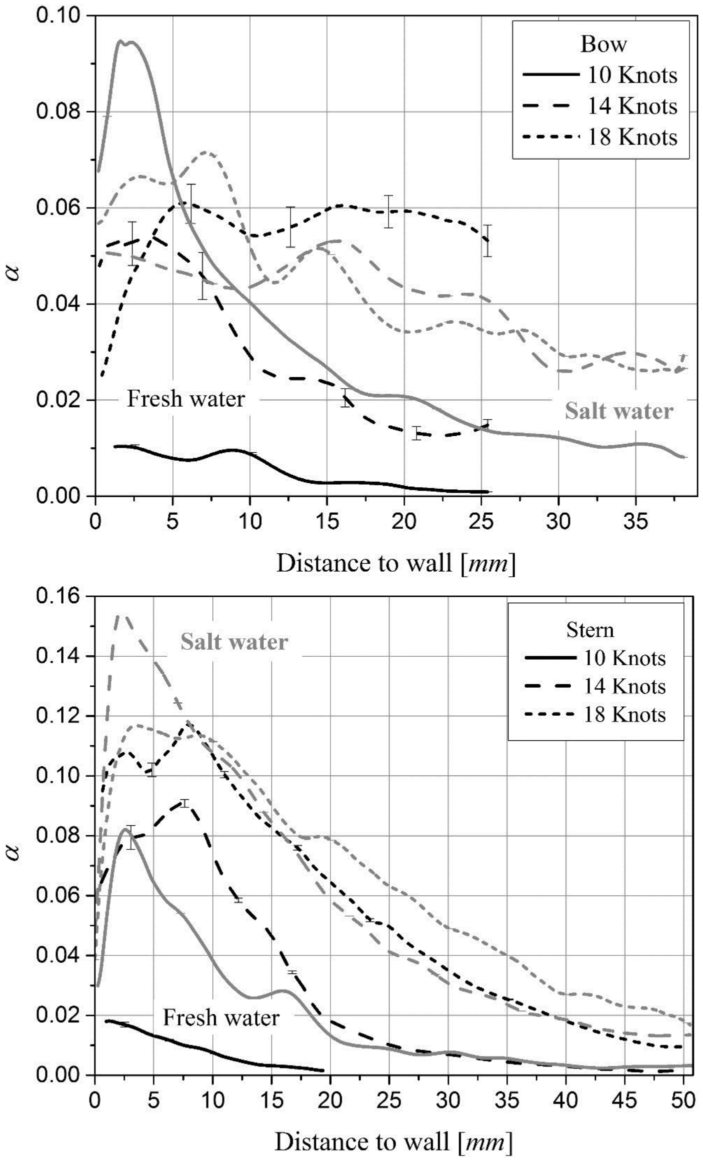

Figure 29: Void fraction as a function of distance to the hull for bow (top) and stern (bottom)

$0.635\ mm$. Closer to the hull, no bubbles were encountered. In salt, at 10 knots the void fraction corresponds closely to that of 14 knots in fresh water with a peak of 8.2% and similar to the other speeds in salt water experiences a sharp decrease in the $0 - 2\ mm$ range.

It is interesting to note that under no condition of speed or sea roughness does the void fraction exceeds 16% (see Fig. 23), with typical values around 6~7% at high speed. This is much smaller than the unfiltered values reported by Johansen *et al*. (2010) in the bow, masker and transom of Athena RV using optical probes, and also by Terrill *et al*. (2005) in the transom using conductivity probes. The unfiltered signal shows raw values of void fraction including times when the air is the continuous phase and drops are the dispersed phase. Occurrences of the free surface moving up and down happen more frequently in the masker and transom regions, resulting in higher absolute void fraction. Johansen *et al*. (2010) filter these out-of-water events by removing signals where the duration of air greatly exceeds the duration of water, indicating that the water is the dispersed phase. The resulting void fraction is comparable with the void fraction shown in this work and accounts only for the void fraction due to bubbles in water.

2.3.6 Chord length and bubble size

Figure 30 shows the average chord length as defined by Eq. 18. In general, larger average chord lengths are observed in fresh water than in salt water, as expected from the lower coalescence rates occurring in salt water (Craig *et al*., 1993; Tsang *et al*., 2004; Castro and Carrica, 2013a). In breaking waves, Cartmill and Su (1993) observed smaller bubbles in salt water than in fresh water.

At the bow, away from the hull, the salt water chord lengths tend to converge towards 1 mm bubbles for distances to the hull beyond 15 mm at all boat speeds. At the hull, the average chord length for 10 knots is nearly twice that of 18 knots, with 14 falling between the two. The peak cord length seen in salt water is *1.5 mm*, and occurs at 10 knots at approximately *2 mm* from the hull. The fresh water chord lengths do not show similar trends. At all speeds, the average chord lengths are larger away from the hull than near. For the higher velocities, this is expected and is similar to what is observed in salt water. Closer to the hull, at higher velocities, bubbles will have a tendency to breakup due to the elongation from shear coupled with the decreasing surface tension holding the large bubbles together and the higher turbulent fluctuations. At 10 knots though, accumulation and coalescence should play a larger role and tend towards having larger bubbles at the hull than at 14 and 18 knots. While this is the case in salt water, in fresh water, the average chord length is seen to peak at 14 knots, 6 mm from the

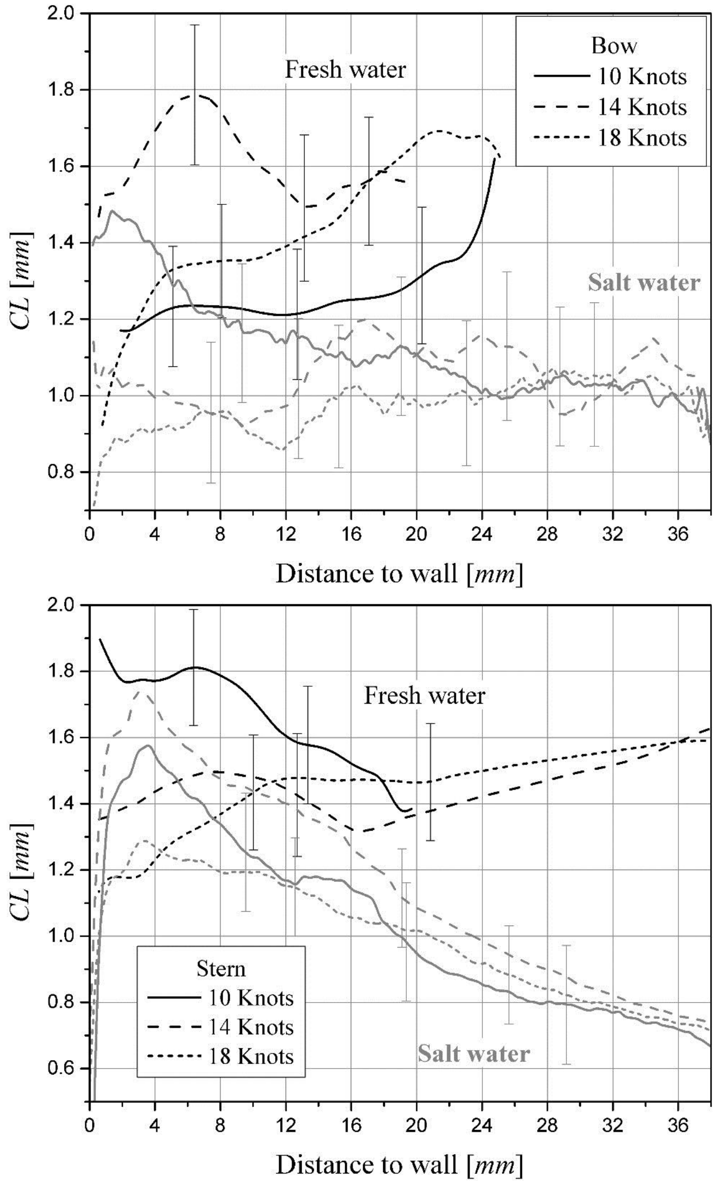

Figure 30: Average chord length as a function of distance to the hull for bow (top) and stern (bottom)

hull and maintain a higher value up to the hull. 18 knots attains the smallest chord length of 0.9 mm at the hull, with 10 knots falling in-between the two.

In the stern, more defined trends are observed. Salt water measurements show a clear trend for all boat speeds of increasing chord length moving away from the hull, peaking at approximately 3mm from the hull and then continuing to decrease throughout the rest of the distance below the hull. The fresh water 14 and 18 knots show a somewhat similar trend with the minimum chord seen at the hull and then a local peak at *8-12 mm* before a slight decrease in chord length followed by a continuing shallow increase moving away from the hull. At 10 knots, the minimum chord length of *1.4 mm* is seen away from the hull, with the chord length increasing all the way to the hull and reaching a peak value of *1.9 mm*. Effectively, from the bow to the stern, buoyancy driven stratification is occurring in salt water. Smaller bubbles have a decreased rise velocity, and hence linger at depths longer and are consequently measured there. The larger bubbles float up to the hull, where they are either measured or break up into smaller bubbles.

In fresh water, bubble coalescence is evident at 10 knots, where at the bow the average bubble chord length was at a maximum away from the hull and reached a value of *1.6 mm*. The peak size reached at the stern is *1.9 mm*. Given the extra rise time at the lower boat velocity, the probability of contact between two or more bubbles favoring coalescence is increased, namely right below the hull, where the hull acts to restrict the third dimension of motion of the bubbles further increasing the likelihood of collision and contact time, resulting in stronger coalescence.

The quick drop in average chord length for salt water experiments close to the wall, and the absence of it in fresh water, is evidence that coalescence appears inhibited in salt water. Moreover, the much smaller average chord lengths than farther away from the wall seem to indicate that strong bubble breakup is also occurring in salt water.

Using the methodology described in §2.1.6 bubble size distributions can be computed from the chord length distributions obtained using Eq. 17. Normalized chord length distributions at 18 knots at different distances away from the hull in fresh and salt water are shown in Figure 31. These were obtained from steady measurements at fixed locations for several minutes, recording from about 2,000 bubbles at the lowest void fraction points to 120,000 bubbles at the densest points. The chord length distribution at 37.5 *mm* in fresh water at the stern does not have enough statistics to perform a bubble size distribution analysis and thus was not used.

An inspection to Fig. 31 shows that both at the bow and stern the chord lengths are smaller right at the wall. At the stern and at the wall the chord length distributions show a considerable increase in probability of finding chord lengths smaller than 250 μm. These trends are the same in fresh and salt water. The bubble size distributions $f(d)$ normalized with void fraction, shown in Fig. 32, are fairly similar at all distances from the hull at the bow in salt water, but in fresh water bubbles are considerably smaller very close to the hull. At the stern is clear the concentration of smaller bubbles at the wall, though the probes cannot resolve the peak around 30 µm measured on Athena R/V by Terrill *et al*. (2005) with a photographic method.

Examining Fig. 32 several important conclusions can be drawn: 1) at the bow very small bubbles are already present, more so in salt water, indicating that the entrainment process already produces very small bubbles; 2) the number of bubbles at the wall smaller than $250\ \mu m$ in diameter increases significantly from bow to stern in both fresh and salt water; 3) at the wall, the number of bubbles larger than $1\ mm$ decreases considerably; 4) the largest bubbles present occur

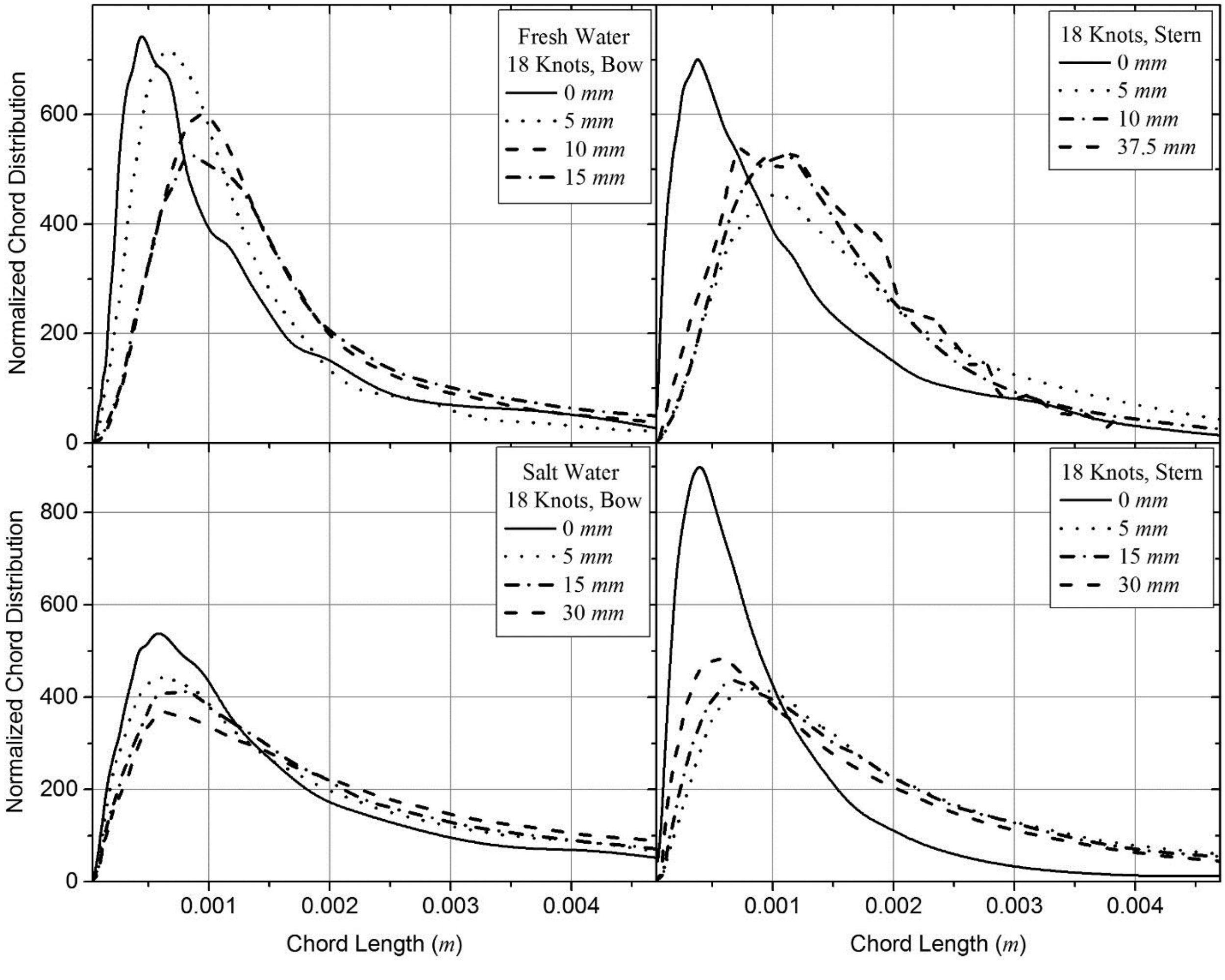

Figure 31: Normalized chord length distributions at 18 knots at different distances away from the hull, fresh and salt water

between the wall and 5 mm in fresh water, while they occur between 5 mm and 10 mm in salt water, with a sharp decrease of $f(d)$ for diameters beyond 3 mm. This would indicate inhibition of coalescence in salt water as discussed in §2.2; 5) size distributions away from the wall show more larger bubbles and less small bubbles, with the exception of the distribution 30 mm away from the wall in salt water, where gravitational filtering appears to result in large amounts of small bubbles.

Figure 33 shows the normalized void fraction distribution at 18 knots in salt and fresh water. The normalization to unit area and the use of the void fraction, which gives more weight to larger bubbles, help visualize how the size distributions shift at different positions. At the wall at the

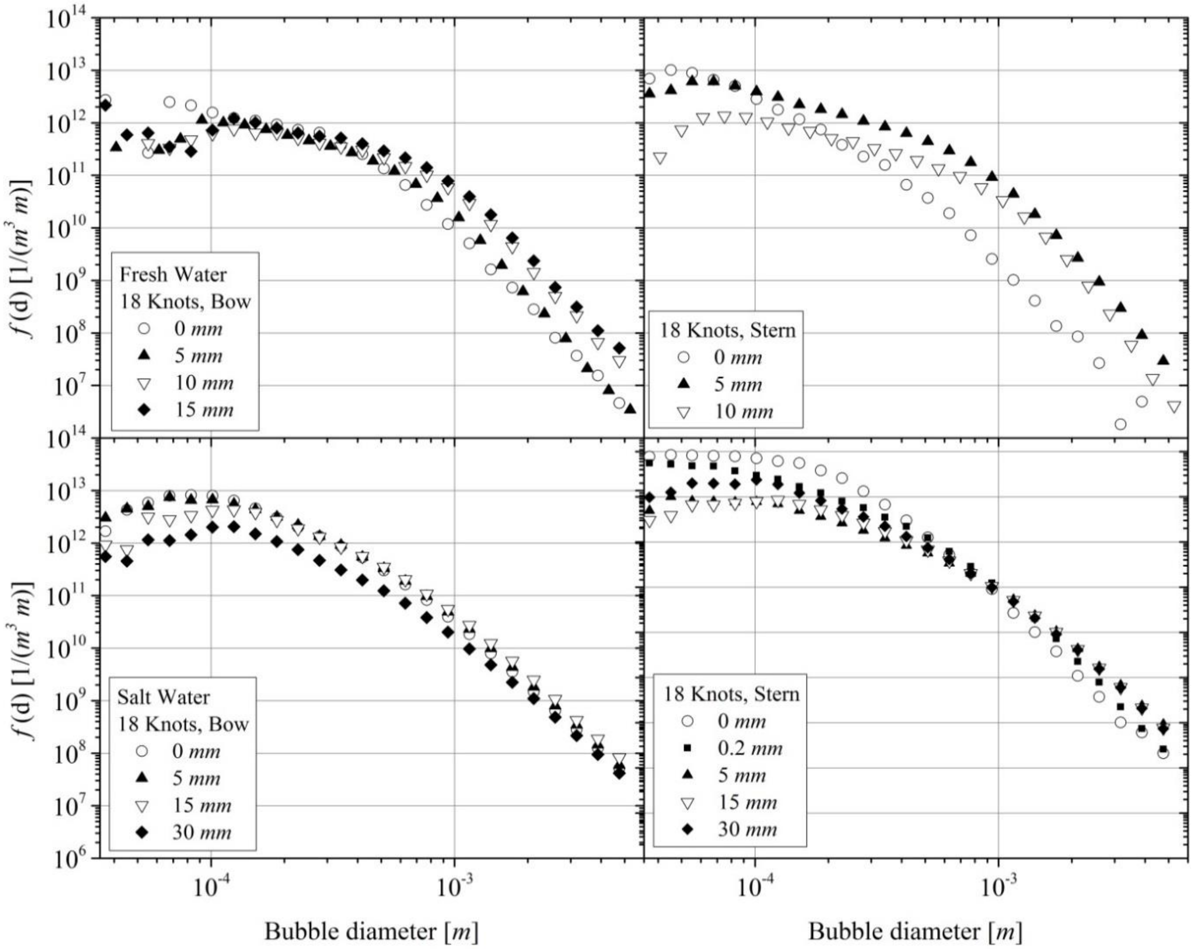

Figure 32: Bubble size distributions at 18 knots at different distances away from the hull, fresh and salt water

stern in fresh water, the void fraction shows a plateau, peaking at diameters from approximately $0.2\ mm$ to $0.75\ mm$. The peak for small bubbles is much higher at the stern than at the bow for salt water, and occurs at a smaller bubble size. At higher distances from the wall bigger bubbles are responsible for a larger percentage of the void fraction.

A direct comparison of normalized bubble size distribution and void fraction distribution can be seen in Figs. 34 and 35 for 10 (salt water only), 14 and 18 knots for 0 and 5 mm in salt and fresh water, respectively. The similarity of the size distributions in fresh and salt water at the bow is striking, indicating that the entrainment size distribution is weakly affected by the salinity of the water. The trend from larger bubbles to smaller from bow to stern at the wall is clearly

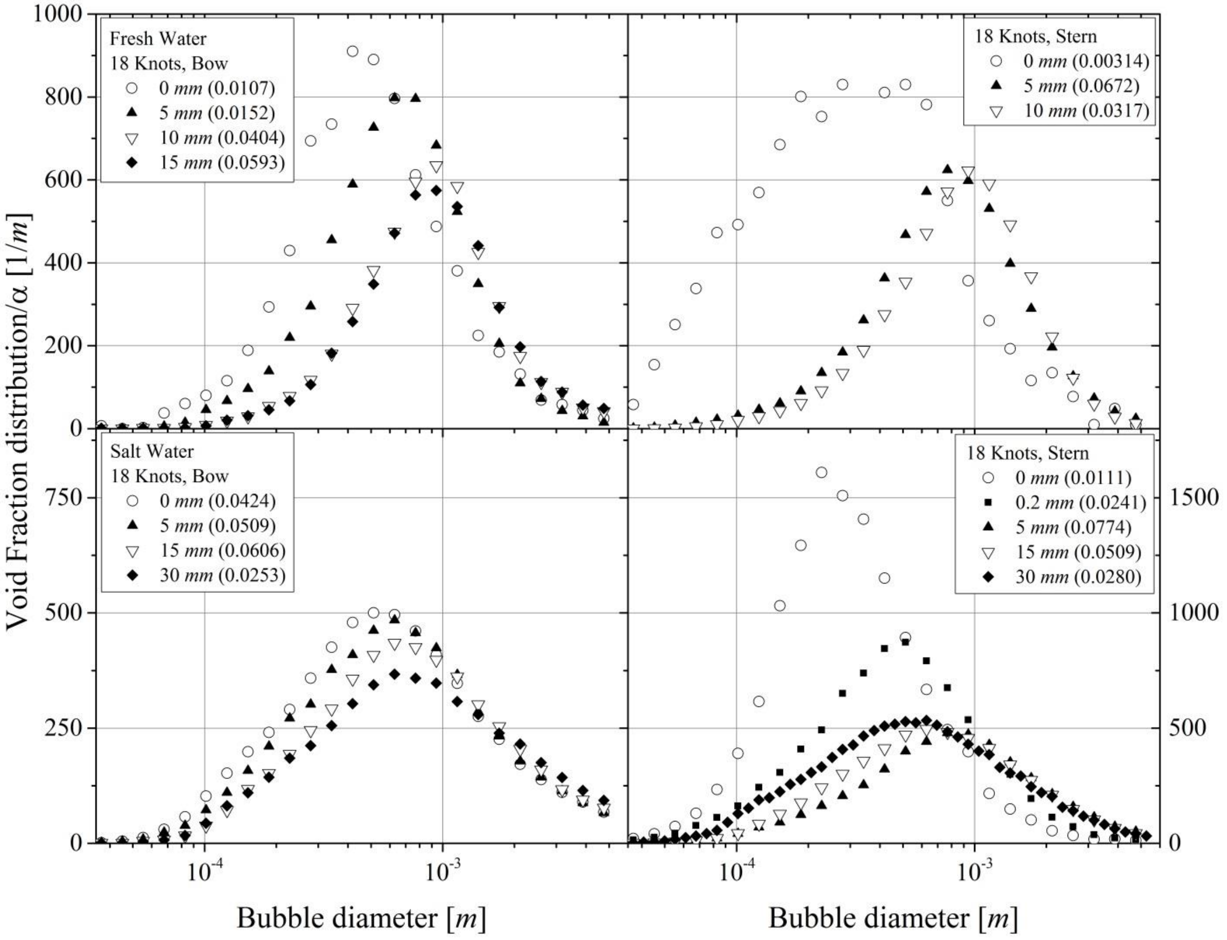

Figure 33: Normalized (by α in parenthesis) void fraction distribution at 18 knots at different distances away from the hull, fresh and salt water

evident here as well as the trend to show smaller bubbles as the probe gets closer to the wall. For all velocities, *f(d)* increases by approximately an order of magnitude from bow to stern for bubble sizes smaller than $0.5\ mm$. The inverse is evident for bubbles larger than $2\ mm$, where there is an approximate order of magnitude decrease in *f(d)* for bubbles larger than $2\ mm$ from bow to stern. The influence of the increasing shear and turbulence (§2.3.4) on bubble sizes can also be seen. For each incremental increase in boat velocity, there is a corresponding increase in *f(d)* for small bubbles which shows that the shear and turbulence are contributing increasingly to bubble breakup.

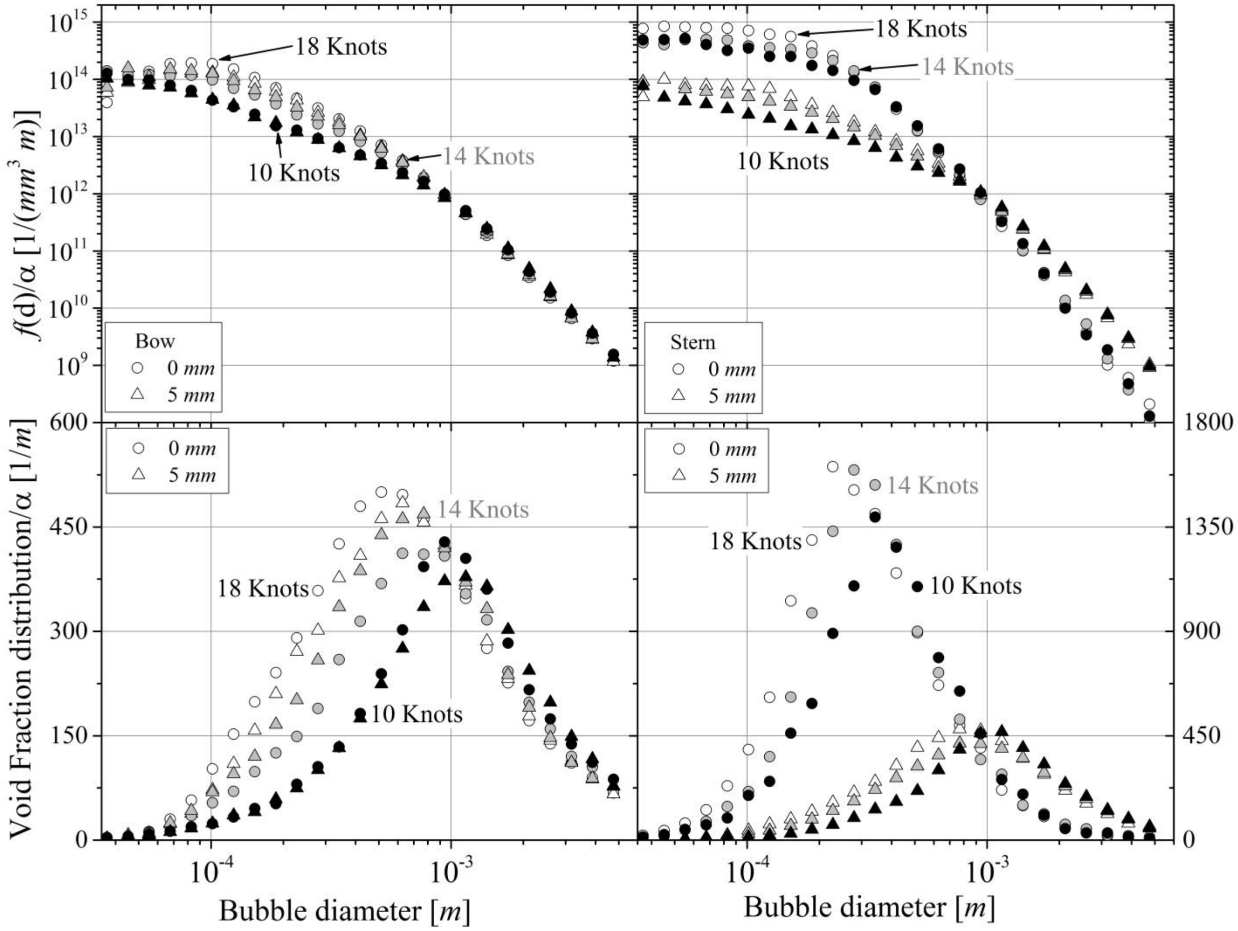

Figure 34: Bubble size distributions (top) and void fraction distribution (bottom) for 10, 14 and 18 knots at 0 and 5 mm from the wall in salt water

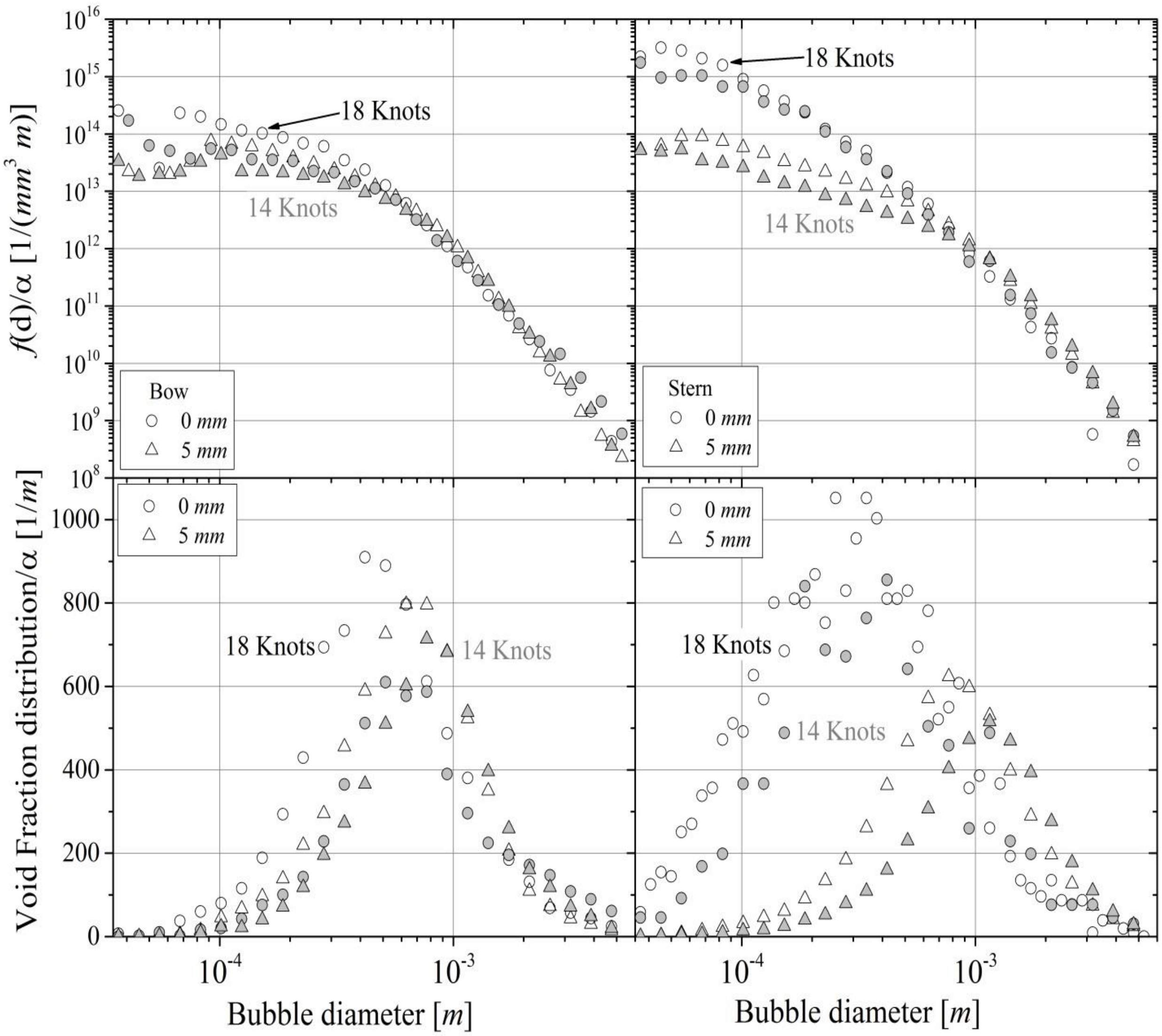

Figure 35: Bubble size distributions (top) and void fraction distribution (bottom) for 14 and 18 knots at 0 and 5 mm from the wall in fresh water

In general the increased number of very small bubbles right at the hull at the stern with respect to the bow for all speeds in fresh and salt water (see Figs. 29-33) indicates that strong breakup is taking place within the boundary layer. Very small bubbles are produced, measured to the limit of approximately 50 μm allowed by the probes. Estimations using levels of turbulence and shear computed with CFD show that bubbles as small as $200\ \mu m$ can breakup, but only in the first 200 μm away from the wall and with very small rate, see §0 and Figs. 3 and 4. Any breakup of a $200\,\mu m$ bubble will result in two equally sized daughters of $159\,\mu m$ in diameter (see §1.3.1.1 and Fig. 5). Some bubbles smaller than $150\,\mu m$ may be the result of breakup of larger bubbles with multiple smaller daughters, but the size distribution (Fig. 32) shows that the number of bubbles decreases quickly with bubble diameter and Fig. 5 shows that, unless unrealistically large turbulence intensities are present, daughter bubbles will not be very small. A $1.5\,mm$ bubble immersed in a turbulent dissipation $\varepsilon = 1500\,m^2/s^3$ will produce with maximum probability one $150\,\mu m$ bubble and one of approximately the original size. On the other hand, breakup of bubbles around 1 mm in diameter can reach break rates of up to $1000\ 1/s$ for distances of up to $1\,mm$ away from the wall, see discussion in §1.3.1.1, thus the production of very small bubbles but bigger than $200\,\mu m$ can be significant.

2.3.7 Limitation of measurement instruments and methods

Ideal double-tip local phase detection probes of infinitesimal size can measure the void fraction, bubble velocity and chord length distribution exactly irrespectively of the shape of the bubbles and without any assumptions. Computation of the bubble size distribution requires assumptions regarding bubble shape. The simplest assumption, used in this paper, is to consider all bubbles spherical (§2.1.6). More complex assumptions for shapes, like spheroidal, require the use of additional tips to measure the two parameters that define the size and shape of the spheroid. Assuming spherical bubbles in the data processing to obtain a size distribution results in an error of increasing magnitude as bubbles are more deformed. Since small bubbles deform little (see §1.3.1.2 and discussion therein), the uncertainty is higher for larger bubbles where the velocity gradient and thus the deformation are largest. Quantification of the resulting uncertainty is not straightforward and has not been attempted.

Measurements in the field necessitate a number of compromises. In the case of this experiment, the primary one is in the form of the measurement instruments used (§2.1.1). There is a balance between how sensitive the optical probes can be made to how long they will survive in the field. The necessity to use a sapphire fiber that is sufficiently large to last in the field yields a compromise to how intrusive it will be to the flow it will be measuring and how small of a bubble it can measure. The main limiting factor that this poses is in measuring the velocity of small bubbles. From Fig. 25, it can be inferred that the lower limit of the probes ability to measure bubble velocity is approximately $100\,\mu m$. This limit is the same for all boat speeds. One possible explanation for this limit is the combination of the increased surface tension with the reduced drag the bubbles of these sizes have. In effect, it becomes harder to pierce the bubble and it becomes easier for the bubble to decelerate and not be pushed by the fluid through the probe tips. With this in mind, it can also be presumed that, in general, there is a decreased likelihood of measuring bubbles smaller than $100\,\mu m$, causing an underestimation of the size distribution for the smallest bubbles. However, while the probe size limits how accurate the bubble velocity can be measured for small bubbles, it does not necessarily limit measuring the chord length of the detected bubbles. As long as a velocity can be measured the cord length, Eq. 17 will still be valid. The velocity takes into account both the leading and trailing edges of the bubble, and hence represents an average velocity for that bubble as it travels through the probe tips. Therefore, using that velocity along with the time in air for each tip, will yield an accurate measurement of chord length. The imposed limit of measuring bubbles smaller than $50\,\mu m$ (§2.1.1), is governed by the physical characteristics of the probes, namely the relative cross sectional area of the probe when compared to the area of a bubble of that size. Note that the above mentioned limitations do not limit the maximum size of bubbles that can be measured.

Another limitation of the optical probe design is the sheltering of the second probe tip from the first. This can be seen in Fig. 36, where the void fractions measured from both tips of a probe are shown. The sheltering of the second tip limits the number of bubbles that are pierced by the second tip, which directly affects the void fraction. This will limit the number of valid bubble pairs that are measured, as a bubble must be pierced by both tips in order to get a valid bubble velocity and hence chord length. Part of the contribution to sheltering of the second probe tip comes from bubble grazing, where the first tip either grazes the side of a bubble, where the curvature of the bubble is sharp enough that the bubble is not pierced, or the bubble is pierced,

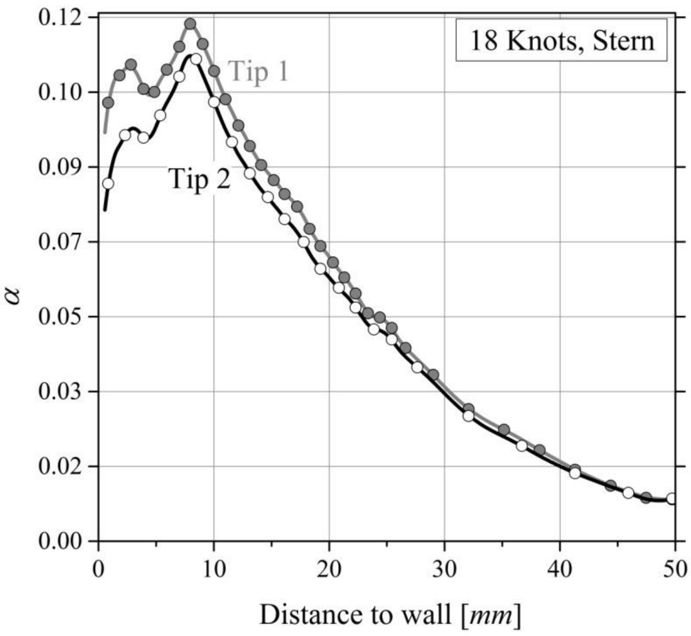

Figure 36: Comparison of void fraction for two tips

but is too far to the side such that the trajectory of the second tip does not intersect with the bubble.

2.3.8 Statistical convergence of measured values

The convergence of a random data set measured in time is defined when its result (typically the mean of the data set) is not changed by the acquisition of additional data (Bendat and Piersol, 1971). Given an infinite number of data, the true mean of a random data set, μ_x, can be computed. In practice though, an infinite data set cannot be collected, but the sample mean $\bar{x}$ of the finite data set containing N measurements can be computed. Using the statistical confidence interval for $\bar{x}$, it can be determined with a certain probability that the variable x has statistically converged when the value of the statistical convergence error has fallen below a predetermined desired value. The confidence interval of $\bar{x}$ usually requires some knowledge of the distribution of the random variable x. If the data falls within a normal distribution, the

Student t-distribution can be used to estimate the confidence interval of $\bar{x}$. In the case of an unknown distribution, or data that has time-varying transient components, a normal distribution is not ideal and the more forgiving Tchebycheff inequality (Eq. 27) is used to estimate the confidence interval.

$$\text{Prob}\left[|\bar{x}-\mu_x| \leq c\frac{\sigma_x}{\sqrt{N}}\right] \geq 1-\frac{1}{c^2} \tag{27}$$

In Eq.27, μ_x and σ_x are the true mean and true standard deviation of x, respectively, $\bar{x}$ is the sample mean and N is the sample size, c is any positive real number. Eq. 27 can be read as the probability that the true mean of x is between the interval of $\bar{x} \pm c\sigma\_x/\sqrt{N}$ is greater than $p = 1 - 1/c\text{^}2$ regardless of the distribution of x. As the true standard deviation σ_x cannot be directly measured nor is known, s_x, the sample standard deviation is used as the best approximation of σ_x. This results in the best approximation of the confidence interval and the statistical convergence error to be defined as:

$$\tilde{d} = c\frac{s_x}{\sqrt{N}} \tag{28}$$

$$E_{SC}(\%) = \frac{\tilde{d}}{\bar{x}} = \frac{c}{\sqrt{N}}\frac{s_x}{\bar{x}} \times 100 \tag{29}$$

Figures 37 - 40 show the cumulative moving average for void fraction (Eq. 30), time-of-flight velocity (Eq. 31), chord length (Eq. 32) and statistical convergence error (Eq. 29) for the 95% confidence interval ($c = 4.5$) for the same quantities.

$$\bar{\alpha}^*_{n+1} = \frac{\alpha_{n+1} + n * \bar{\alpha}^*_n}{n+1} \tag{30}$$

$$\overline{U_{tof}}^{*}_{n+1} = \frac{U_{tof_{n+1}} + n * \overline{U_{ToF}}^{*}_{n}}{n+1} \tag{31}$$

$$\overline{CL}^{*}_{n+1} = \frac{CL_{n+1} + n * \overline{CL}^{*}_{n}}{n+1} \tag{32}$$

In Eq. 30, each n point is the void fraction of Eq. 19 with an integration time of 1 s. In equations 31 and 32 n is value of CL (Eq. 18) and U_{tof} (Eq. 16) with values of cl_i (Eq. 17) and $V_{tof,i}$ (Eq. 15) taken between time $t = n \pm 0.5\ s$.

The flow around the Kann boat has transient components (as seen in §2.3.2) which adversely affect the convergence rates of the quantities measured. The void fraction is seen to converge most slowly and its statistical convergence error rarely decreases below 10% regardless of the amount of data collected. Conversely, the time-of-flight velocity and cord length converge at a relatively quick rate despite experiencing the same transient components. This variation in convergence is due to the nature of each quantity measured. Each additional bubble velocity and chord length measured reduces the error in the estimated average velocity and chord length regardless of any time dependent variations in the flow. The void fraction however, which is not only defined by the number of bubbles and their chord lengths (time in air), but also by *when* they are measured is more strongly influenced by the transient flow around the boat. At the bow location, where the two-phase boundary layer has not become fully developed, the transient flow components are observed as being larger than at the stern, where the boundary layer is more developed. For this reason, the statistical convergence error tends to be larger at the bow than at the stern.

As seen in Figs. 3 and 4, the convergence is dependent on the location of the measurements. Closer to the wall, where the RMS fluctuations are largest (§2.3.4), values converge at a slower rate than further from the wall, where the fluctuations are reduced.

In general, the void fraction is slower to converge than bubble velocity or chord length. Regardless of the transient nature of the flow, if all bubbles have about the same velocity or chord length distribution, every bubble measured reduces the error of your estimated average velocity and chord length. So therefore the error is a function of the number of bubbles measured and can be defined as 1/sqrt(# bubbles). Void fraction, as discussed on b), depends on *when* you measure those bubbles.

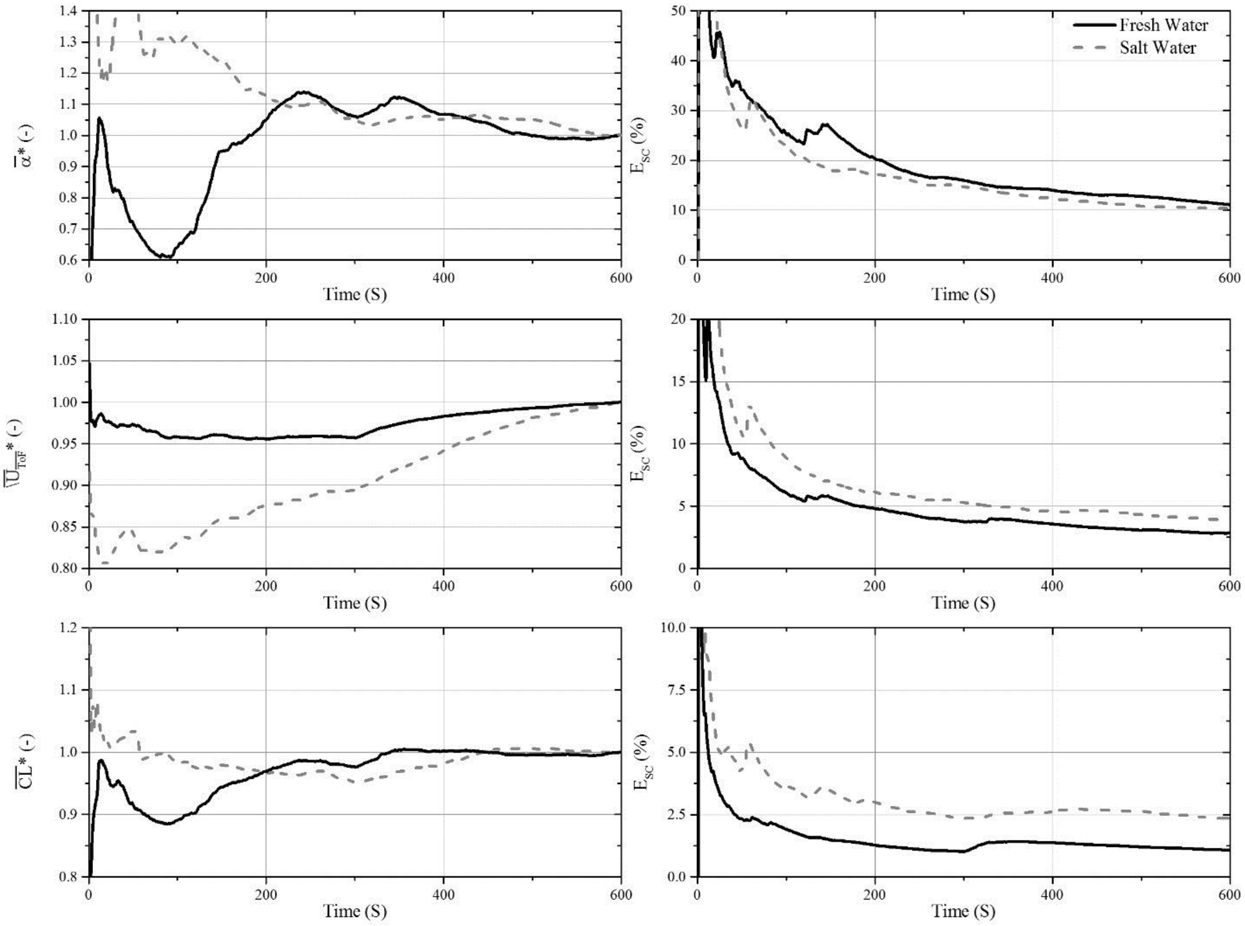

Figure 37: Cumulative moving average (left) and statistical convergence error (right) for 5 mm at the stern, 14 knots

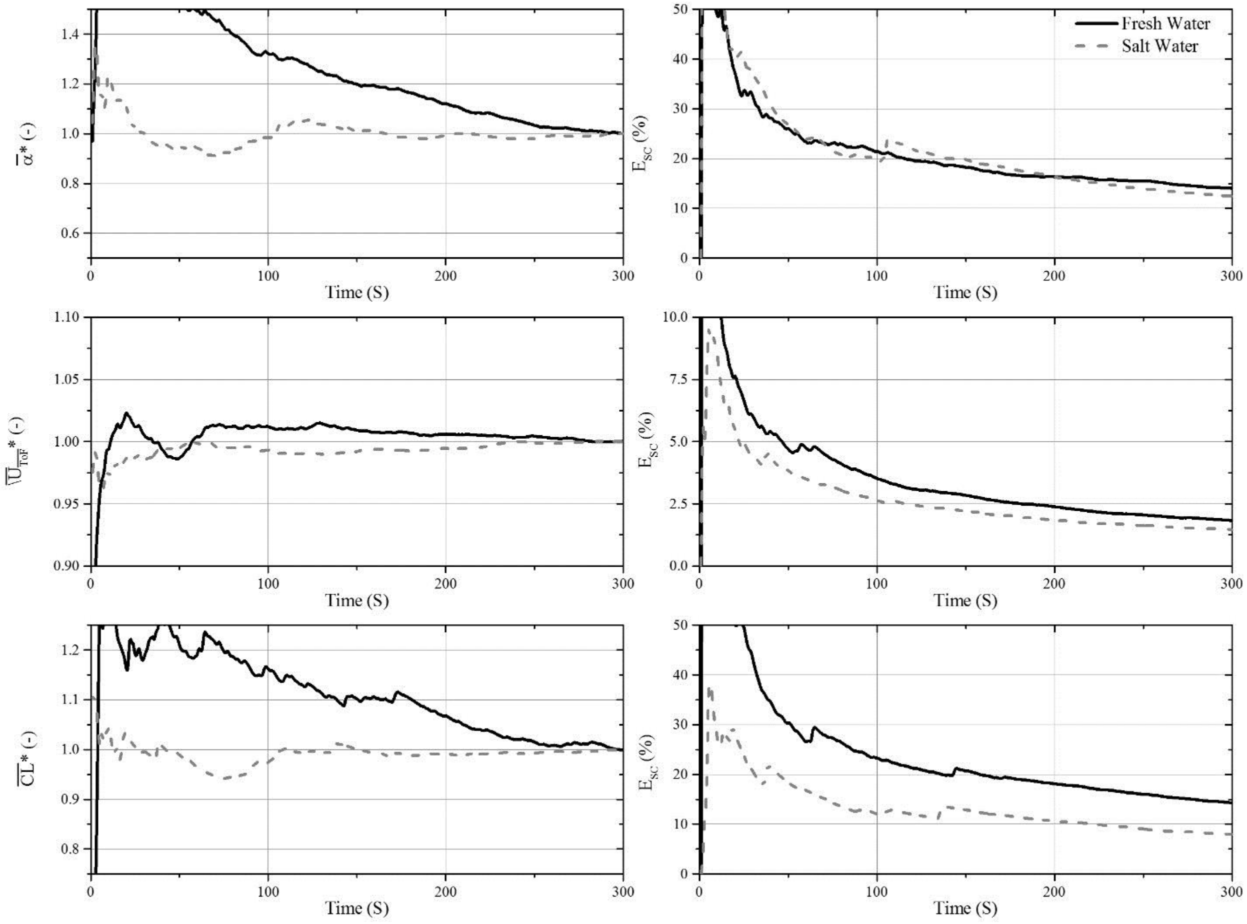

Figure 38: Cumulative moving average (left) and statistical convergence error (right) for 5 mm at the bow, 14 knots

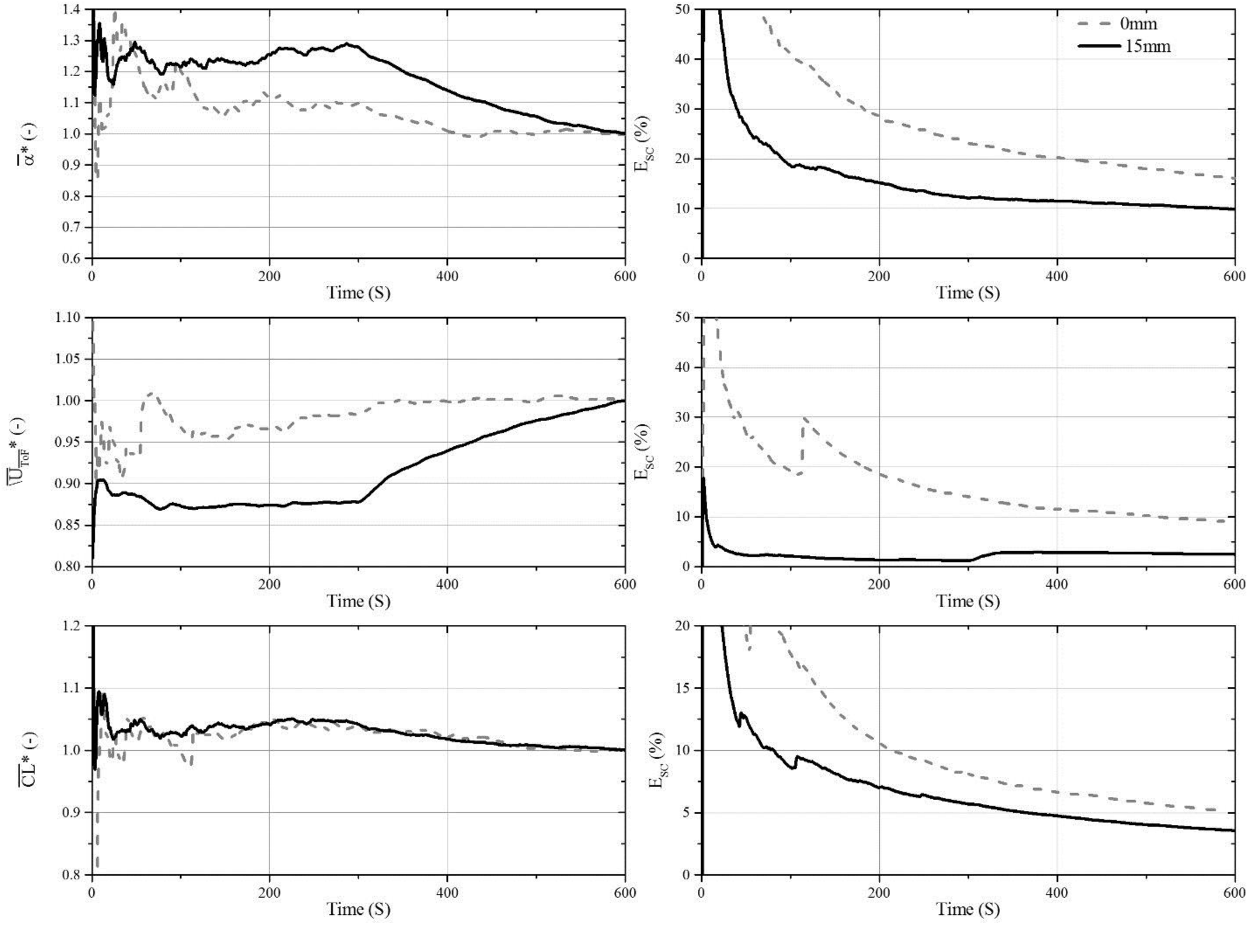

Figure 39: Cumulative moving average (left) and statistical convergence error (right) at 0 and 15mm at the stern, in salt water at 14 knots

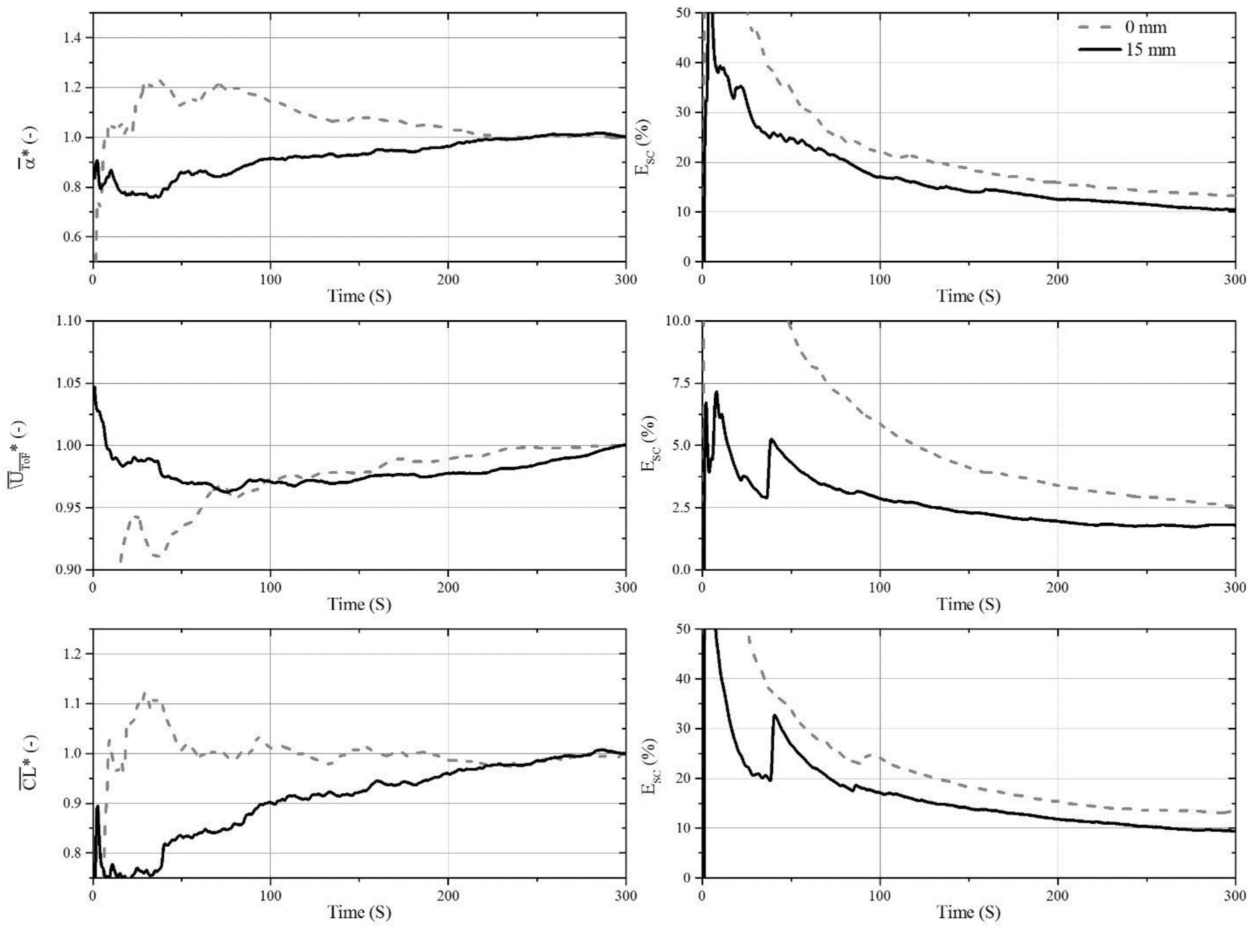

Figure 40: Cumulative moving average (left) and statistical convergence error (right) at 0 and 15mm at the bow, in salt water at 14 knots

CHAPTER 3: SINGLE TIP PROBES

This section examines some of the limits presented in §2.3.7 and discusses how single tip optical probes can resolve them. This section also serves to document the continued development of multi-phase measurement tools.

3.1 Introduction to single tip probes

While single tip probes have long been used to measure void fraction (§1.5.1), it is not until more recently that the ability to measure bubble velocity and size has been researched. Having only one tip requires a more complex algorithm for measuring velocity that is more dependent on probe geometry and, often, flow characteristics. Direct measurement was briefly discussed in §1.5.1, where the velocity of a bubble is measured using the characteristics of the rising signal. This methodology is more thoroughly discussed below.

Abuaf *et al.* (1978) were among the first to propose and evaluate that a single fiber optic probe tip could be used to infer the velocity of the dispersed phase in a two phase flow. They proposed that the bubble penetration time is a function of the bubble velocity. The bubble penetration time, also known as rise time or transition time, (T_u) is defined as the time from the first increase in signal (bubble arrival) to the ultimate steady state signal value. Abuaf *et al.* (1978) suggested that for bubble velocities greater than 40 cm/s, the signal rise time is roughly proportional to a constant divided by the bubble velocity (See Fig. 41):

$$T_{u,i} = \frac{Const}{V_i} \qquad (33)$$

For bubble velocities below 40 cm/s, it was suspected that the effects of surface tensions dominate over inertial effects and as a consequence the penetration time is longer than $Const/V_i$. In additional Abuaf *et al.* (1978) also analyzed the behavior of the 'de-wetting' of the probe tip. They proposed that as bubble velocity increases the water film on the probe tip doesn't have sufficient time to dry and hence results either in there being a delayed reation time or in the

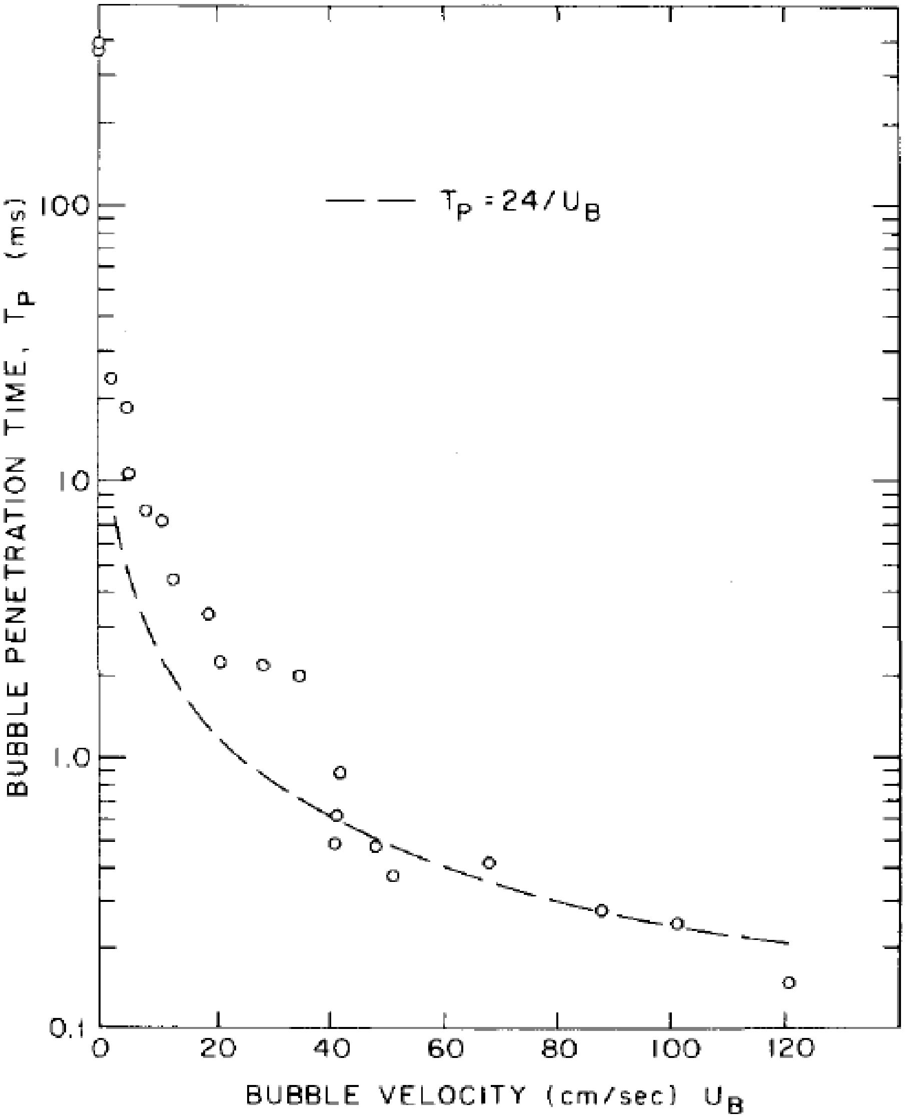

Figure 41: Bubble penetration time as a function of bubble velocity (Abuaf *et al.*, 1978)

probe not registering the transition at all.

More recently LEGI (Laboratoire des EÂcoulements GeÂophysiques et Industriels) has been leading the continued development of single tip optical phase detection probes (Cartellier and Barrau, 1998; Barrau *et al.*, 1999; Cartellier, 1998). LEGI defines the latency length (herein called L_u), which similar to Abuaf *et al.* (1978), corresponds to the effective active length of the sensor tip. In the case of very small probe tips (3 μm achieved by Gouirand, 1990 – in glass fiber) the active region goes beyond the probe tip, which is primarily due to the inconsistencies in the core/cladding thickness as the glass fibers are heated and stretched to achieve the reduced fiber diameters. This, along with minor manufacturing defects in the tips necessitates the use of a calibration procedure to determine L_u on an individual sensor basis.

The probes developed by LEGI are made from silica glass fibers that have been acid

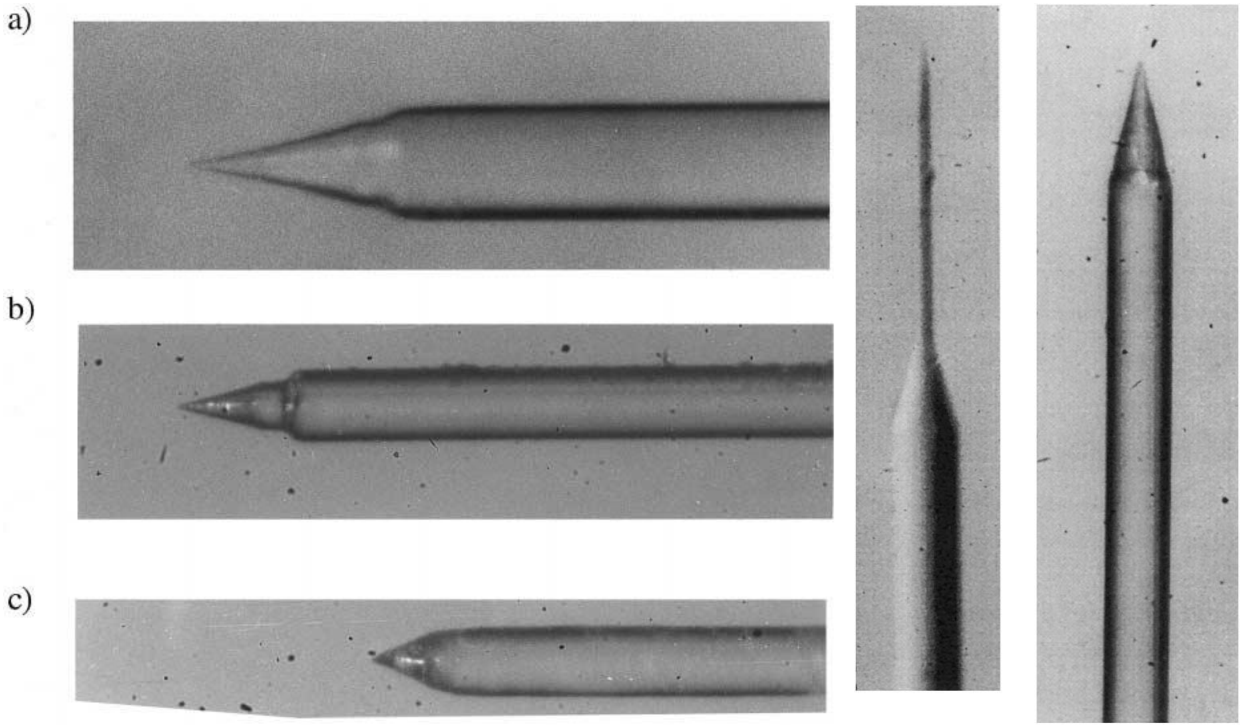

Figure 42: Some probe tips produced by the etching technique (the fiber external diameter root is 140 µm). From Cartellier and Barrau, 1998 (left) and Cartellier, 1998 (right)

etched into a number of different shapes. Fig. 42 shows a selection of the probe tips developed and tested by LEGI. The design objective was to optimize each tip for both sensitivity and repeatable manufacturing while controlling L_u. The probes developed behave admirably under controlled circumstances and yield minimal error (<10%) under controlled experiments in the determination of bubble velocity. The sensitivity of the probes to uncontrollable parameters experienced in experimental flows was analyzed as well, where it was found that T_u can increase 3 fold as the probe impact angle changes from normal to 45º. Discriminating on the shape of the bubble signature is possible when the bubble shape is ordinary (spherical/ellipsoidal). Ultimately though, they find that error increases drastically, namely in void fraction, as the velocity of the flow increases (up to $2\,m/s$ in their tests). Also, their tests were conducted with bubbles primarily larger than $1\,mm$.

Addressing the fragility of glass probes, Vince *et al.* (1982) designed and fabricated a probe made of diamond intended for high temperature flows. The probe design was optimized using a 2-D light ray tracing computer simulation and resulted in an optimal probe angle of 45º. Fabrication of the probe at the desired dimensions ($0.3\,mm$, similar to Miller and Mitchie, 1969) proved too costly, necessitating the increase in tip diameter to $0.7\,mm$. The probe was tested with a low pressure air/water flow and was reported to work.

Recent developments in focused ion beam machining with femtosecond lasers (Kou *et al.*, 2010) has opened up the window for new innovative single tip probe geometries. With the ability to create geometric features on the micro scale in ever stronger and harder materials, the prospect of creating a single tip optical probe that is capably of measuring sub $1\,mm$ bubbles in both violent and otherwise hostile flows is promising.

3.2 Dual angle single tip

The premise of the dual angle single tip probe is to get two positive transitions in the return light signal. Having two transitions reduces the uncertainty of the velocity measurement, as there are two discreet events that can be used to measure the velocity in addition to the rise time, Eq. 33. The probe was designed at the practical limits of Eq. 9. With Sapphire ($n_{f,Sapphire} = 1.76$), in water the limit at which refraction will occur is 34° and in air, internal reflection occurs at 51°. Using a Sapphire fiber with a diameter of $125\,\mu m$, two angels 35° and 50° were polished onto the fiber (Fig. 43). The shaping of the fiber was done in the same method as used for the dual tip probes (§2.1.1). While the diameter of the probe is not ideal for measuring bubbles smaller than $\sim 500\,\mu m$ (it is believed that below $500\,\mu m$, the bubble's surface tension will cause it to deflect off the probe, rather than be pierced by the probe), the probes robust shape makes it ideal for hostile environments.

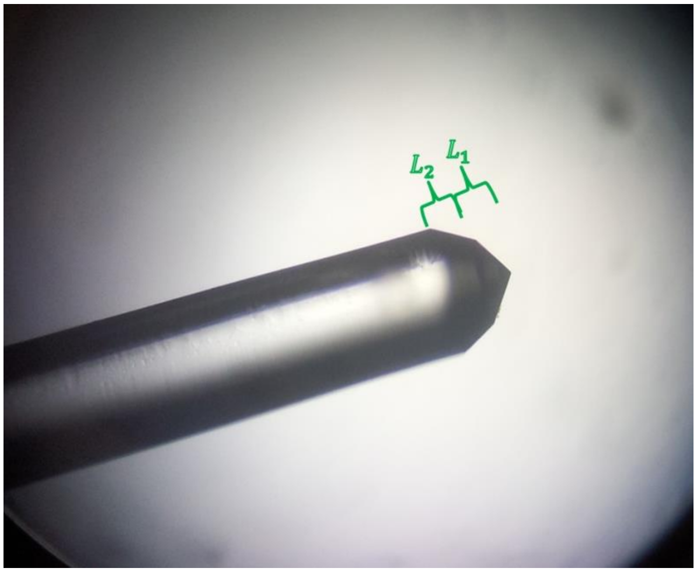

Figure 43: Double angle single tip probe

The single tip was connected to a fiber optic cable with core/cladding diameters of 62.5/125 µm. Using a National Instruments (NI) – 5114 8-bit 250 MS/s oscilloscope the raw analog return signal from the RBI optoelectronic units was collected for processing.

3.2.1 Processing methodology and sample signals

Using a sample flow created by an air pump injecting air into a quiescent beaker of water, bubble signature signals were collected for analysis. A typical signal has 3 distinct transitions in both the rising edge and falling edge. Referring to Fig. 44, the first transition occurs as a bubble starts to be penetrated by the probe and the signal begins to rise. This marks the beginning of the rise time of the bubble and is denoted $t1_r$. The second transition occurs as the bubble's interface transitions from the first angle to the second angle, denoted $t2_r$. Finally, as the bubble's interface covers the entire tip, and the final steady state signal amplitude is reached, the third transition time, $t3_r$ is measured. Though less pronounced on the falling edge of the bubble, as the bubble exits the probe, three transition times can also be marked ($t3_f$, $t2_f$ and $t1_f$), marking the bubble's interface crossing the same three transition locations as when it was pierced.

Hence, using the two lengths of the probe tip (L_1 and L_2) there are two distinct values that can be used to compute the interfacial velocity of a bubble:

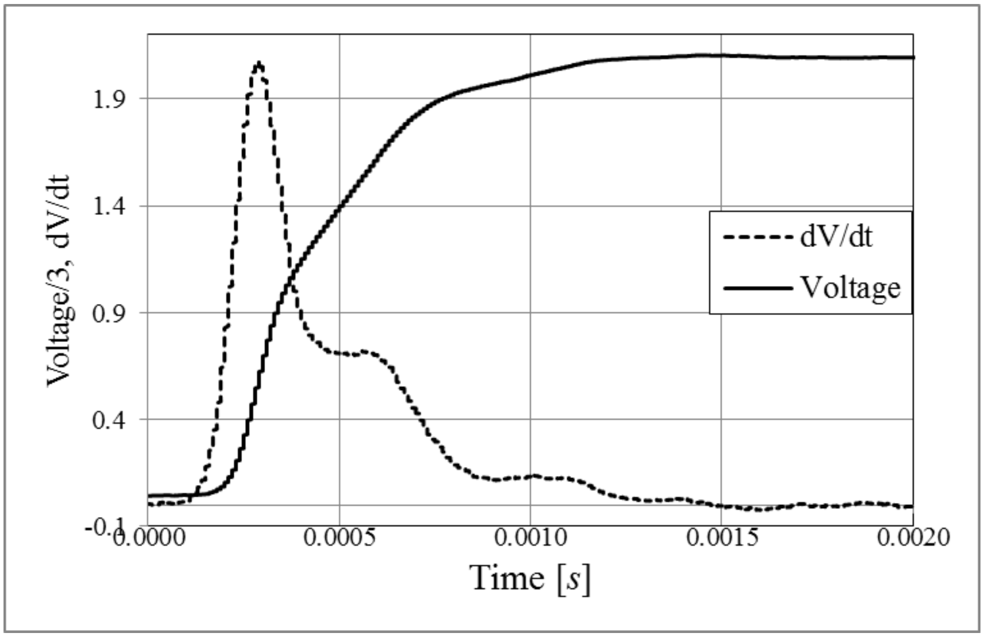

Figure 44: Sample leading interface signal from dual angle single tip probe

$$V1_{i,(r,f)} = \frac{L_1}{\left(t2_{i,(r,f)} - t1_{i,(r,f)}\right)} \tag{34}$$

$$V2_{i,(r,f)} = \frac{L_2}{\left(t3_{i,(r,f)} - t2_{i,(r,f)}\right)} \tag{35}$$

Taking the average of $V1_{i,(r,f)}$ and $V2_{i,(r,f)}$ yields the bubble velocity. In the probe tip (Fig. 43), the values of L_1 and L_2 are $29.6\,\mu m$ and $36.2\,\mu m$, respectively. Note that the signal lags significantly in reaching its steady state value, which results in an abnormally slow velocity. It is suspected that the bubbly is slowed significantly by the lack of inertia the bubble has at such a low velocity and the bluntness of the probe tip. This probe design has been succeeded by the single angle notched tip discussed below.

3.3 Single angle notched tip

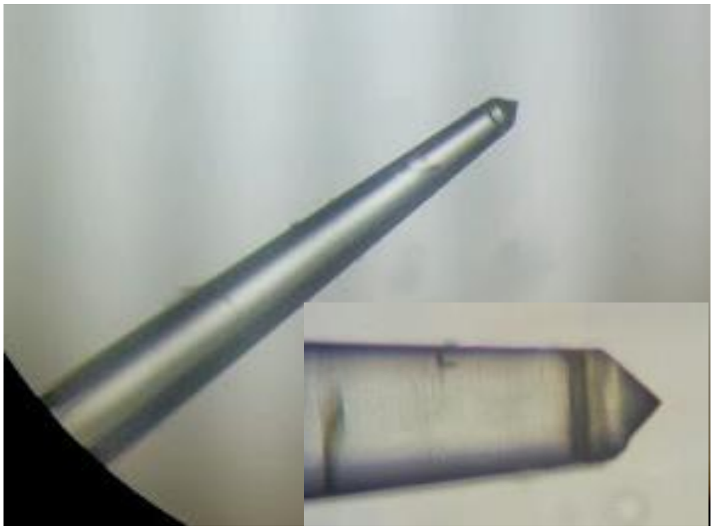

Figure 45: Singe tip notched probe with detail of the tip

The objective with the single tip notched probe was to make a versatile probe that would be able to accurately measure sub-50µm bubbles with minimal effect on the surrounding flow. Using only a single tip from the double tip probes of §2.1.1 a notch was laser machined into the fiber to create a groove that goes 360º around the perimeter of the fiber (Fig. 45). With the 5 degree axisymmetric taper on the fiber prior to the tip, the effective diameter that a bubble sees when its interphase crosses the groove is ∼40 μm.

3.3.1 Processing methodology and sample signals

Using the same equipment as §3.2 sample signals were collected. Fig. 46 shows the voltage signal along with the derivative (dV/dt) of the voltage. The derivative provides a 'magnified' view of the transitions in the voltage signal as the bubble travels along the probe. Referring to Fig. 46, as the bubble's interface crosses over the probe tip, the voltage signal begins to rise ($t1_r$), and can clearly be seen by the spike in dV/dt. When the interface reaches the notch in the probe, a slight 'bump' in the voltage signal is visible and marks $t2_r$. Using the length from the probe tip to the groove, the velocity can be computed similar to Eq. 34.

Note that on the rising edge the notch's signal is very small and is not registered in dV/dt. This is due, in part, to the saturation of the returning light from the tip and the relative

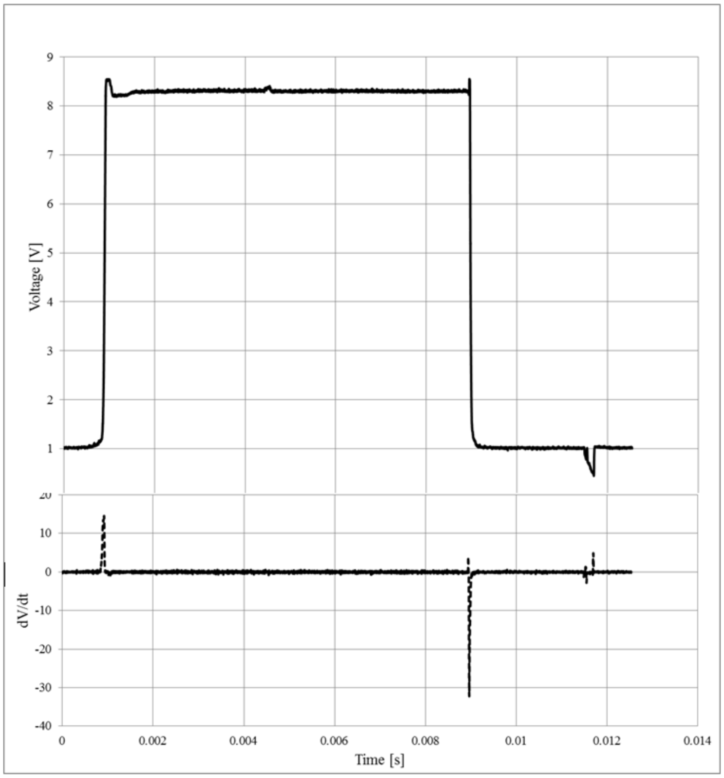

Figure 46: Sample signal from single notched tip

high signal-to-noise ratio in dV/dt. On the falling edge the notch is much more visible in both the signal and dV/dt (Figure 46). It is presumed that this is due to the reflective nature of the bubble's interface as it crosses the notch.

An emphasis must be placed that the development of the single tip probes is at its beginning and much work is necessary to continue the development of these ideas and to better understand their operation.

3.4 Single taper probes

Single taper sapphire tips, with one continuous taper with an axis-symmetric angle less than i_c in Eq. 9, can be used to generate the phase indicator function, as well as directly measuring bubble velocity. The diagram in Fig. 47 shows the relative sizes of a single taper tip to a double angle tip (red). In order for a single taper tip to work properly, it is necessary for the final polishing (§2.1.2) to be less than 0.5 μm, effectively making the surface 'mirror-like' and able to easily internally reflect the IR light source.

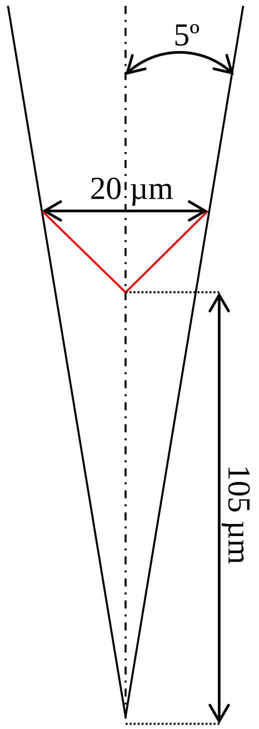

Figure 47: Comparison of single taper to double angle probe tips

Using the laws of geometrical optics, a simple 2-D simulation was made. The path of light rays originating from the IR laser source are assumed to move in straight lines within the sapphire tip, with axis-symmetric taper angle β (See Fig. 48). Neglecting the effects of attenuation (Beer's law) and reflection and refraction losses (Fresnel laws), light reflects off of the interphase of the probe at its incident angle or refracts into the surrounding medium if $\varphi < i_c$ or $\varphi \geq i_c$, respectively, as determined by Snell's law of refraction. Each subsequent reflection, yields an incident angle relative to the tip interface, φ_1, which is equal to the previous incident angle

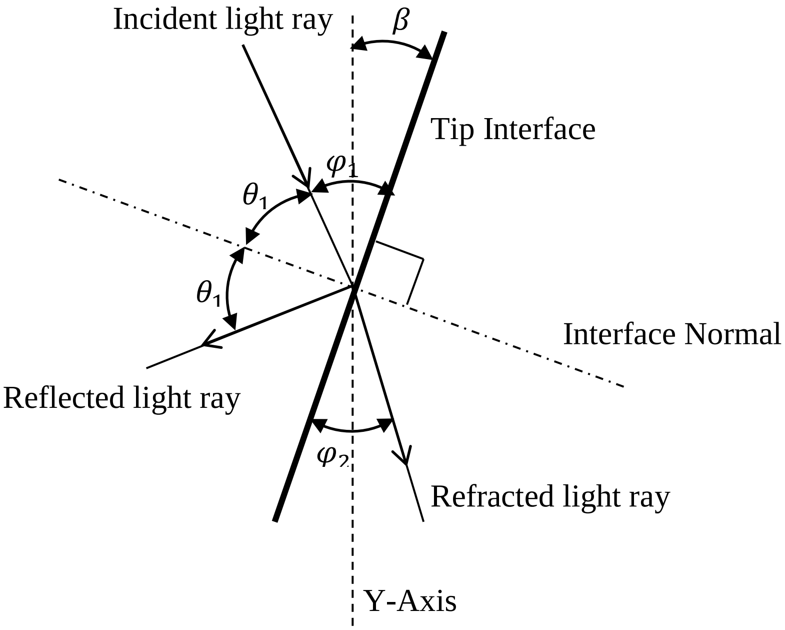

Figure 48: Light reflection and refraction at probe interface

plus $2 * \beta$. Hence, as the light is reflected down the taper, its angle with respect to the tip interface continually increases. In the case of the probe tip being in air, the internal reflection continues, until the reflected angle causes the light to return back up the fiber. In water, the light reaches i_c and then refracts into the water.

As the light entering the probe tip is not a precise point source, but rather distributed throughout the circular cross-section of the sapphire, the location of where the critical angle causing refraction changes linearly along the length of the tip depending on the radial source of that precise light ray. An example of this is shown in Fig. 49, where light originating from $r/d_f = 0.95, 0.50$ and 0.15 is traced down the fiber until it either refracts (green lines) or reflects (red line). Herein, the active length of the tip is considered to be the length from the absolute tip of the taper to the location where a light ray entering at $r/d_f = 0.99$ refracts into water (i.e. $\varphi_1 \geq i_c$). Note that the number of reflections to achieve refraction/internal reflection

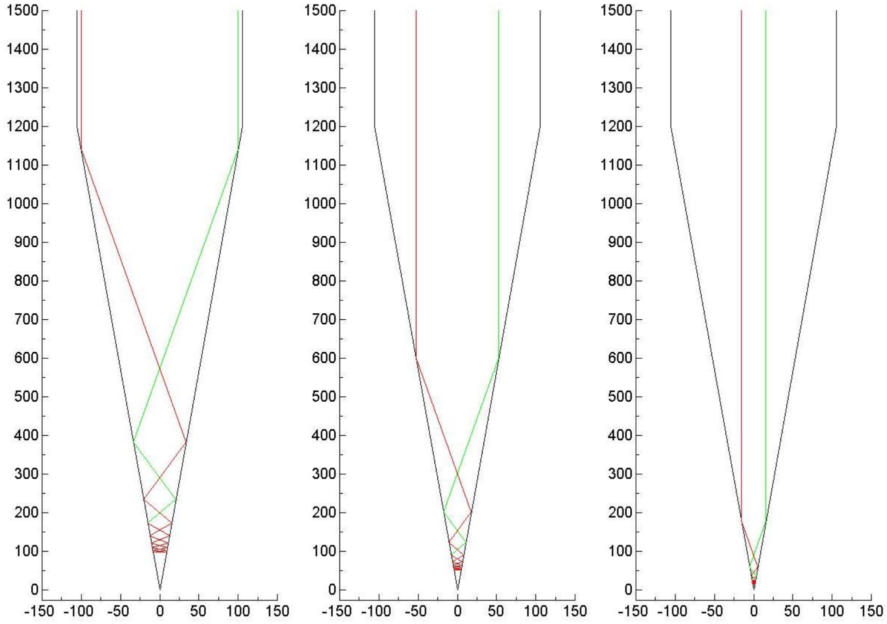

Figure 49: Light tracing from $r/d_f = 0.95, 0.50$ and 0.15 with green lines corresponding to path of light in water and red lines corresponding to path of light in air

is independent of the radial location of the incident light; it is solely dependent on the taper angle of the fiber and the indexes of refraction of the sapphire and surrounding medium, which determine i_c.

Using fiber diameters of $d_f = 210\,\mu m$ and a taper of 5°, the active length of the tip is $180.5\,\mu m$ long. Controlling the active length of the tips can be done by using different diameter fibers, to the extent of their availability, or by controlling the taper angle. Larger taper angles result in smaller active lengths, with the limit being 45°, where only two reflections are necessary to have complete internal reflection. Longer active lengths are achieved by using small taper lengths, with the limit for a fiber diameter of $d_f = 210\,\mu m$ being $182.9\,\mu m$. The practical limit of small taper lengths is dictated primarily by the ability to fabricate fibers will tapers less than 1° and also the Fresnal equations. In order for the light traveling down a tapered tip to reflect back up the tip, it must reflect within $\beta°$, the taper angle, of the normal to the taper. Considering it takes $90° - 2 * \beta°$ reflections to reach the angle that is necessary, the transmission and reflection coefficients start to play a role as the number of reflections increase. The ratio of transmission-to-reflection increases when approaching the normal, and hence the more light is lost through transmission and the intensity necessary to complete the path becomes large. With modern pigtail lasers, this limit is dwarfed by the practical limitation of fabricating a tip with such a sharp angle.

CHAPTER 4: PROBE TIP CHARACTERIZATIONS AND VALIDATION

This chapter is dedicated to better understanding the bubble piercing behavior and the corresponding signal created by various probe configurations. Additionally, this chapter documents the operating window in which the probes and processing methodologies are valid in. As an addendum, a differential threshold processing methodology is presented in §4.7.

4.1 High Speed test loop facility

To properly characterize the optical phase detection probes in a bubbly flow, a high speed test loop was designed and constructed. The objective of the test loop facility was to simultaneously acquire the analog signal from the probes of §2.1.1 and 3.4 along with high-speed video of the probes piercing bubbles. The test loop, shown in Fig. 50, consists of $38 \times 38mm$ test section that is $254\ mm$ long. The test section is fed by a 20-1 area contraction. Water was circulated with a $1.1\ kW$ centrifugal pump fed from a head/overflow tank. Within the test section, capillary tubes provided the source for bubbles and were placed up-stream of the probes. Bubbles injected by the capillary tubes were tracked using a Photron APX RS high speed camera, capable of 250,000 frames per second, with illumination provided by circuit on board (COB) light emitting diodes (LEDs). As the bubbles were pierced the analog return light signal was captured using a PCI 250MHz oscilloscope.

The objective of the characterization was to reveal the level (if any) of deformation that the bubbles experience when pierced by the probes as well as a detailed understanding of the piercing/exiting to signal rising/falling relationships. This information was collected for a representative selection of bubble sizes and serves as a vital component to better understand the influence of the probes on bubbles. Further, with this characterization, tuning of the double-threshold technique used in digitizing the analog signal will be possible.

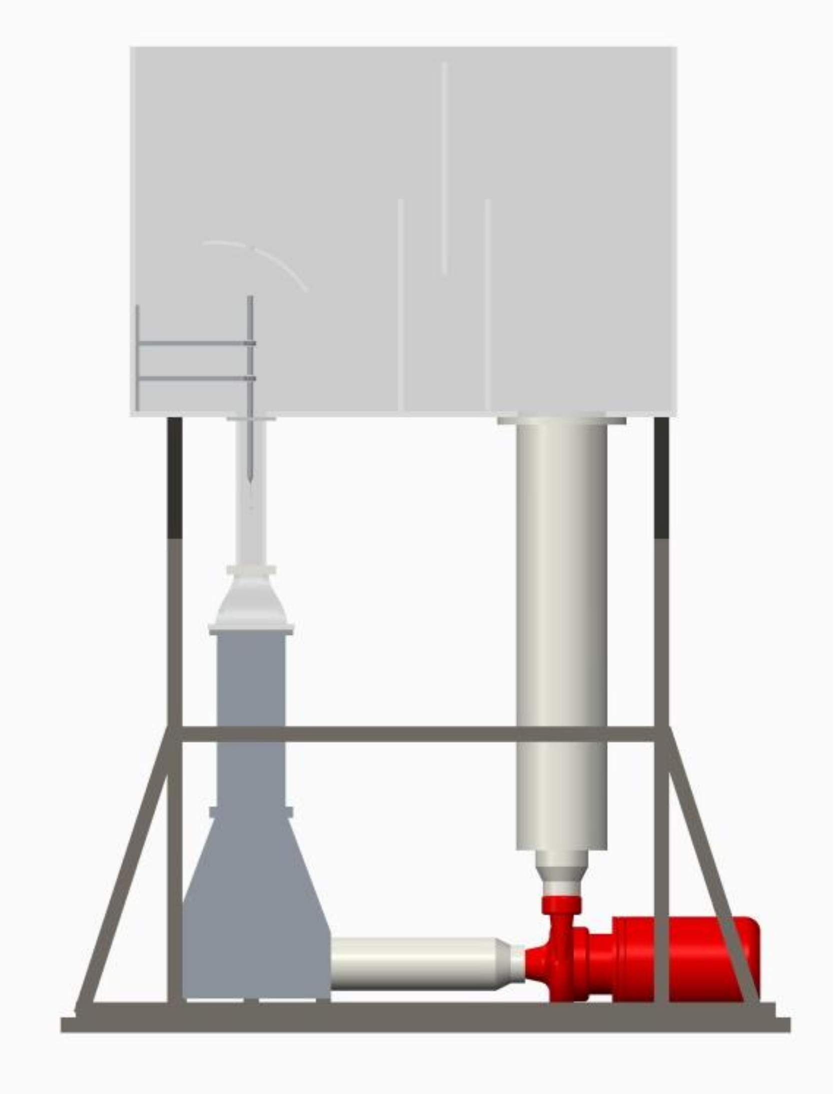

Figure 50: High speed test loop

4.1.1 Characterization of test section

Characterization of the test section was carried out using Particle Image Velocimetry (PIV). A 6 watt $532\ nm$ solid state laser fitted with sheet generating optics illuminated the test section in the plane parallel to the flow direction. An Integrated Design Tool (IDT) NX4-S2 high speed camera fitted with a $105\ mm$ Nikon lens was used to capture single exposed images at a frame rate of 8 kHz and a resolution of 1024 x $256\ pixels$. The water was seeded with neutrally buoyant silver coated hollow glass spheres, which reflected the laser light to the camera optics. The images were processed in a time-series configuration with a multi-pass $32 \times 32\,pixel$ window with 50% overlap using LaVision's DaVis 8.1 software.

Due to the physical construction of the contraction and test section, the view window into the test section is obstructed every $15\,mm$, and hence, PIV measurements were carried out between the obstructions, giving a window view of the flow. PIV measurements were conducted in the plane of the air injector to assess the quality of the flow. Results of the measurements are shown in Fig. 51. With the test loop set to run at a velocity of $V_o = 7.8\,m/s$, there is minimal

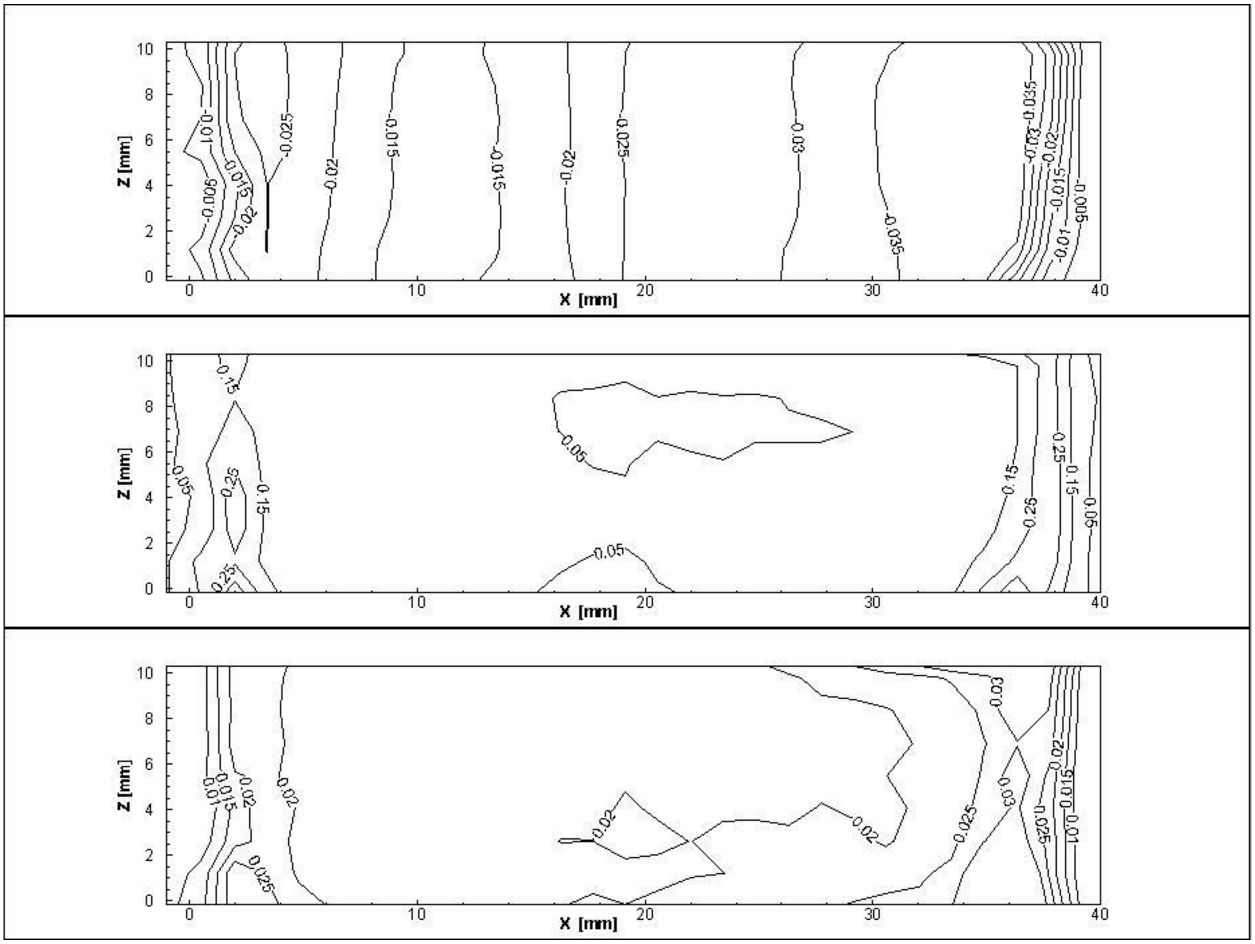

Figure 51: Test section cross flow, U_x/V_o (Top), cross flow RMS fluctuations, $U_{x,rms}/V_o$ (Middle), and vertical RMS fluctuations V_{rms}/V_o (Bottom)

cross flow and RMS fluctuations in the test section. From the top plot, the cross flow velocity (perpendicular to the flow direction) reaches at a maximum of 0.025% of V_o with RMS fluctuation (middle) not exceeding 0.15% of V_o. From Fig. 51, bottom, it can be seen that there are minimal RMS fluctuations in the vertical direction. The lack of any significant cross flow helps in having consistent bubble formation and subsequent trajectories, and hence clean, predictable bubble piercings, which is paramount in capturing bubbles small bubbles traveling at high velocities.

4.2 Plunging test facility

In addition to the high speed test loop, a facility able to plunge the probes in and out of a quiescent fluid was used. The objective of this facility is to quantify the drying and wetting time of the probe tips, as well as map critical locations of light reflection and refraction in the tips. The facility consists of a vertically oriented traverse with a probe holder. Probes can be oriented to either travel into the quiescent fluid or out of the fluid and into the air. When the probe travels from the liquid into gas, the processes that it undergoes are similar to those when the probe strikes and pierces a bubble, with each incremental distance exposing the tip to more air, which must then dry. In the other orientation, the probe travels from the gas into the liquid, and is similar to the re-wetting of the probe when it exits a bubble.

Note that while the processes seen in the plunging facility are similar to bubble piercings, they are not exactly the same. A bubble’s curvature aids in maintaining its spherical shape, whereas a flat quiescent fluid interface does little to resist an initial deformation caused by anything touching that interface.

4.3 Instrumentation setup and synchronization

Synchronization of the high speed camera and oscilloscope was accomplished using a debounce latching switch that was calibrated and controlled as described below.

Calibration was carried out using a Coherent CUBE laser, capable of digital modulation up to 125 MHz with rise and fall times $< 3\ nsec$ and a high speed photo-detector. Referring to the diagram in Fig. 52, the laser light is directed to a piece of opaque paper with a pin hole in it. Equidistant on either side of the paper is the photo-detector and high speed camera. A portion of the laser light reflects off of the paper and is picked up by the camera, while the rest travels through the pin hole to the photo-detector. The photo-detector is connected to the oscilloscope.

Two primary components of the system were tested, the synchronization of the timing in the camera when compared to the oscilloscope and the delay from the digital trigger to the beginning of acquisition of the camera and oscilloscope. The delay was measured by triggering the camera and oscilloscope to begin collecting data at their maximum respective rates while the laser was triggered to start running after a short delay in a continuous state. Using this method, any internal trigger delays of the camera and oscilloscope could be quantified and measured. The synchronization was quantified by using the pulsing feature of the laser at a low power and high frequency while acquiring images and the signal from the photo-detector at the same frequency.

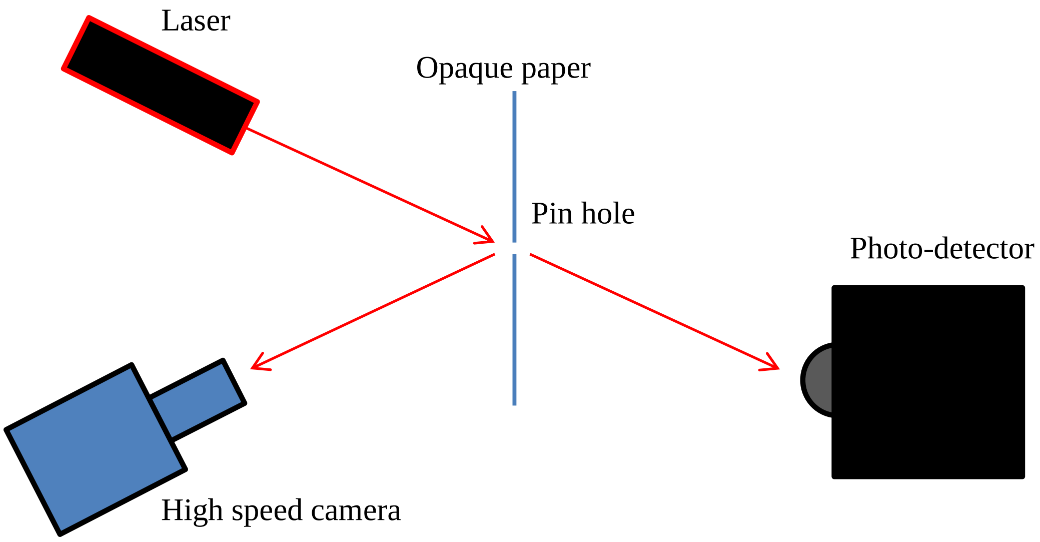

Figure 52: Configuration of high speed camera and oscilloscope synchronization

Over time, any drift in the signals can be quantified. Using these two methods, both the systems were synchronized to within the limits imposed by their maximum respective frequencies.

Triggering the camera and oscilloscope to capture bubbles was done in one of three ways; 1) continuous recording 2) bubble interface trigger and 3) bubble proximity trigger. With a continuous recording, the camera and oscilloscope were set to continually record data, while not a very efficient method; it does reveal grazes and small bubbles that would otherwise not set the trigger in methods 2 and 3. Bubble interface triggering is accomplished by latching the camera and oscilloscope triggers when the opto-electronic unit begins to register the rising signal of a bubble being pierced by the probe. This is useful in capturing re-wetting of the probe tips as well as viewing the deformation of the bubbles when pierced. A bubble proximity trigger uses a laser shining across the test section to a photo-detector, just prior to the probe tip. When a bubble crosses the laser line, it trips the photo-detector and triggers the camera and oscilloscope to start recording.

A sample of the probe tips tested is shown in Fig. 53. The tips are made in sapphire and are shaped in the methods described in §2.1.1. The compound angle tips (left and center, Fig. 53) are of the same design of probes used in the experimental campaigns in §2.3, with the center one

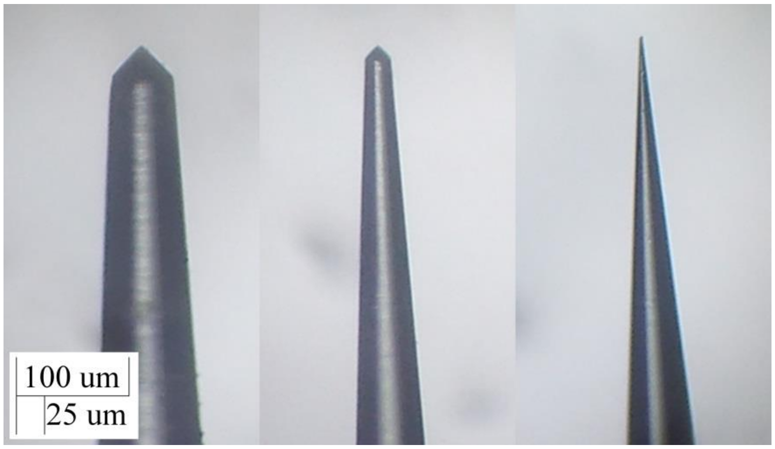

Figure 53: Probe tips tested, left to right: 54 μm tip (Probe 2), 22 μm (Probe 1) and straight taper (Probe 3)

being a probe that was used in the experiments. The single taper is more recent, described in §3.4 and has an ideal shape for piercing bubbles with minimal intrusiveness.

4.4 Test loop experiments

Experiments were conducted to ascertain the accuracies and errors associated with the operation of compound angle dual tip probes in a water/air two phase flow. The limitations posed by the small size of the probe tip, and the necessity to properly discretize the very tip of the probe limited the maximum velocity that can be used in the test loop. In order to resolve at least three points along the $45°$ taper of a $20\ \mu m$ dual angle probe tip, imaging needs to be conducted at a rate of $300\ kHz$ per m/s of bubble velocity, which exceeded the range of the high speed camera. Due to this, the primary experiments were conducted with bubble velocities around $30-40\ cm/s$, which allow frame rates of $60\ kHz$, to finely discretize the $45°$ tip of the dual angle tip. Additional experiments were conducted at higher velocities and lower frame rates to analyze the extent of bubble deformation in the entire piercing process.

4.4.1 Direct bubble piercings

Direct bubble piercings are broadly defined as bubbles being pierced with the probe tip relatively normal to the interphase of the bubble. In this configuration, the drying and re-wetting of the probe tip occurs evenly around the perimeter of the tip, and hence provides a good benchmark to compare bubble grazes and non-normal bubble piercings. Additionally, with the tip normal to the bubble interface, the exposed area of the tip is minimized as the bubble advances up the probe.

Figure 54 shows the piercing process of a compound angle probe (note that the images are not at equal time intervals), and in Fig. 55 the exiting process is shown. The corresponding signal measured during these processes is shown in Fig. 56, along with the phase indicator function, Eq. 10, using the double threshold of §1.5.1. Colored dots indicate when each image was taken. The red dots in Fig. 56 (middle) correspond to the images in Fig. 54. The blue dots in Fig. 56 (bottom) corresponds to the images in Fig. 55. The bubble being pierced is $\sim 750\ \mu m$ in diameter and the probe tip measures $22\ \mu m$ in diameter where the $45°$ section meets the $5°$ taper (Fig. 53, center).

Referring to Fig. 54, the first image in row 1 is taken $50\ \mu s$ before the interface of the bubble meets the probe, which occurs in the second image. The next ten images are taken $16\,2/3\ \mu s$ apart with the first 6-7 corresponding to the $45°$ tip drying. The subsequent images (row 3, image 4 through row 4) show the continued piercing of the tapered part of the tip. In row 1, images 3 and 4, a clear meniscus can be seen forming around the perimeter of the probe tip. The meniscus is no longer visible in subsequent images due to the deformation of the bubble, which prevents the viewing of the bubble/probe interface. During the piercing, the degree of bubble deformation is clearly visible in rows $2-4$. The bluntness of the probe tip combined with the low bubble velocity makes the surface of the bubble deform inwards as the probe tip exerts force on the bubble interface. The dimple that is formed around the probe tip grows for the earlier part of the piercing process and then stabilizes at a diameter of $\sim 150\ \mu m$.

Since the $45°$ tip of the probe is vastly more sensitive in terms of the ability to directly reflect light per given length, it shows minimal error in detecting the beginning and end of the bubble's interface. An analysis of the images and signal, shows that using the $10/90$ double threshold (§1.5.1) yields minimal error in the resident time of the probe tip in air, so long as the threshold levels are met. The conditions in which the thresholds are not met results in a bubble rejection. To mitigate rejection rates, a proposed methodology is presented in § 4.7. The associated relative error for the $10/90$ double threshold is less than 0.7% of the total residence time of the bubble. Using a more robust $20/80$ double threshold increases the error to $\sim 1.3\%$ and with a $50/50$ single threshold, the error increases to $\sim 6\%$. Since this is a relative error, as the resident time decreases (smaller or faster bubbles), the error will increase. This error corresponds to the drying time of the probe tip and is discussed in greater detail in §4.5.

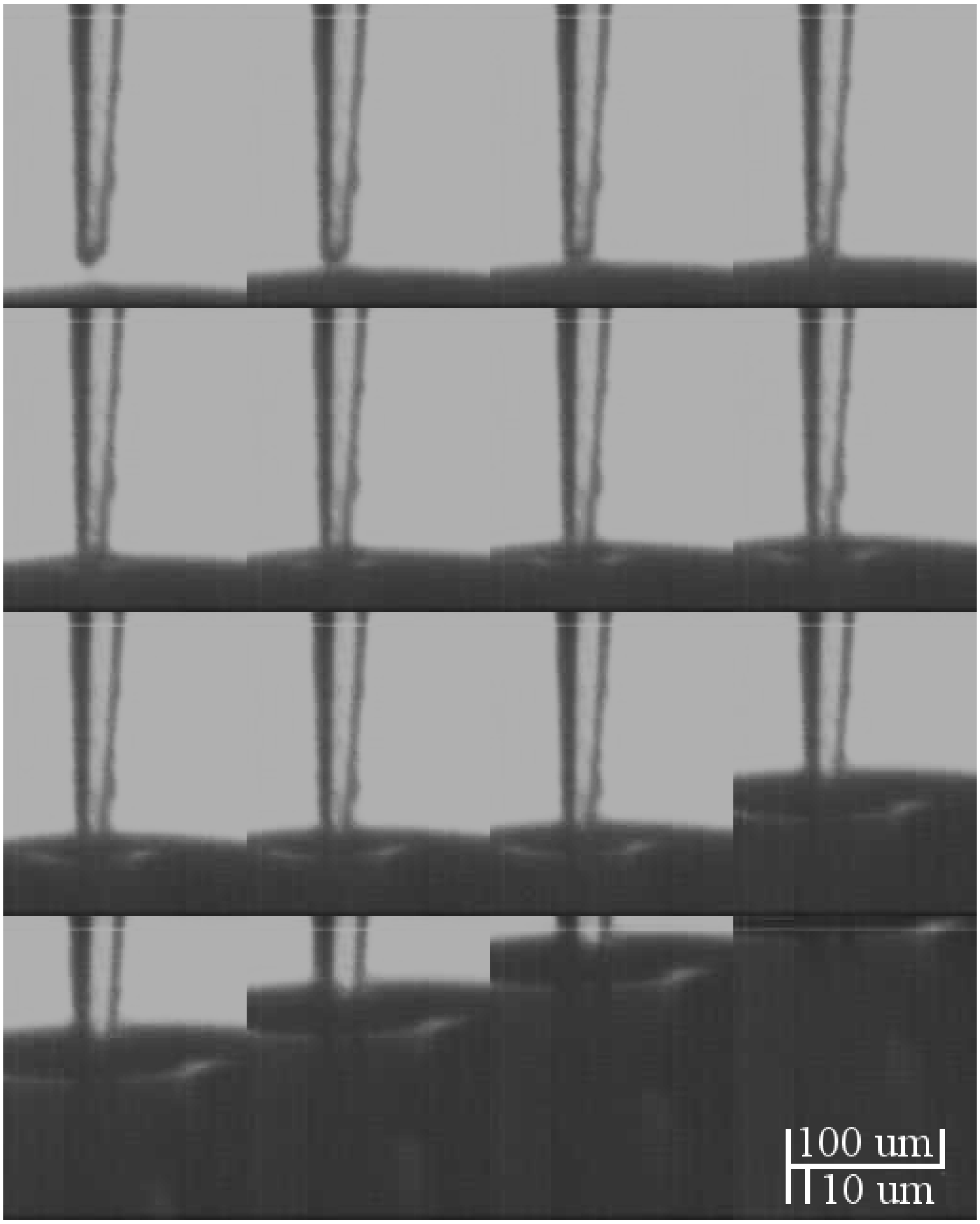

Figure 54: Piercing (de-wetting/drying) process of double angle probe tip (note that image sequence is not at equal time intervals)

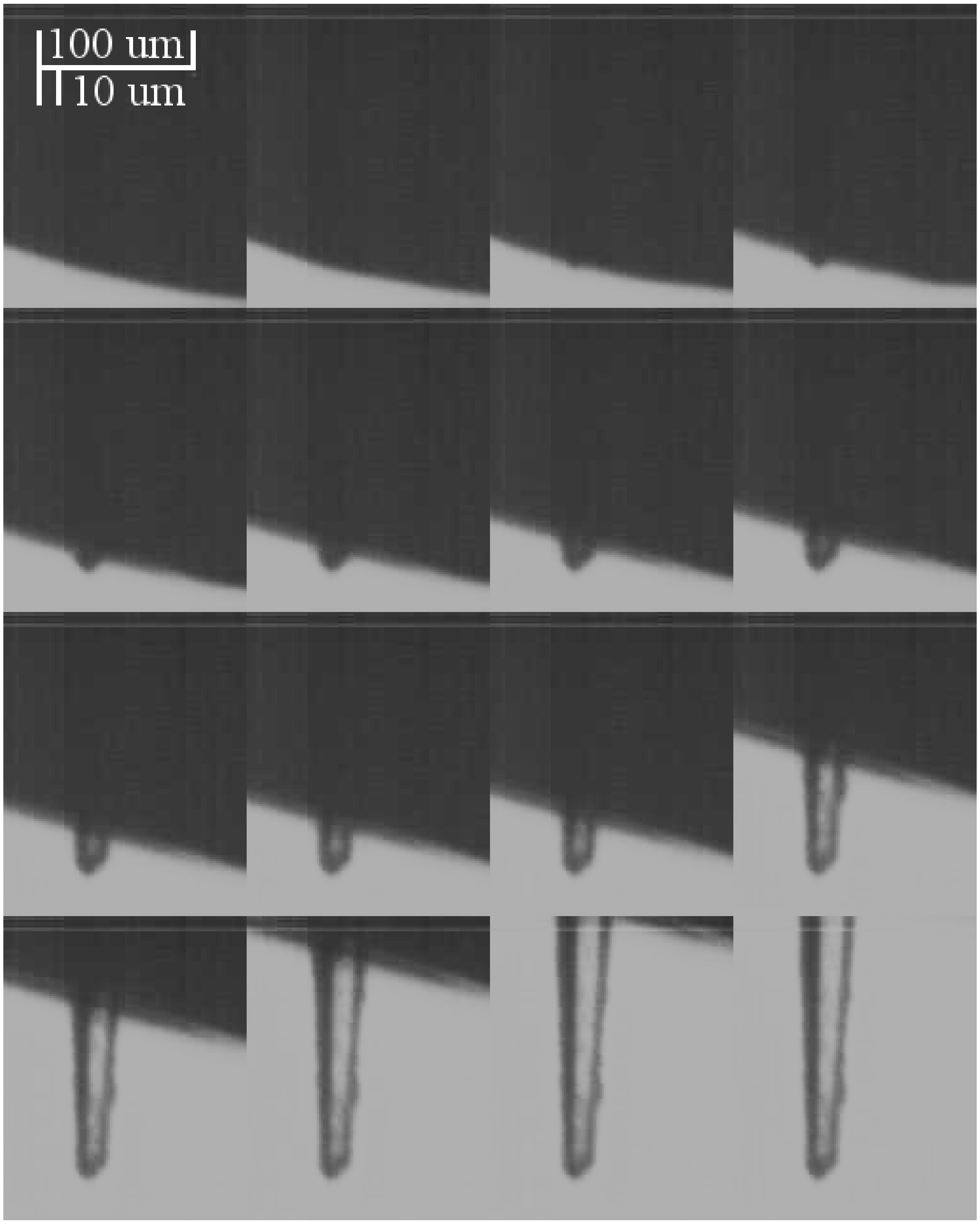

Figure 55: Exiting (wetting) bubble process (note that image sequence is not at equal time intervals)

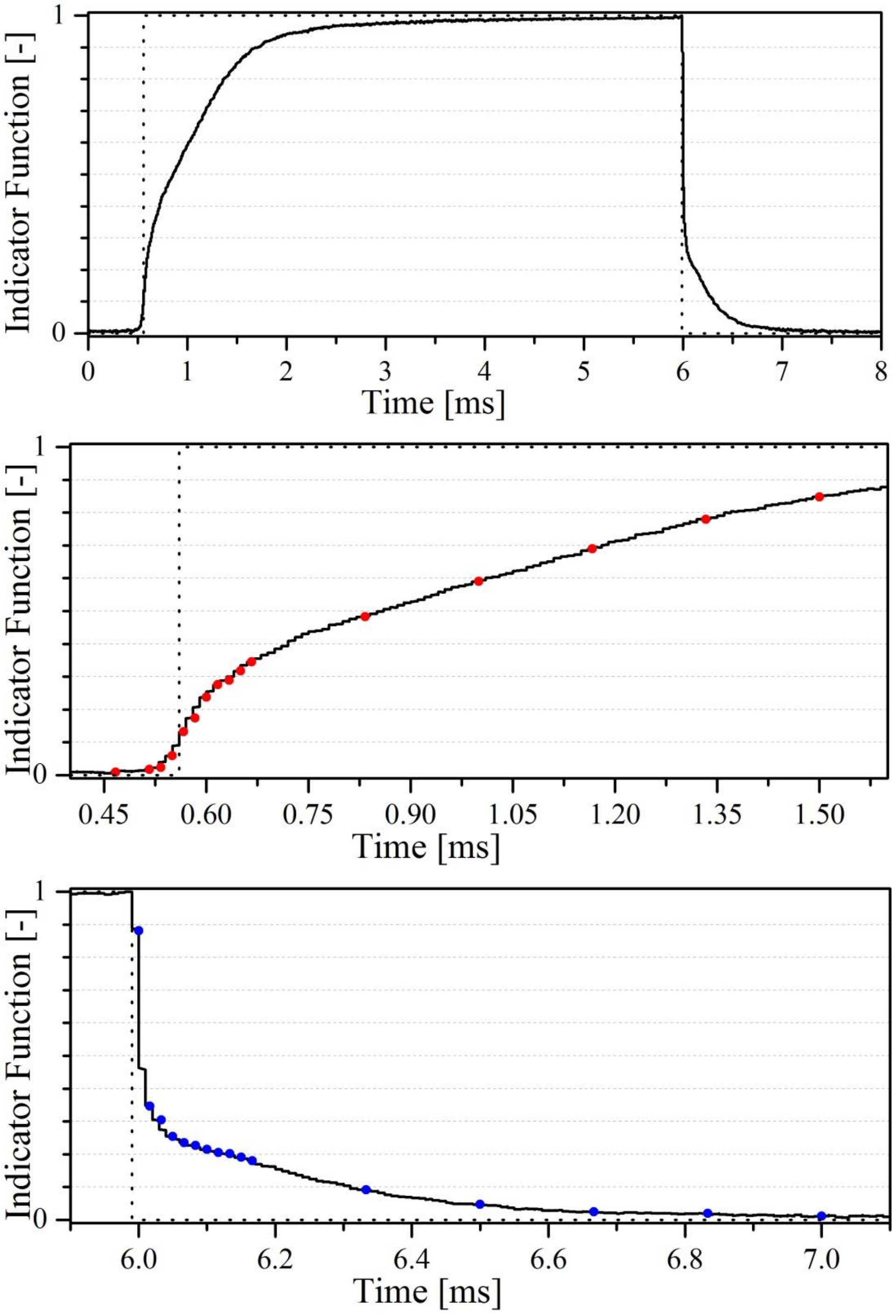

Figure 56: Normalized double angle full analog signal and corresponding phase indicator function

A similar experiment was run at a flow velocity of $2\,m/s$ to ascertain the degree of global deformation that a bubble will experience when pierced by both tips of a probe. Figure 57 shows the bubble piercing and the corresponding signal and indicator function. The bubble measures $700\ \mu m$ in diameter and the probe tip-tip distance is $525\ \mu m$. Note that in the analog signal, the second tip does not display the same drying curve as the first tip. This is primarily due to the second tip being slightly larger than the first, and since the exposed area increases with the radius squared, the second tip is more sensitive and hence rises quicker, this is discussed in greater detail in §4.5.2

Throughout the piercing process, the bubble maintains a relatively spherical shape and

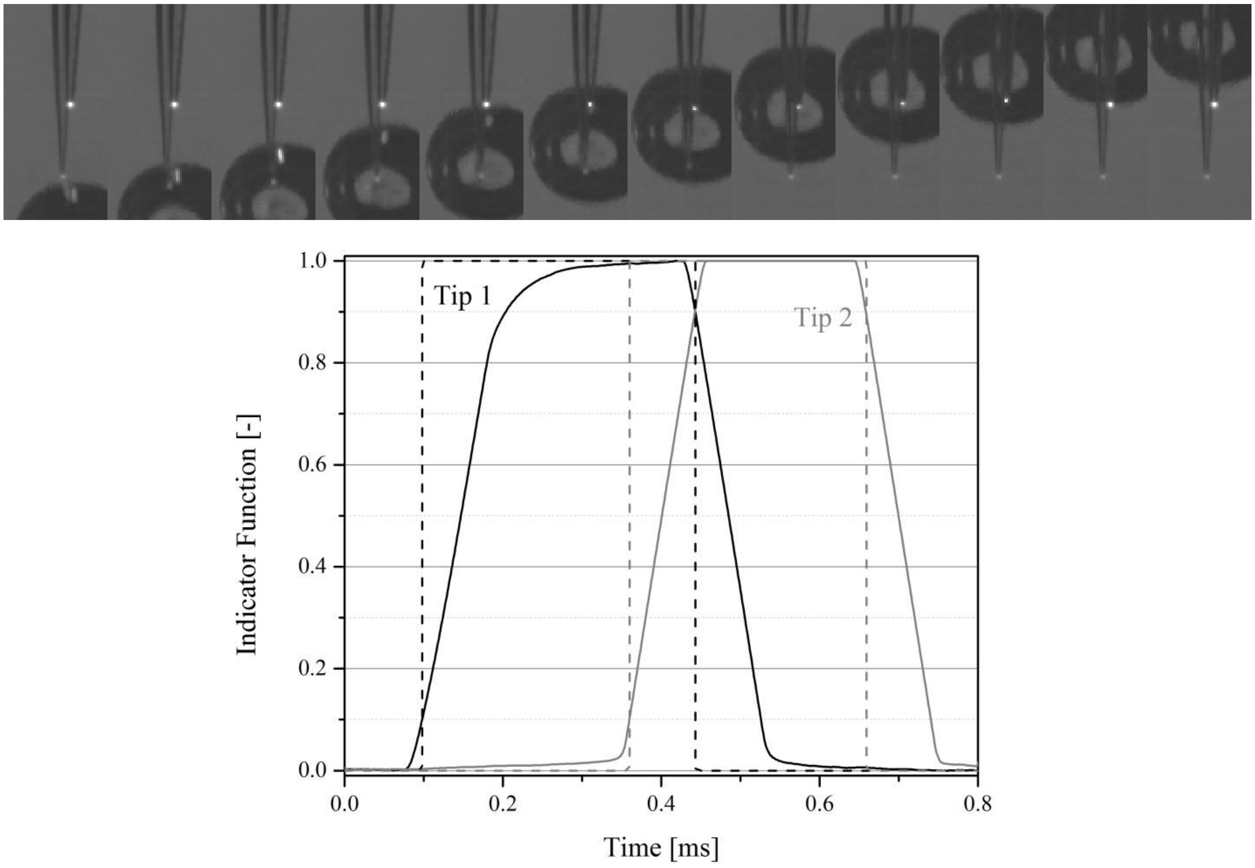

Figure 57: Compound angle double tip probe piercing with analog signals and corresponding phase indicator functions

shows minimal deformation up to the piercing with the second tip. As the bubble continues up the probe, it starts to deform slightly by elongating along the perpendicular plane to the probe axis. The elongation is caused by a slowing of the leading edge of the bubble as it encounters the continually expanding probe taper. Fluid from behind the bubble continues to push the bubble against the probe and has the effect of squishing the bubble. This causes a slight decrease in the second tips resident time in air. Additionally, as the two interphases of the bubble are in effect moving towards each other, the time-of-flight velocity is more accurate from the leading edges, as discussed in §2.1. The dimple that is evident in Figure 54 can be seen as a slight flattening of the otherwise circular curve that depicts the outline of the bubble. This dimple is most pronounced when the bubble meets the second tip. During the duration of the piercing process of the bubble, the bubble shows negligible amount velocity changes.

Due to the high magnification necessary to view the probe tips, and consequently the limited depth of field, imaging from higher velocities was not productive. The probe tips have a tendency to drift in and out of the plane of focus.

4.4.2 Bubble grazes

Bubble grazes and non-normal piercings occur when a bubble strikes the probe tip on the outer fringes of the bubble. Bubble grazes create vastly different behavior depending on the angle of contact and where the probe strikes the bubble surface. This can pose challes when processing the raw probe signal, as often a graze generates spurious signals that are similar to that of a small bubble. In other instances, bubbles will be deflected away from the probe tip and will not register.

An example of a bubble graze/non-normal piercing is shown in Fig. 58. In this instance, the bubble reflects sufficient light to be detected in the analog signal and goes above the first threshold, but does not reach the second threshold and hence was not be registered in the digital signal. Another consideration of non-normal piercings is that if the incident angle of the bubble is similar to that of the probe facet closest to the bubble, the bubble interface can reflect light originating from the tip, even though it's not in contact with the tip. The reflected light is then picked up by the probe and registers the bubble prior to its arrival. This is observed in the bubble pierced in Fig. 58 and results in the signal reach 10% prior to the probe tip making contact with the bubble. Note that due to the absorption of water in the near infrared to mid-infrared spectrum increasing substantially, there is negligible error associated with this detection and hence, it is not considered as a influential factor in §2.1.7.

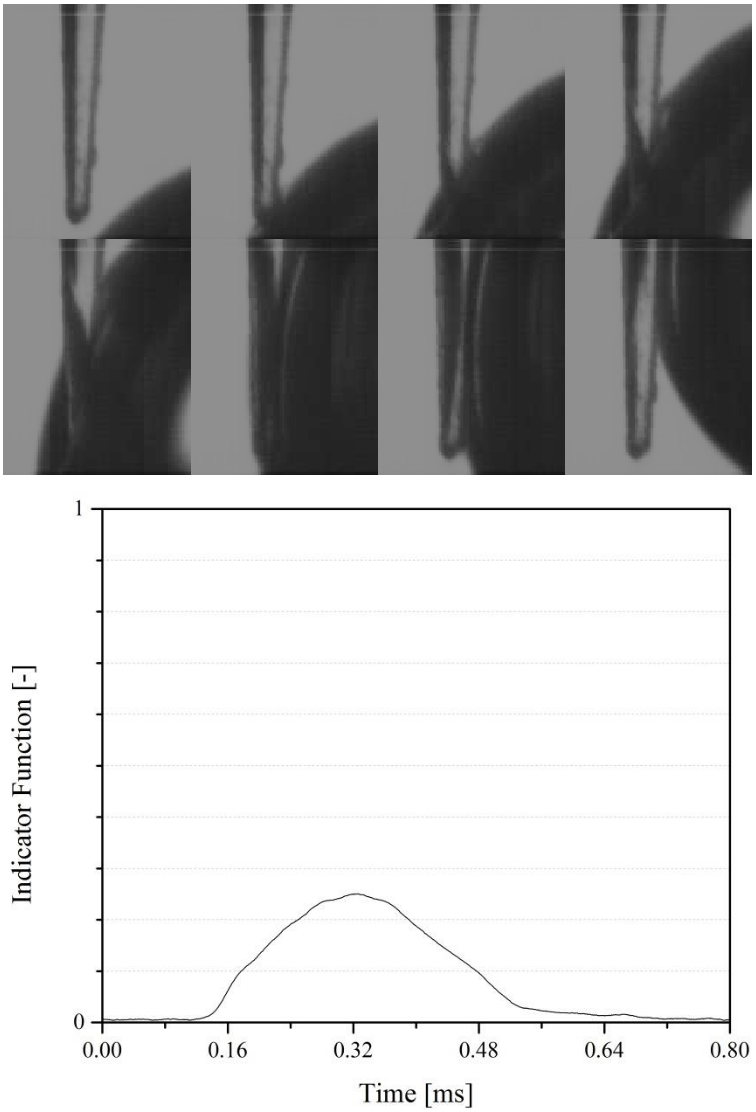

Figure 58: Bubble graze and corresponding analog signal

4.5 Plunging facility tests

To quantify the drying and wetting times and distances of the compound angle probes, the plunging facility was used with the probes shown in Fig. 53. To facilitate discussion, Probe 1 refers to the probe in Fig. 53, center, and is a probe that was built and used, among others, in the experimental campaigns in §2.3. Probe 2 (Fig. 53, left) was made with the 45° taper slightly above the upper limits of what was considered acceptable to use in the experimental campaigns. The third probe, Probe 3 (Fig. 53, right), was made with a single taper that matches Probes 1 and 2, but with no 45° tip. Probe 3 was made to evaluate traits in the signal observed in §4.4. The results of these experiments are shown below for each probe with a discussion on the finding and the related implications in §4.5.4. As Probe 1 is a combination of Probes 2 and 3, it is adequate to introduce the probes in a 3-2-1 order.

Experiments were conducted with the three probes using both configurations of the plunging facility, from gas (air) to liquid (water) and liquid to gas. A variety of velocities were used in the plunging tests ranging from $0.1 - 500\ mm/s$ to evaluate any velocity dependencies. The raw analog signal was collected along with high speed images. From the analog signal the tip-to-interface distance, which is the distance from the probe's tip to the liquid/gas interface is computed using the velocity of the plunging facility. There is a distinct difference between the active length of a probe tip and the interface distance. The extent of the interface distance that sees a changing signal corresponds to the active region of the probe tip. The critical component of this region is the length that corresponds to where the signal reaches the second threshold and is what is considered the active length.

4.5.1 Probe 3 results

Figure 59 shows the raw analog output signal (top left and right) and tip-to-interface distance (bottom) for Probe 3 going from liquid to gas. The output signal is shown on two scales to better separate the signals from the higher velocities. Signals for the three highest velocities

(100, 150 and 300 mm/s) exhibit some overshoot with minimal ringing. The overshoot quickly levels off before reaching an asymptotic value that is below the saturation point of the photodetector. An evaluation of the tip-to-interface distance shows that the active region of the single taper is independent of the relative velocity between the interface and probe tip. The linear range of the active area is longer than that predicted by the light tracing program of §3.4, which is consistent with the findings of Cartellier and Barrau (1998). This is primary due to the assumption that all light entering the probe tip is traveling in a direction parallel to the axis of the

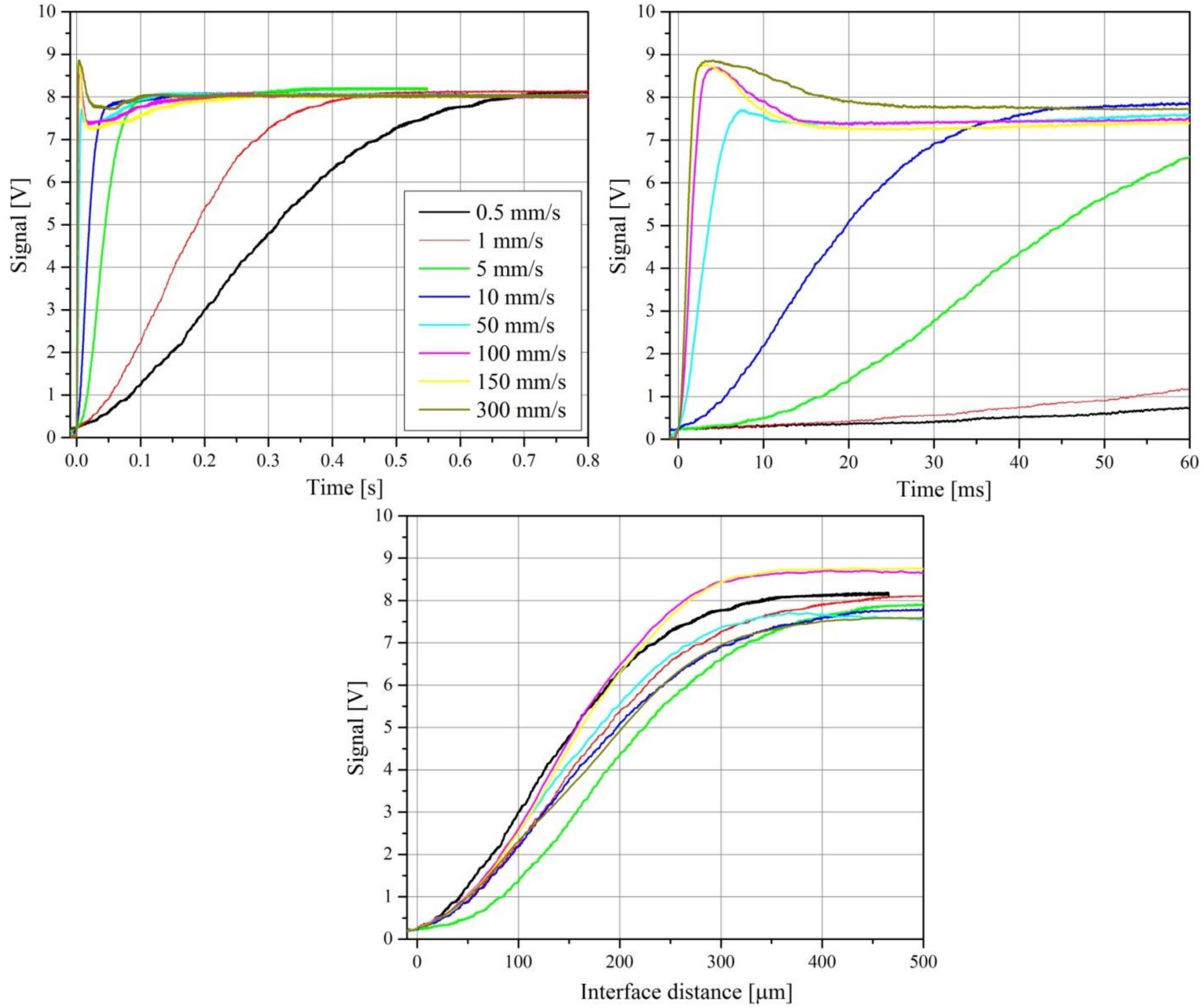

Figure 59: Probe 3 de-wetting/drying signals (top row) and interface distance

fiber. As the incident angle of light increases the location where i_c is reached moves axially further from the probes' tip. The effect of this is similar to having a larger taper angle where the number of reflections required to meet i_c decreases and hence increases the active length of the probe. In a multi-mode fiber optic cable the light bounces within the fiber when there is a bend in the cable or if the source is not perfectly collimated. In effect, the light entering the probe tip to not be parallel to it and causes the active length of the tip to be longer than predicted. Another factor source that contributes to the active length being longer than predicted is the actual drying time which has been studied by Zun *et al.* (1995). This is the finite amount of time that is required for the water film to dry off of the probe tip. The drying time can be evaluated by comparing the wetting signals, which is known to be in effect instantaneous.

Figure 60 shows the wetting (gas-to-liquid) signals and tip-to-interface distance of Probe 3. Similar to the drying experiments, the wetting shows an increase in active length over that predicted in §3.4 and a nearly linear trend over the middle 50% of tip length.

Comparing the wetting distances and the drying distances verifies the conclusions of Abuaf *et al.* (1978); the drying time is proportional to a constant divided by the velocity (Eq. 33). The constant is not the same for the drying as it is for the wetting, with the drying constant being larger than the wetting by $\sim 100\ \mu m$ with this probe shape. Due to the shape of this probe, the range of valid velocities increases over that found by Abuaf *et al.* (1978), namely in the lower velocity region, where surface tension effects increase relative to the inertial effects experienced at higher velocities. The deformations that the probe tip can cause are discussed in detail in §4.5.4.

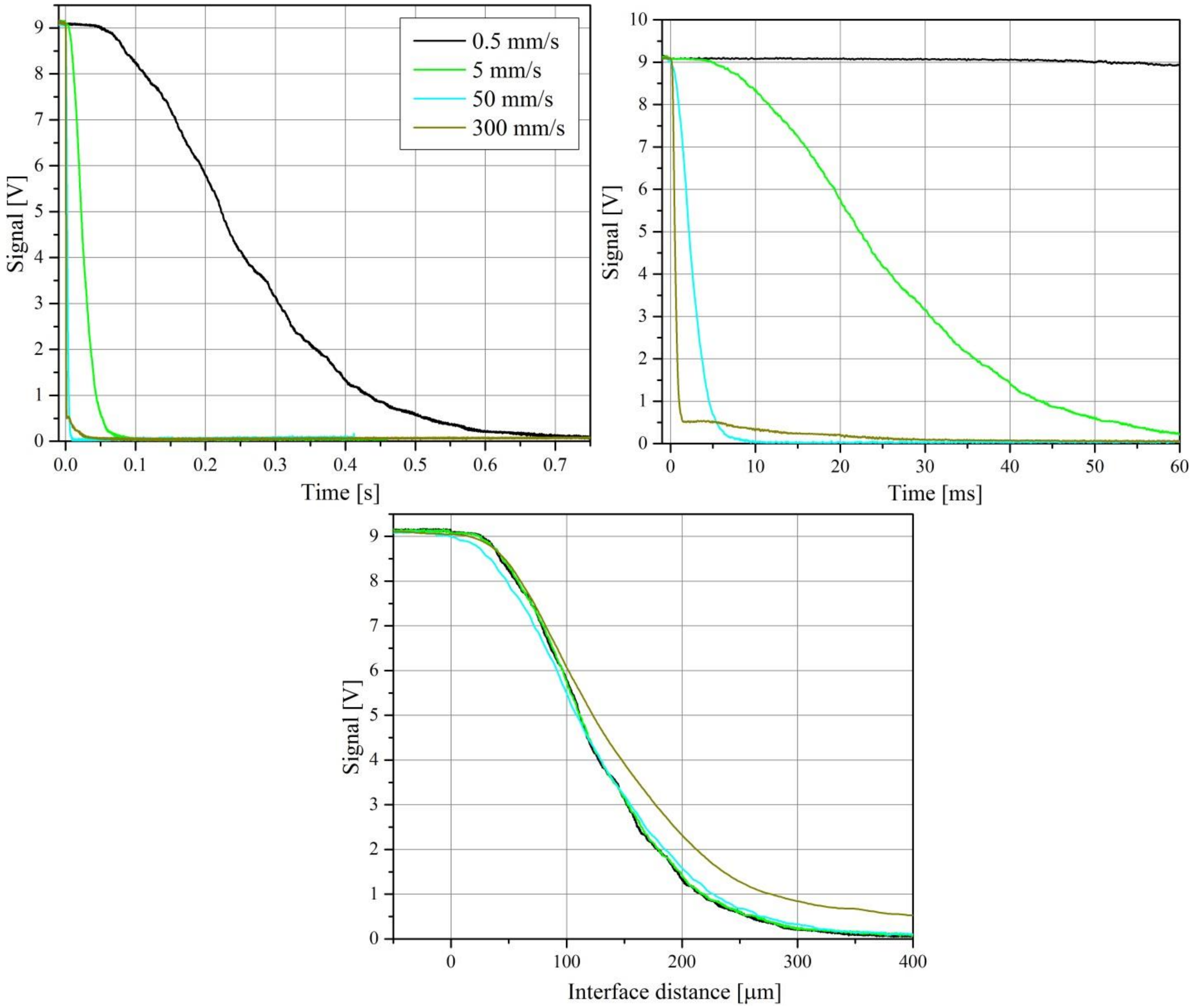

Figure 60: Probe 3 wetting signals (left) and interface distance (right)

4.5.2 Probe 2 results

Figures 61 and 62 show the drying and wetting signals and interface distances, respectively for Probe 2 with the same velocities and conditions as above. The proximity of the interface to the probe tip leads to reflections from the interface causing the probe to register some reflected light prior to piercing the interface. This becomes prevalent when the tip is approximately 25% of the tip diameter away from the interface (Fig. 61, bottom). On a probe tip of this size and greater, this is a non-negligible source of error, as the return signal reached prior to touching the interface can easily exceed the lower threshold values if not set correctly. With smaller probe tips (§ 4.5.3) and non-planer surfaces (bubbles), this error is expected to decrease. Smaller probe tips do not have sufficient aperture to pick up the reflected light. Additionally, with smaller probe tips, when they get close enough to the interface such that they could pick up on the reflected light, their proximity (which is estimated to be $4-5\ \mu m$ for Probe 1) would be on the order of the wavelength of the IR light and hence would not follow the continuum light

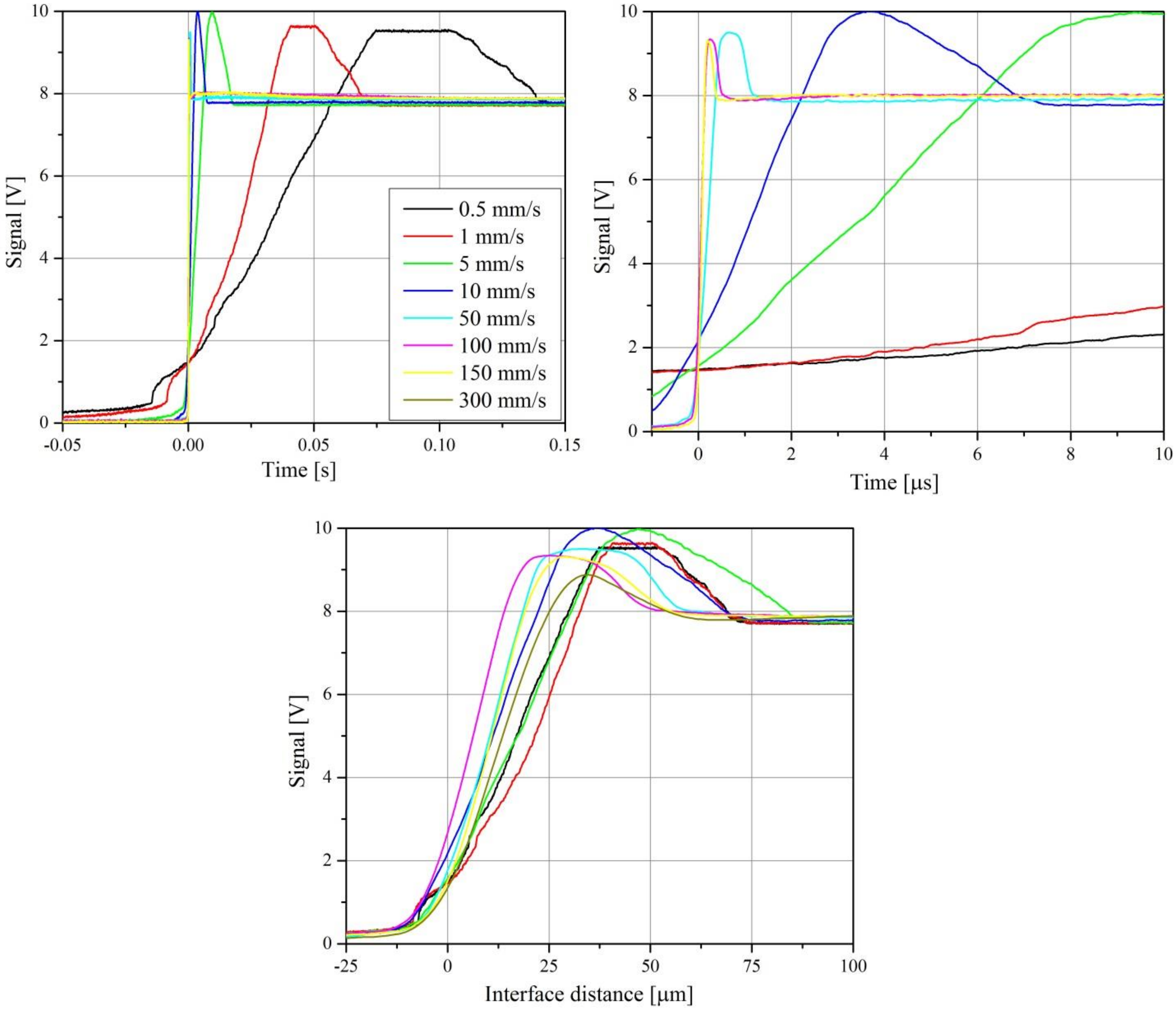

Figure 61: Probe 2 de-wetting/drying signals (top row) and interface distance

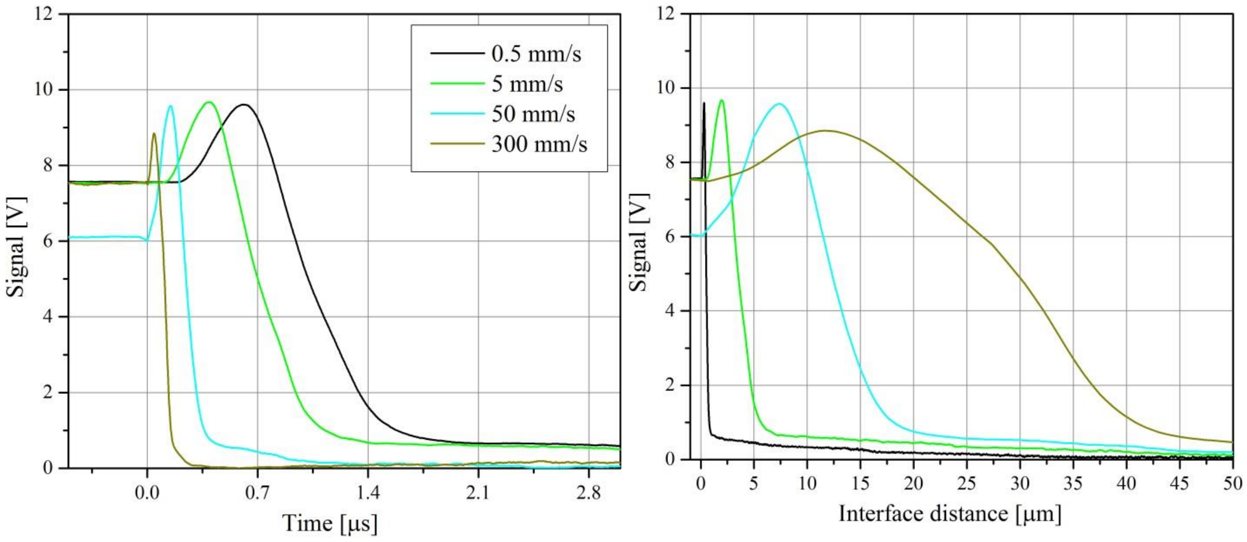

Figure 62: Probe 2 wetting signal and interface distance

assumption used for this analysis. Non-planar surfaces, such as bubbles, have the characteristic of scattering light rather than directly reflecting it as a planar surface does.

The overshoot that is observed in the signal has been observed by Abuaf *et al.* (1978) and more recently by Cartellier and Barrau (1998). Cartellier and Barrau (1998) suggest that this is an artifact of the local interface deformation occurring at the boundary of the conical and cylindrical portions of the probes (Fig. 42). Abuaf *et al.* (1978) suggested that what Miller and Mitchie (1969) had observed as a reduction in signal amplitude with increasing velocity is a result of a thin film of liquid that is present as the probe pierces an interface, and whose thickness is dependent on velocity (Fig. 63). The overshoot seen in Probe 2's signal is believed to be a combination of the two phenomena. As the interface deforms and is pushed by the probe tip, a thin film of water is captured between the probes' surface and the surrounding air. Due to the small size of the actual tip, this film acts on the surface to make it a reflective coating. As the coating dissipates with the probe traveling further into the gas, the reflectiveness decreases and sees the signal asymptote to its full scale amplitude. In the case of Abuaf *et al.* (1978), the thickness of this film is greater due to the size of the probe and does not have sufficient time to

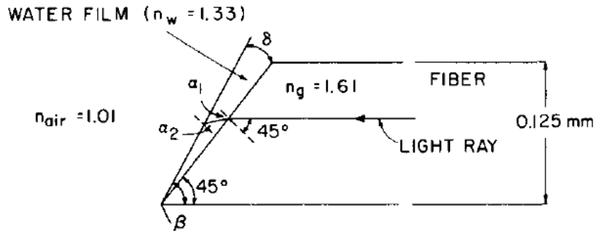

Figure 63: Sketch of 45° probe tip with water film. Taken from Abauf *et al.* (1978)

fully dry within the transit time of a bubble, and hence, the signal is truncated below the full amplitude.

The wetting signal of probe 2 has vastly different trends than those observed in Probe 3. The active length appears to be dependent on probe velocity. In all cases there is an increasing active length with probe velocity. At the highest velocities tested, the active length approaches that of the active length in the de-wetting process. An evaluation of the high speed camera reveals that there is significant capillary action that occurs at the lower velocities (See §4.5.4, Fig. 68), which is also described by Cartellier and Barrau (1998). As the velocity of the probe increases, the bluntness of the tip causes a significant deformation similar to that observed in Fig. 54. This deformation pushes the wetting location further up the probe and thus causes an increased effective active length.

4.5.3 Probe 1 results

The results for Probe 1 drying and wetting are shown in Figs. 64 and 65, respectively. The drying signal undergoes two distinct phases which are best observed in the interface distance (Fig. 64, bottom). The first phase is similar to Probe 2's signal and the second phase similar to Probe 3's signal. The first phase is defined by a greater rate of increase in the signal, while the second phase has a smaller, but still positive, rate of increase. These two sections are similar to the dual angle single tip probe described in §3.2, and indeed, the derivative of the signal seen in

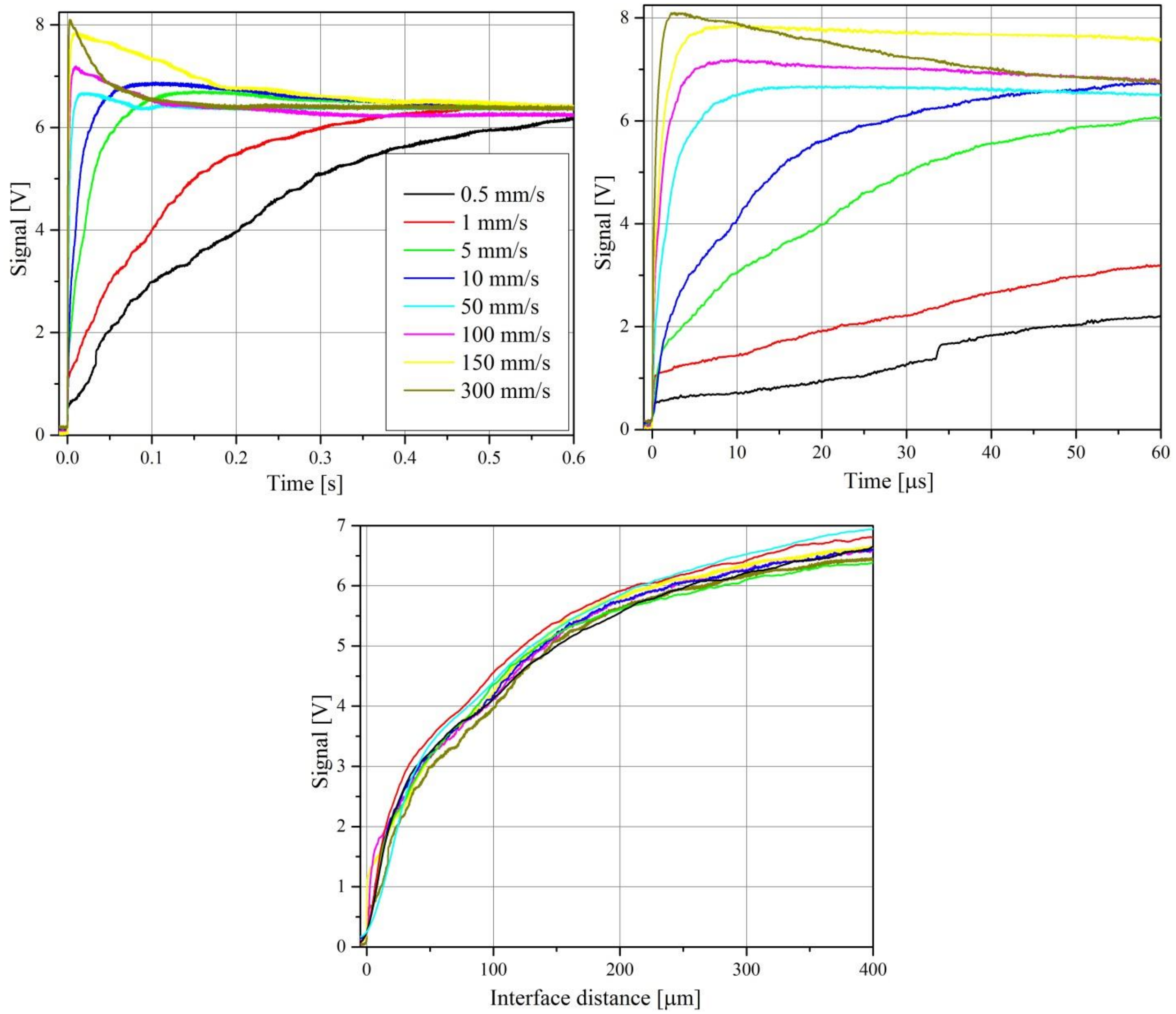

Figure 64: Probe 1 de-wetting/drying signals (top row) and interface distance

Fig. 65 shows a similar trend. The overshoot observed in Probes 2 and 3 are prevalent in Probe 1's signal as well.

The wetting signal displays a number of interesting characteristics. When the proximity of the probe to the interface is close the signal is seen to decrease. It is believed that the tip acts as a hygrometer similar to the fiber optic hygrometer described in Trainer (2000). The reason the smaller probe tip is more sensitive to the liquid vapor in the gas when compared to the larger probe tip of Probe 2 is not fully understood. Following the slow decrease in signal, the liquid

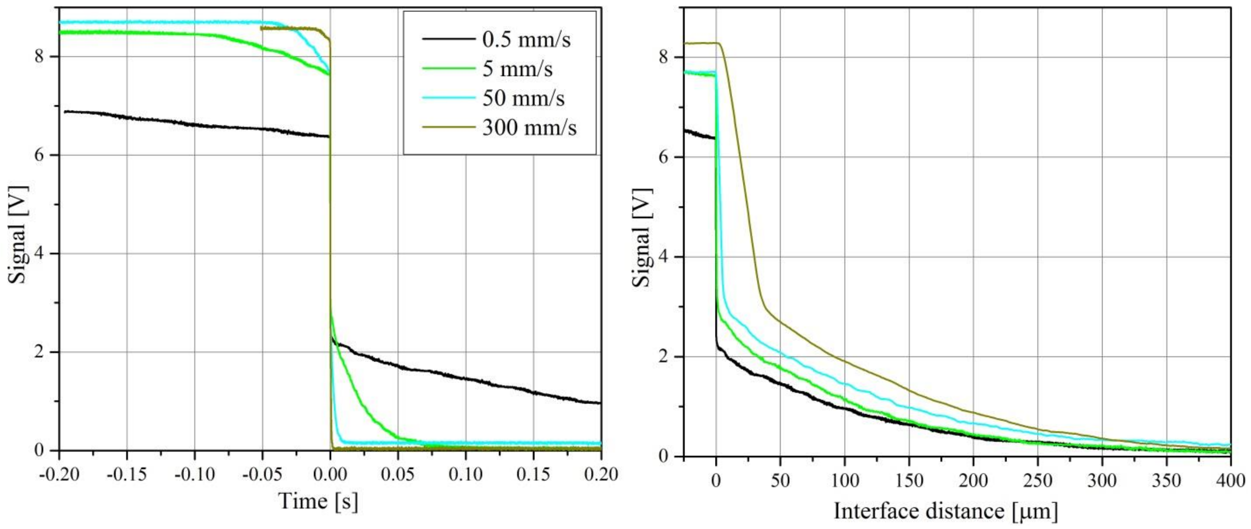

Figure 65: Probe 1 wetting signal and interface distance

interface is reached and a quick capillary action saturates the $45°$ portion of the tip with liquid causing a sharp decrease in the signal. The signal continues to decrease reaching a steady state amplitude of 0 after approximately $3 - 400\ \mu m$.

4.5.4 Discussion of plunging tests

During the drying process, the distance that each probe must travel to reach the critical threshold value is fairly independent of velocity, see §4.5.1-4.5.3. The images shown in Fig. 66 are for a velocity of $0.5\ mm/s$, but can serve to represent the full velocity range of the plunging tests conducted. The images correspond to the time when the probe's signal reached $10/50/90\%$ threshold values. With all three probes, the signal continues to grow beyond the 90% threshold until each probe's steady state voltage is reached.

Note that with Probe 2, the interface surge observed by Cartellier and Barrau (1998) is present. The surge, is explained by the inertia of the fluid pushing the interface up as the probe tip approaches. The surge is more pronounced with a flat interface than with a curved one (as would be expected with a bubble piercing). This allows for the probe tip to advance beyond the quiescent interface level prior to the actual tip penetration. With the smaller cross sectional areas of Probes 1 and 3, this surge is not as well defined in the images.

It can clearly be seen that probe 3 needs more penetration length to reach all threshold values. The images also show similar surface deformation as seen with Probe 1 when the 90% threshold is met. The increased active length (to reach the 10% threshold with Probe3) makes the interface deformation significant when compared to Probes 1 and 2 at the same threshold level. At the 90% threshold, both Probes 1 and 3 show similar surface deformation. While it is expected that the sharp taper of Probe 3 would better penetrate an interface, the necessity for an increased penetration length negates any benefits that are gained by the sharp taper. With Probe 1, the distance that is traveled from the 10% threshold to the 50% is $\sim 43\ \mu m$ with an additional $\sim 95\ \mu m$ traveled to reach the 90% threshold.

Figures 67 and 68 show time series images of the gas-to-liquid transition for $0.5\ mm/s$ and $300\ mm/s$, respectively. The capillary action that causes the sharp decrease in the probe signal as it reaches the interface at lower velocities in Probes 1 and 2, observed in §4.5.2 and 4.5.3, is clearly visible in Fig. 67. Between $d_O + 1\ \mu m$ and $d_O + 2\ \mu m$, which represents a $1\ \mu m$ increment distance between of the probe tip and the interface, the interface is seen to jump up the probe tip in excess of $25\ \mu m$. Probe 3 is observed to have nearly no effect on the interface at this same location. As the probes continue into the interface, the capillary action continues to draw the fluid up the perimeter of the probe tips. This continues until the interface reaches the location where the fiber diameter is approximately $60\ \mu m$, beyond which there is minimal interface deformation.

The column of $d_O + 48\ \mu m$ in Fig. 67 corresponds with the same location below the interface as $d_O + 48\ \mu m$ in Fig. 68 and serves as a good metric to see the effect that the probes velocity has on the interface. The deformation in the interface due to inertial effects is quite noticeable and in stark contrast with the capillary action pulling the interface up the probes in Fig. 67. At this velocity the deformation continues to grow throughout the piercing process until well after the 5° taper transitions into the cylindrical root fiber. In the case of a dual tip probe made of tips similar to that of Probe 1, the deformation would be expected to continue growing, or in the case of a bubble piercing, the bubble tends to break apart or get pulled to one side when the structure of the probe is met.

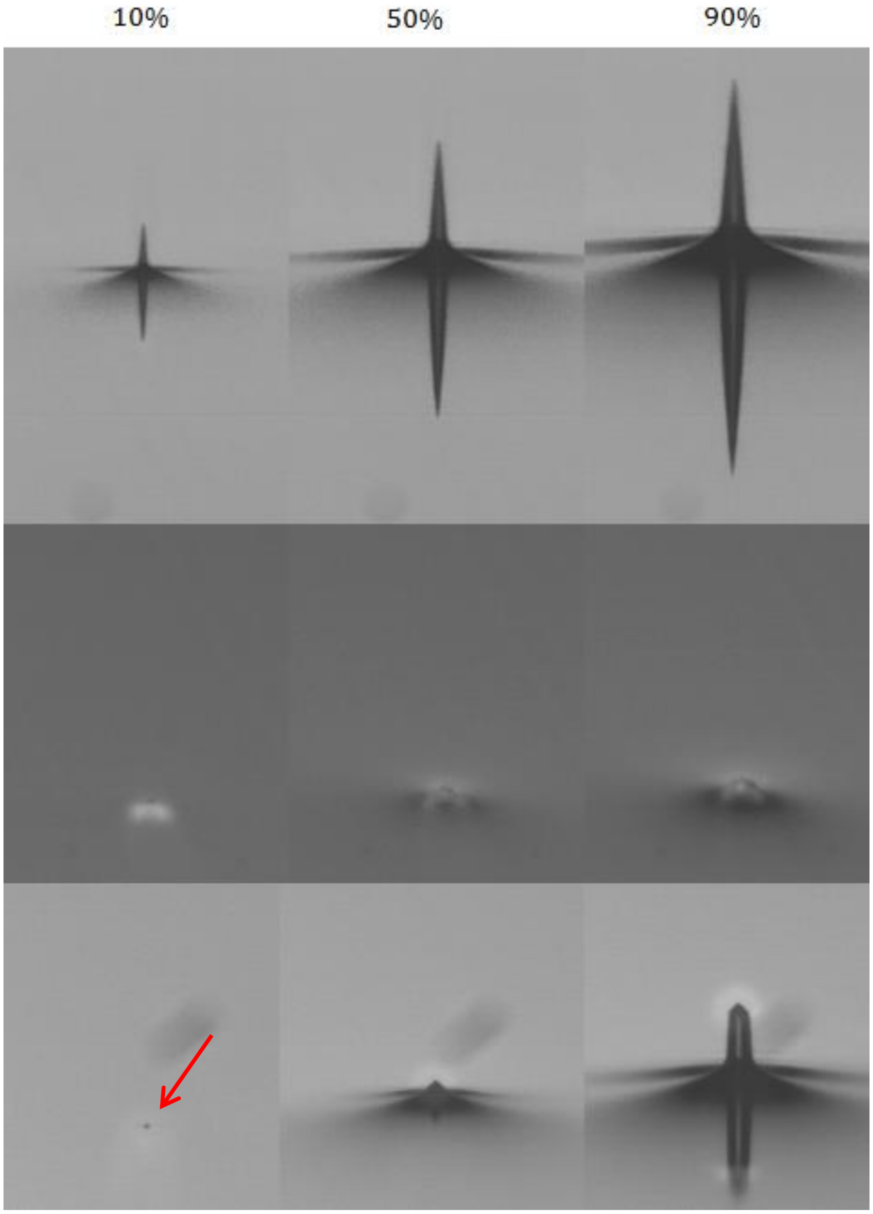

Figure 66: Probe tip images at threshold values for liquid-to-gas transition. From top to bottom, Probes 3, 2 and 1

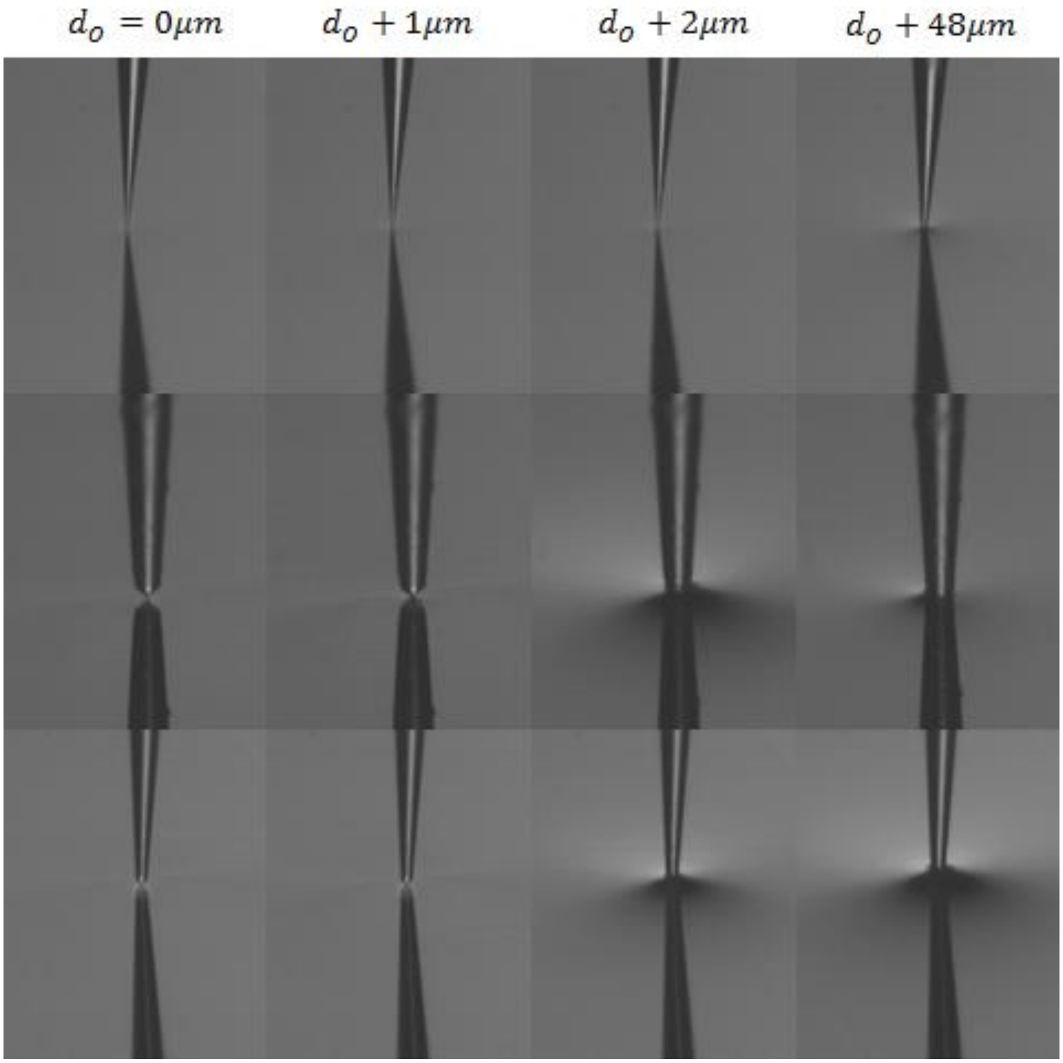

Figure 67: Time series of images from gas-to-liquid transition for 0.5 mm/s. From top to bottom, Probes 3, 2 and 1

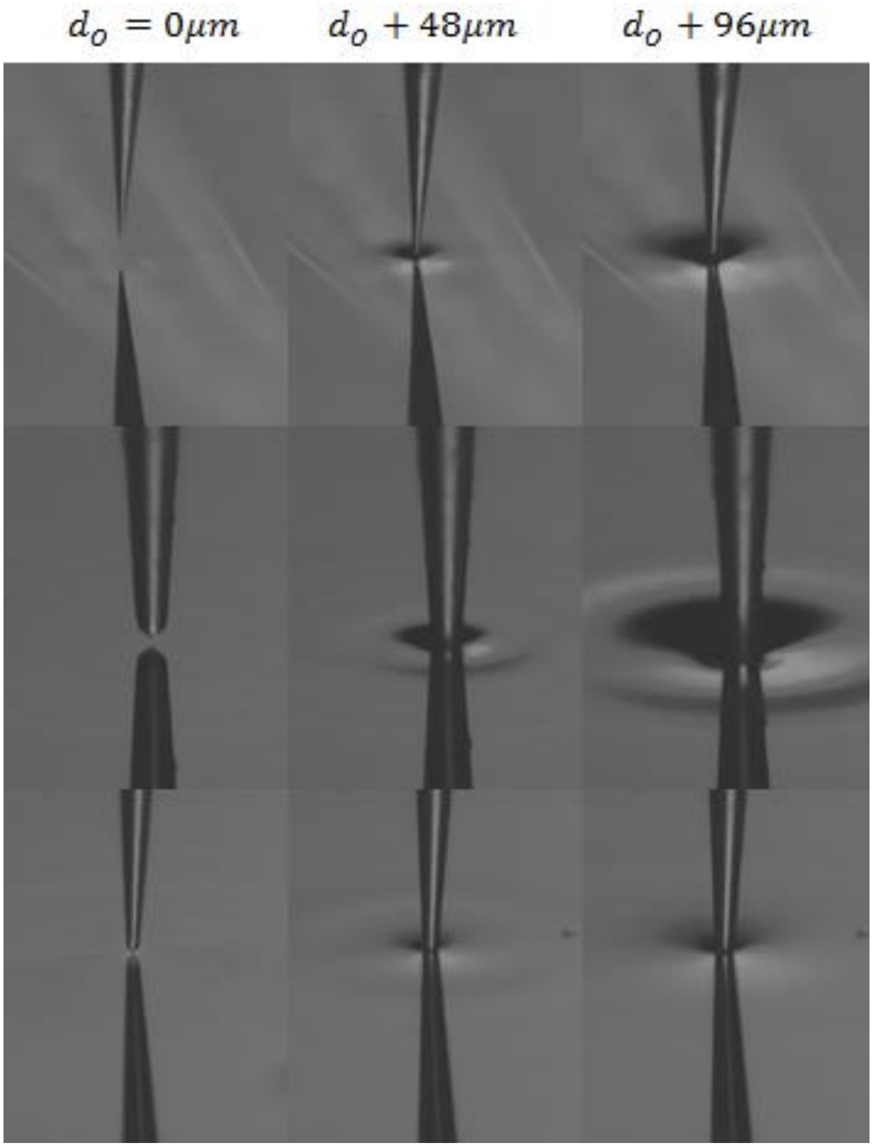

Figure 68: Time series of images from gas-to-liquid for 300 mm/s. From top to bottom, Probes 3, 2 and 1

4.6 Discussion on tip characterization

The characterization of the probe tips revealed some noteworthy aspects:

- There is a critical active length necessary to reach the second threshold with a double threshold technique. Ultimately it is not the tip size, but the critical active length that determines the lower bound on the size of bubble that can be measured.

- The active length can be controlled by taper angles and by the 45° tip size. Counterintuitively, a decrease in the active length can be accomplished by increasing the 45° tip size with diminishing returns once the second threshold is met in the length of the 45° tip.
- The extent of bubble deformation, both globally and locally is minimal in the test loop experiments, suggesting that there is minimal deformation error associated with the piercing process.
- The active length for the drying of the probe tips appear to be constant for any given shape, whereas the wetting active lengths appear to be velocity dependent.
- To reduce small bubble rejection rates, an improved threshold technique needs to be developed. A suggested method is described in § 4.7.

4.7 Differential threshold processing method

In an effort to reduce bubble rejection rates associated with small bubbles and bubble grazes, a new processing methodology is proposed below. The methodology relies on being able to detect the slope of the drying and wetting signals. Using a similar threshold technique to the current double threshold, the spikes in the slope can be used to mark the times of the bubbles interface crossing the probe tip. This method is similar to that used in §3.2 and §3.3.

Computing the derivatives can be done in a number of different ways. The brute force method is to compute the derivative at the software level, which requires the entire analog signal to be digitized in situ. While reliable and simple to implement, there are a number of considerations when pursuing this method. The impact rates seen in high speed flows can approach 1,000 bubbles/s or more (§ 2.3.3) and would be expected to increase as smaller bubbles are detectable, making saving the entire signal for off-line inefficient. Using a minimum bubble size of 50 μm and a flow velocity of 10 m/s, the time in air is 5 μs. This imposes a minimum response time necessary to detect rise times that are expected to be on the order of 200 ns. This, combined with the Nyquist rate to acquire alias-free signals would require the use of specialized high speed hardware to be able to differentiate the signal at the software level in real time. While not out of the range of contemporary Field Programmable Gate Arrays (FPGAs) or fast microprocessors, a more clever and efficient solution is to use a simple differentiator circuit. The addition of a differentiator circuit to the current suit of electronics has the benefit of using the reliability and well proven comparator based digitizing components already in use and saves only the critical information necessary to generate the phase indicator function (Eq. 10).

4.7.1 Bubble rejection causes

There are a variety of scenarios that can interfere with the registration of bubbles in the double threshold technique currently used. Any chord length piercing that is shorter than the active length of the probe risks not reaching the upper threshold. These short cord lengths can be caused by small bubbles (see Fig. 13), by off center bubble piercings or by bubble grazes (as seen in Fig. 58). In the cases of small bubbles and off center piercings, the trailing edge of the bubble reaches the probe tip prior to the leading edge reaching the location of the upper threshold. In the case of bubble grazes, there is not sufficient contact of the bubbles interface with the active area of the probe tip to reach the upper threshold.

The rejection rates for the experimental campaigns conducted in §2.3 are not known, as analog signals were never collected and was beyond the scope of the project. It can be presumed that the rejection rates might be quite high, as many bubbles smaller than the active length of the probes used were present in the far wake of ships (Trevorrow *et al.*, 1994; Trevorrow *et al.* 2006; Vagle and Burch, 2004; Stanic *et al.*, 2009). In the context of this thesis, measuring the smallest bubbles possible was highly desirable and was the driving force behind the development of probes capable of piercing small bubbles. It is still necessary to develope an appropriate processing methodology and corresponding electronics.

4.7.2 Evaluation of drying and wetting signals

An evaluation of Fig. 69 reveals that the range in amplitudes of the derivatives from the signals acquired in §4.5 differ drastically for different probe sizes. Unlike the photodetector signals acquired, whose full scale amplitude is dependent on the light that is reflected and the photodetector sensor used, the derivative is highly dependent on the active lengths of various probe geometries and sizes.

Similar to the selection of the threshold levels in the signal double threshold method, the selection of the threshold levels in the differential threshold method requires some special considerations. In a typical signal, one would see the derivative spike to a positive value as the probe tip is drying and then to a negative value as the probe tip wets. The threshold values must be set at levels such that noise, which is amplified in the derivative, does not reach the trigger levels. Also, the thresholds must be set above the levels created by the overshoot observable in most signals (§ 4.5). With these considerations in mind, it is reasonable to assume that the threshold values would need to be set on a probe-by-probe base with some input based on the expected velocities.

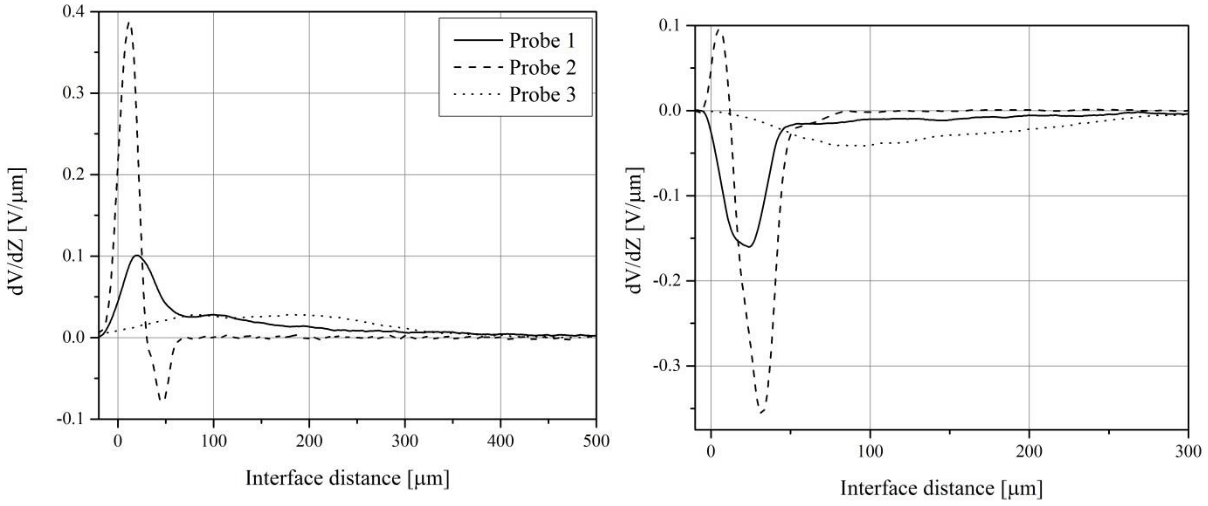

Figure 69: Derivative of drying (left) and wetting (right) signals for Probes 1, 2 and 3 at $300\ mm/s$

4.7.3 Processing method

Due to the nature of the derivative, the processing method is quite simple to understand and implement. With properly selected thresholds, each positive threshold reached will correspond with the leading edge of a bubble and each negative threshold will correspond to the trailing edge of a bubble. The logic implementation is as follows: transition of threshold from zero to positive, time stamp-indicator 1; transition of threshold from zero to negative, time stamp – indicator 0.

4.7.4 Sample signals

A collection of sampled signals are presented below. These signals correspond to bubble piercings from the test loop (§ 4.4), where the analog signal has been acquired. For comparison purposes the signals are from bubble piercings already presented and have been processed at the software level. The threshold levels used to generate the phase indicator function were selected at $\pm 5{,}000\ V/s$.

The signal shown in Fig. 70 is from the bubble piercing in Fig. 57. The bubble pierced is greater than the active length of both tips in the dual tip probe. With the differential threshold method the detection of the leading edge of the bubble occurs $20\ \mu s$ earlier than the traditional double threshold method. The detection of the falling edge occurs $14.6\ \mu s$ earlier. The increase of $\sim 5\ \mu s$ in the residence time is a 1.6 % increase when compared to the double threshold, which decreases the error in the total residence time by $\sim 0.06\ \%$. The reduction in error is negligible, and shows that for bubbles of this size, both interface detection methods work equally well.

Applying the differential threshold method to the bubble graze of §4.4.2 yields the signal and indicator function seen in Fig. 71. Note that the signal generated by a bubble graze is extremely similar to that of a small bubble whose diameter is smaller than the active length. The similarities in the signals come from the active *region* of the probe tip. In the case of a bubble graze the bubbles interface is in contact with a large area of one side of the active region, see Fig. 58, row 2 images. A small bubble will occupy a similar area, but on the entire circumference of the probe tip. This can be seen in Fig. 13 (row 1, image 4) where the bubble has transitioned away from the active length, but still occupies the active region. The original signal did not reach the upper threshold in the traditional method, and hence was not registered in the digitized signal. Using the differential threshold, the bubble graze is easily detectable with a residence time of $228\,\mu s$. An analysis of the images captured in conjunction with the acquired signal results in the bubble having a residence time of $333 - 366\,\mu s$. The deviation of the differential threshold residence time from the true residence time in a bubble graze is largely explained by a combination of the interface deformation and imperfect internal reflection when most of one side of the probe tip is in contact with the bubble (see Fig. 58). Both the interface deformation and the one-sided strike create a lag in the response of the optical system which under-represents the true residence time. A bubble graze such as this one may or may not reach the second tip. In the case that it does, a similar signal is expected to be generated and a velocity and hence chord length can be computed. In the case of the bubble not reaching the second tip, the bubble will only factor into the void fraction measurements.

4.7.5 Discussion on differential threshold method

The benefits of the differential threshold method are that bubble’s residence times are measured more accurately and bubbles whose signals do not reach the upper threshold in the double threshold method can be detected and factored into the phase indicator function. Additionally, with this method the active length of a probe no longer dictates the lower bounds on the size of bubbles that are measureable. The analysis performed focused on improving the methodology for the probes used in the Kann boat experiments, but can easily be applied to any probe geometry. With a probe such as Probe 3 (§4.3) and the differential threshold method it can be expected that bubbles down to a few microns can be detected if an appropriate electronic suite can be developed.

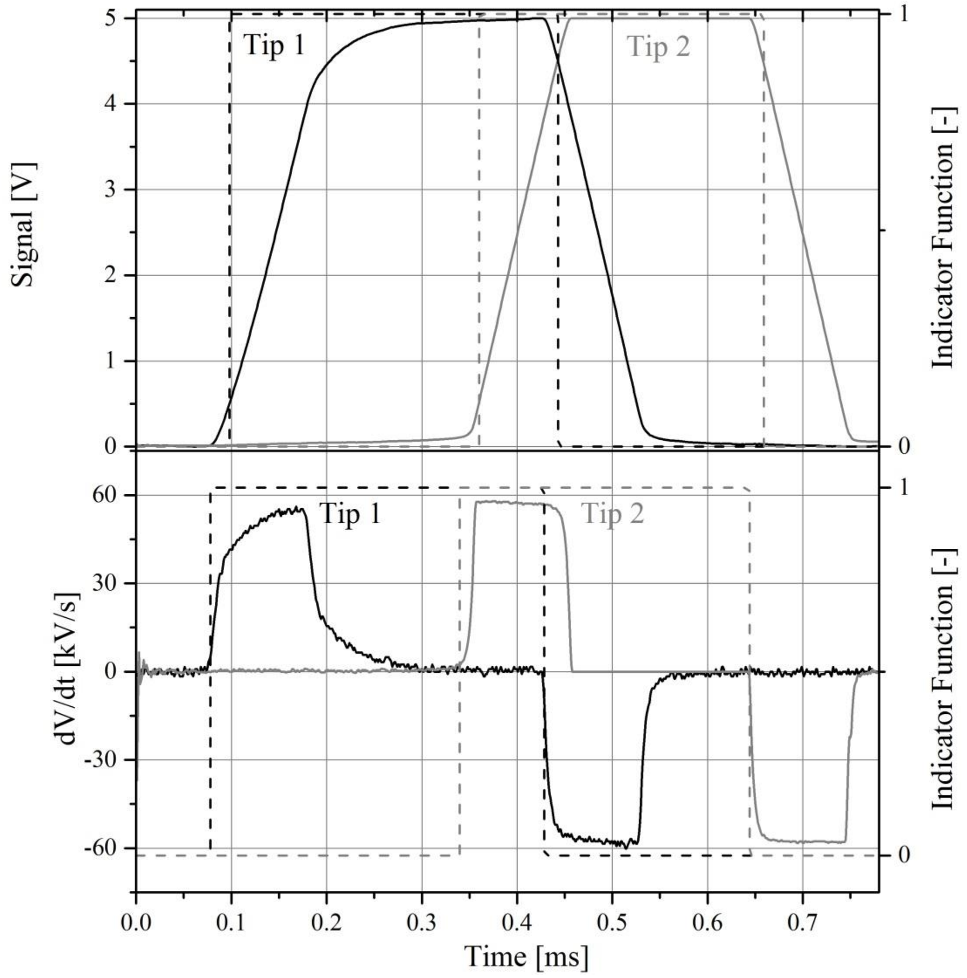

Figure 70: Differential threshold method applied to bubble piercing in Fig. 57. Analog signal with double threshold indicator function (top), derivative and differential-threshold indicator function (bottom)

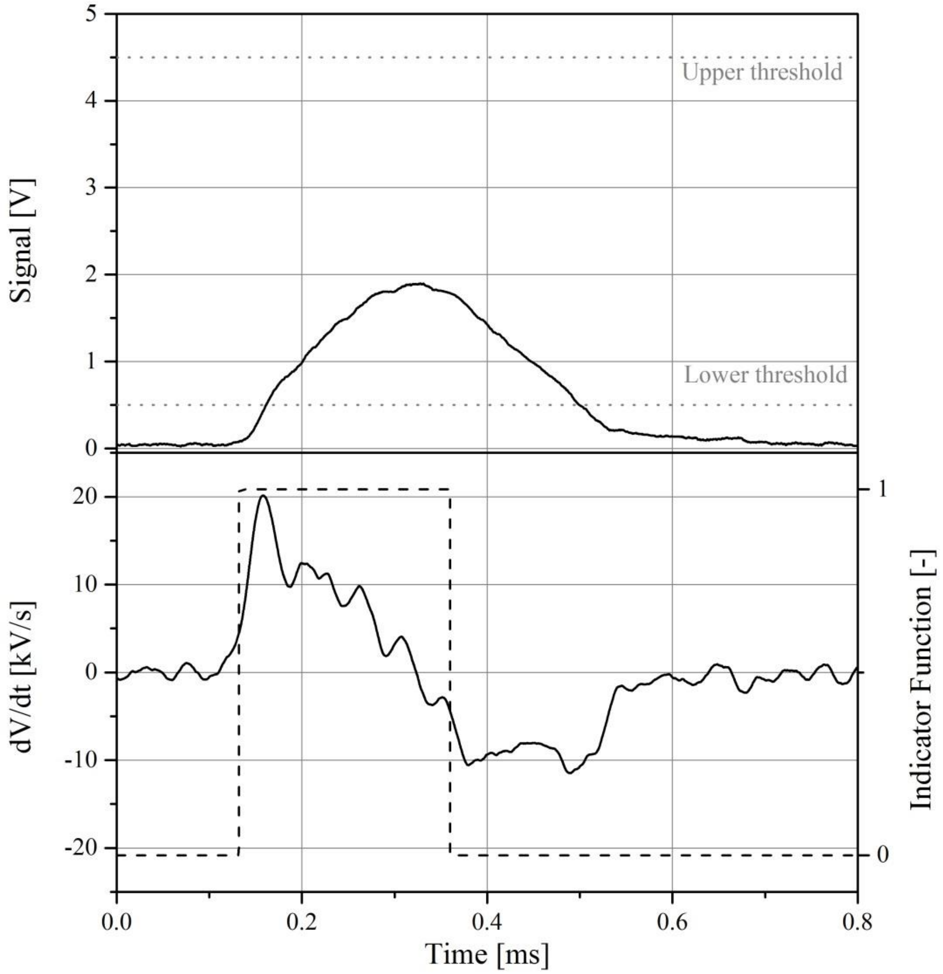

Figure 71: Differential threshold method applied to bubble graze of Fig. 58. Analog signal (top), derivative and differential-threshold indicator function (bottom)

CHAPTER 5: CONCLUSIONS AND FUTURE WORK

The complexity of two-phase flow surrounding a ship makes it a challenging topic to study. Numerical simulation lack adequate models to universally predict the polydispersed bubbly flows, while the harsh environment coupled with the high speeds make full scale experimentation a challenge. This thesis contributes to the development of micro sized optical phase detection probes capable of functioning in hostile environments, and their characterization and use to study the bubbly flow within the turbulent boundary layer of boat.

5.1 Conclusions

With the current optical phase detection probes, the limiting bubble size measurable is not defined by the size of the 45 degree tip, but rather the location anywhere along the fiber that the threshold to transition to air is reached. With the exception of stretch glass fiber probes whose core/cladding structure remains in tacked, any tapered probe that has a reduction in the cross sectional area in an effort to measure small bubbles will have light escape along the exposed elongation that will be reflected and refracted in the same fashion as the 45° tip. This primarily affects probe tips that have 45° tips smaller than 50 μm. Bubbles less than 1 mm show slight deformations when pierced by the probes, but show minimal error in their residence time when a properly tuned double threshold technique is used.

Pertaining to the study of the Kann boat's two-phase boundary layer, measurements of void fraction, bubble velocity and bubble size were performed within the boundary layer of the boat's flat bottom. These measurements were taken at the bow, near the bubble entrainment region, and at the stern. The results indicate that changes in the environmental conditions (wind, swell, free surface roughness) cause high variability in void fraction and average chord length. At low speeds the bubble residence time is longer, turbulence is weaker and bubbles rise and accumulate under the hull where, in fresh water, they coalesce, producing larger bubbles at the stern location. In salt water coalescence is inhibited and accumulation of large bubbles is much less pronounced at the stern. At high speeds the shear rate and turbulence intensity increase, resulting in the production of small bubbles (smaller than $250\ \mu m$). This occurs both in fresh and salt water. Using the breakup models of Lehr *et al.* (2002), Grace (1982) and Müller-Fischer *et al.*(2008), bubbles as small as $200\ \mu m$ can be produced, but neither the levels of turbulence nor the shear rate present near the wall are strong enough to produce bubbles smaller than $150\ \mu m$ (as observed in the experiments) which indicates that other processes are causing the bubbles to break. One possible mechanism that could produce very small bubbles is the combination of shear, which elongates the bubbles, and turbulent eddies, which could break the elongated, weaker bubble even if unable to break a more stable spherical bubble. Breakup could also be caused by the highly non-uniform velocity gradients found within the boundary layer. No models of breakup exist that combine the canonical processes of turbulent and shear breakup.

Bubble velocity measurements indicate that bubbles slip and do not attach to the wall, thus showing significantly less velocity gradient than the liquid. Large velocity fluctuations are observed for the bubble velocity at the stern, with RMS fluctuations increasing near the wall.

Results show that void fraction are typically moderate (less than 10%), in agreement with other full scale measurements in ships. The void fraction at the stern peaks just before the wall is reached, except at 10 knots in fresh water, where the peak is at the wall. At the bow the void fraction is more uniform.

5.2 Recommendations for future work

- Develop a suitable electronic module to generate the phase indicator function using the differential threshold method described in § 4.7.
- Further develop the single tip probes of Chapter 3, namely the notch design of §3.3 which would allow highly accurate measurements of bubbly velocity and size with minimal size and better robustness.
- Analyze behavior of probes at high speed
- Study sapphire fiber stretching techniques to produce appropriate tip shapes that reduce/eliminate sensitivity except in the desired active tip.

- Study sapphire coating techniques to produce a fiber with cladding, for instance with glass.

REFERENCES

Barigou, M., & Greaves, M. (1991). A capillary suction prove for bubble size measurement. *Measurement Science and Technology, 2*(4), 318.

Barrau, E., Rivière, N., Poupot, C., & Cartellier, A. (1999). Single and double optical probes in air-water two-phase flows: real time signal processing and sensor performance. *International Journal of Multiphase Flow, 25*(2), 229-256.

Becker, H., Hottel, H., & Williams, G. (1967). On the light-scatter technique for the study of turbulence and mixing. *Journal of Fluid Mechanics, 30*(02), 259-284.

Bell, R., Boyce, B., & Collier, J. (1972). *Structure of a submerged impinging gas jet*. *J. Brit. Nucl. Energy Soc.* 11: No. 2, 183-93.

Bendat J.S. and Piersol, A.G. (1971). Random DataL Analysis and Measurement Procedures. John Wiley & Sons, Inc. New York, NY.

Blenkinsopp, C., & Chaplin, J. (2007). *Void fraction measurements in breaking waves.* Paper presented at the Proceedings of the Royal Society of London A: Mathematical, Physical and Engineering Sciences.

Cartellier, A. (1990). Optical probes for local void fraction measurements: characterization of performance. *Review of Scientific Instruments, 61*(2), 874-886.

Cartellier, A., & Achard, J. (1991). Local phase detection probes in fluid/fluid two-phase flows. *Review of Scientific Instruments, 62*(2), 279-303.

Cartellier, A., & Barrau, E. (1998). Monofiber optical probes for gas detection and gas velocity measurements: conical probes. *International Journal of Multiphase Flow, 24*(8), 1265-1294.

Cartmill, J. W., & Su, M. Y. (1993). Bubble size distribution under saltwater and freshwater breaking waves. *Dynamics of atmospheres and oceans, 20*(1), 25-31.

Castro, A. M., & Carrica, P. M. (2013). Bubble size distribution prediction for large-scale ship flows: Model evaluation and numerical issues. *International Journal of Multiphase Flow, 57*, 131-150.

Ceccio, S., & George, D. (1996). A review of electrical impedance techniques for the measurement of multiphase flows. *Journal of fluids engineering, 118*(2), 391-399.

Ceccio, S. L. (2010). Friction drag reduction of external flows with bubble and gas injection. *Annual Review of Fluid Mechanics, 42*, 183-203.

Chen, F., Gomez, C., & Finch, J. (2001). Technical note bubble size measurement in flotation machines. *Minerals Engineering, 14*(4), 427-432.

Clark, N. N., & Turton, R. (1988). Chord length distributions related to bubble size distributions in multiphase flows. *International Journal of Multiphase Flow, 14*(4), 413-424.

Craig, V. S., Ninham, B. W., & Pashley, R. M. (1993). The effect of electrolytes on bubble coalescence in water. *The Journal of Physical Chemistry, 97*(39), 10192-10197.

Danel, F., & Delhaye, J. (1971). Sonde optique pour mesure du taux de presence local en ecoulement diphasique. *Mesures-Regulation—Automatisme*, 99-101.

De Bruijn, R. (1993). Tipstreaming of drops in simple shear flows. *Chemical Engineering Science, 48*(2), 277-284.

Debruijn, R. A. (1991). *Deformation and breakup of drops in simple shear flows*. PhD thesis. Eindhoven Univ. Technol., The Netherlands.

Delhaye, J. (1968). *Measurement of the local void fraction in two-phase air-water flow with a hot-film anemometer*. CEA-R-3465(E)

Delhaye, J., & Chevrier, C. (1966). The use of resistivity probes for the measurement of local void fraction in two-phase flow. *CEN Grenoble, Report No TT 70.*(122, 123).

Elemans, P., Bos, H., Janssen, J., & Meijer, H. (1993). Transient phenomena in dispersive mixing. *Chemical Engineering Science, 48*(2), 267-276.

Goldschmidt, V. W. (1965). Measurement of aerosol concentrations with a hot wire anemometer. *Journal of Colloid Science, 20*(6), 617-634.

Gouirand, J. (1990). *Technology and signal treatment development of optical probes for two-phase flow measurements.* Paper presented at the The Hague'90, 12-16 April.

Grace, H. P. (1982). Dispersion phenomena in high viscosity immiscible fluid systems and application of static mixers as dispersion devices in such systems. *Chemical Engineering Communications, 14*(3-6), 225-277.

Grau, R., & Heiskanen, K. (2002). Visual technique for measuring bubble size in flotation machines. *Minerals Engineering, 15*(7), 507-513.

Guido-Lavalle, G., Carrica, P., Clausse, A., & Qazi, M. (1994). A bubble number density constitutive equation. *Nuclear engineering and design, 152*(1), 213-224.

Harvel, G., Hori, K., Kawanishi, K., & Chang, J. (1996). Real-time cross-sectional averaged void fraction measurements in vertical annulus gas-liquid two-phase flow by neutron radiography and X-ray tomography techniques. *Nuclear Instruments and Methods in Physics Research Section A: Accelerators, Spectrometers, Detectors and Associated Equipment, 371*(3), 544-552.

Hecht, E. and Zajac, A. (1974). Optics. Addison-Wesley, Reading, MA.

Hinata, S. (1972). A Study on the Measurement of the Local Void Fraction by the Optical Fibre Glass Probe: 1st Report, On the Method for the Measurement of the Local Void Fraction in a Liquid Metal Two-Phase Flow. *Bulletin of JSME, 15*(88), 1228-1235.

Hinze, J. (1955). Fundamentals of the hydrodynamic mechanism of splitting in dispersion processes. *AIChE Journal, 1*(3), 289-295.

Hong, M., Cartellier, A., & Hopfinger, E. J. (2004). Characterization of phase detection optical probes for the measurement of the dispersed phase parameters in sprays. *International Journal of Multiphase Flow, 30*(6), 615-648.

Hong, M., Cartellier, A., & Hopfinger, E. J. (2004). Characterization of phase detection optical probes for the measurement of the dispersed phase parameters in sprays. *International Journal of Multiphase Flow, 30*(6), 615-648.

Hoschek, S. S., Carrica, P. M., & Weber, L. J. (2008). Bubble entrainment and distribution in a model spillway with application to total dissolved gas minimization. *Journal of Hydraulic Engineering, 134*(6), 763-771.

Hsu, Y., Simon, F., & Graham, R. (1963). *Application of hot-wire anemometry for two-phase flow measurements such as void fraction and slip velocity*. Paper presented at the Proceedings of the ASME Winter Meeting, Philadelphia, PA.

Hsu, Y., Simoneau, R., Simon, F., & Graham, R. (1969). *Photographic and other optical techniques for studying two-phase flow*. Paper presented at the ASME Symposium Volume: TwoPhase Flow Instrumentation.

Janssen, J., Boon, A., & Agterof, W. (1994). Influence of dynamic interfacial properties on droplet breakup in simple shear flow. *AIChE Journal, 40*(12), 1929-1939.

Jin, N., Xin, Z., Wang, J., Wang, Z., Jia, X., & Chen, W. (2008). Design and geometry optimization of a conductivity probe with a vertical multiple electrode array for measuring volume fraction and axial velocity of two-phase flow. *Measurement Science and Technology, 19*(4), 045403.

Johansen, J. P., Castro, A. M., & Carrica, P. M. (2010). Full-scale two-phase flow measurements on Athena research vessel. *International Journal of Multiphase Flow, 36*(9), 720-737.

Kataoka, I., Ishii, M., & Serizawa, A. (1984). *Local formulation of interfacial area concentration and its measurements in two-phase flow*. Argonne National Laboratory Report, ANL-84-68, NUREG/CR-4029.

Kim, S., Fu, X., Wang, X., & Ishii, M. (2000). Development of the miniaturized four-sensor conductivity probe and the signal processing scheme. *International journal of heat and mass transfer, 43*(22), 4101-4118.

Latorre, R., Miller, A., & Philips, R. (2003). Micro-bubble resistance reduction on a model SES catamaran. *Ocean engineering, 30*(17), 2297-2309.

Le Corre, J.-M., Hervieu, E., Ishii, M., & Delhaye, J.-M. (2003). Benchmarking and improvements of measurement techniques for local-time-averaged two-phase flow parameters. *Experiments in fluids*, *35*(5), 448-458.

Lehr, F., Millies, M., & Mewes, D. (2002). Bubble-Size distributions and flow fields in bubble columns. *AIChE Journal*, *48*(11), 2426-2443.

Liao, Y., & Lucas, D. (2009). A literature review of theoretical models for drop and bubble breakup in turbulent dispersions. *Chemical Engineering Science, 64*(15), 3389-3406.

Liu, W., Clark, N. N., & Karamavruç, A. I. (1998). Relationship between bubble size distributions and chord-length distribution in heterogeneously bubbling systems. *Chemical Engineering Science, 53*(6), 1267-1276.

Luo, H., & Svendsen, H. F. (1996). Theoretical model for drop and bubble breakup in turbulent dispersions. *AIChE Journal-American Institute of Chemical Engineers, 42*(5), 1225-1233.

Marrucci, G. (1969). A theory of coalescence. *Chemical Engineering Science, 24*(6), 975-985.

Martínez-Bazán, C., Montanes, J., & Lasheras, J. C. (1999). On the breakup of an air bubble injected into a fully developed turbulent flow. Part 1. Breakup frequency. *Journal of Fluid Mechanics, 401*, 157-182.

Miller, N., & MitBchie, R. (1969). *The development of a universal probe for measurement of local voidage in liquid/gas two-phase flow systems*: ASME.

Müller-Fischer, N., Tobler, P., Dressler, M., Fischer, P., & Windhab, E. J. (2008). Single bubble deformation and breakup in simple shear flow. *Experiments in fluids, 45*(5), 917-926.

National Defense Research Committee Division 6, S. T. R. V. (1946). Physics of Sound in the Sea. *reprinted 1969 as NAVMAT, Report P-9675*.

Neal, L., & Bankoff, S. (1963). A high resolution resistivity probe for determination of local void properties in gas-liquid flow. *AIChE Journal, 9*(4), 490-494.

Perret, M., & Carrica, P. M. (2011). Near-Ship Field Measurements of Bubble Velocity, Volume Fraction and Size Distribution Using Local-Phase Detection Probes. *4th International Conference on Underwater Acoustic Measurements: Technologies and Results*(Kos, Greece).

Perret, M., & Carrica, P. M. (2015). Bubble–wall interaction and two-phase flow parameters on a full-scale boat boundary layer. *International Journal of Multiphase Flow*, *73*, 289-308.

Perret, M., Esmaeilpour, M., Politano, M. S., & Carrica, P. M. (2013). Experimental study of a two-phase surface jet. *Experiments in fluids, 54*(4), 1-20.

Perret, M. N., Esmaeilpour, M., & Carrica, P. M. (2014). Two phase flow measurements in a full scale boundary layer. *30th Symposium on Naval Hydrodynamics*. (Hobart, Australia).

Prasser, H.-M., Böttger, A., & Zschau, J. (1998). A new electrode-mesh tomograph for gas–liquid flows. *Flow measurement and instrumentation*, *9*(2), 111-119.

Prasser, H.-M., Scholz, D., & Zippe, C. (2001). Bubble size measurement using wire-mesh sensors. *Flow measurement and instrumentation*, *12*(4), 299-312.

Prince, M. J., & Blanch, H. W. (1990). Bubble coalescence and break-up in air-sparged bubble columns. *AIChE Journal*, *36*(10), 1485-1499.

Randall, E., Goodall, C., Fairlamb, P., Dold, P., & O'Connor, C. (1989). A method for measuring the sizes of bubbles in two-and three-phase systems. *Journal of Physics E: Scientific Instruments*, *22*(10), 827.

Stanic, S., Caruthers, J. W., Goodman, R. R., Kennedy, E., & Brown, R. (2009). Attenuation measurements across surface-ship wakes and computed bubble distributions and void fractions. *Oceanic Engineering, IEEE Journal of*, *34*(1), 83-92.

Takahashi, K. M. (1990). Meniscus shapes on small diameter fibers. *Journal of colloid and interface science*, *134*(1), 181-187.

Takahashi, T., Kakugawa, A., Makino, M., & Kodama, Y. (2003). Experimental study on scale effect of drag reduction by microbubbles using very large flat plate ships. *Journal-Kansai Society of Naval Architects Japan*, 11-20.

Terrill, E., Melville, K., Lada, G., Otero, M., Hazard, J., Harris, T., Pierson, A., Middleton, B., Jenkins, T., (2005). 2004 Field Measurements. *2005 ONR Bubbly Flow Program Review*(Pasadena, CA).

Terrill, E. and Fu, T. At-sea measurements for ship hydromechanics. *27th Symposium on Naval Hydrodynamics* (Seoul, Korea).

Trainer, M.N. (2000). Fiber optic hygrometer apparatus and method. United States patent US 6164817 A.

Trevorrow, M. V., Vagle, S., & Farmer, D. M. (1994). Acoustical measurements of microbubbles within ship wakes. *The Journal of the Acoustical Society of America*, *95*(4), 1922-1930.

Trevorrow, M. V., Vasiliev, B., & Vagle, S. (2006). Wake acoustic measurements around a maneuvering ship. *Canadian Acoustics*, *34*(3), 112-113.

Tsang, Y. H., Koh, Y.-H., & Koch, D. L. (2004). Bubble-size dependence of the critical electrolyte concentration for inhibition of coalescence. *Journal of colloid and interface science*, *275*(1), 290-297.

Vagle, S., & Burch, H. (2005). Acoustic measurements of the sound-speed profile in the bubbly wake formed by a small motor boat. *Journal of the Acoustical Society of America*, *117*(1), 153-163.

Vagle, S., & Farmer, D. M. (1998). A comparison of four methods for bubble size and void fraction measurements. *Oceanic Engineering, IEEE Journal of*, *23*(3), 211-222.

Vince, M., Breed, H., Krycuk, G., & Lahey, R. (1982). Optical probe for high-temperature local void fraction determination. *Applied optics*, *21*(5), 886-892.

Weissenborn, P. K., & Pugh, R. J. (1995). Surface tension and bubble coalescence phenomena of aqueous solutions of electrolytes. *Langmuir*, *11*(5), 1422-1426.

Yianatos, J., Bergh, L., Condori, P., & Aguilera, J. (2001). Hydrodynamic and metallurgical characterization of industrial flotation banks for control purposes. *Minerals Engineering*, *14*(9), 1033-1046.

Žun, I., Filipič, B., Perpar, M., & Bombač, A. (1995). Phase discrimination in void fraction measurements via genetic algorithms. *Review of Scientific Instruments*, *66*(10), 5055-5064.